

## **Preliminary Study of a Hybrid Rocket**

**Pedro Paulo de Oliveira Alcaria Guerreiro**

Thesis to obtain the Master of Science Degree in

### **Mechanical Engineering**

#### **Examination Committee**

Chairperson:	Prof. Luís Rego da Cunha de Eça
Supervisor:	Prof. João Eduardo de Barros Teixeira Borges
Co-Supervisor:	Prof. António Manuel Relógio Ribeiro
Members of the Committee:	Prof. Viriato Sérgio de Almeida Semião

**May 2013**



«Quando você quer alguma coisa, todo o universo conspira para que você realize o seu desejo.»

*Paulo Coelho*

*Dedico este trabalho*

*À minha mãe Ivette,*

*À mais recente mamã e minha irmã Cláudia,*

*Por estarem sempre presentes, e*

*À minha tia Ana (27 de Setembro de 1952 - 9 de Novembro de 2012) e*

*À minha avó Emirene (7 de Dezembro de 1933 - 5 de Janeiro de 2013),*

*Que não estando presentes... estão.*

## Resumo

O mercado da indústria aeroespacial está em expansão nos últimos tempos, devendo-se à crescente procura de serviços de lançadores para colocar satélites de comunicação em órbita, mas também devido ao crescente interesse pelo turismo espacial, passando pelo descomissionamento do Space Shuttle. Há portanto necessidade e mercado para um foguete que permita reduzir custos e aumentar a simplicidade, assegurando um bom nível de desempenho. É nesse contexto que, no universo da propulsão química, surge com elevado interesse o motor de foguete híbrido. Ele acaba por ser uma solução de compromisso, uma vez que permite desempenhos mais próximos dos motores de foguete líquidos, mas com uma simplicidade quase a par dos motores de foguete sólidos.

No entanto, ainda há espaço para melhorar. E é aqui que esta tese propõe-se a desenvolver uma ideia que permite simplificar ainda mais estes motores híbridos, tornando-os assim mais competitivos. Por detrás deste novo conceito, está o aproveitamento da energia calorífica perdida por transferência de calor pelas paredes da tubeira supersónica destes motores. Energia essa que irá ser utilizada para auto pressurizar o reservatório de comburente, ajudando a manter as condições de temperatura e pressão constantes no reservatório, e com isso evitando assim sistemas mais complexos e pesados de pressurização do comburente.

A investigação começa por apresentar um estudo preliminar do novo conceito de motor híbrido, para depois desenvolver um simulador que inclui o uso de transferência de calor. É também efectuado um trabalho experimental cujos resultados permitem testar o modelo do reservatório de comburente saturado.

### Palavras Chave:

Foguete Híbrido, Propulsão de Foguete, Simulação Computacional, Transferência de Calor, Trabalho Experimental, Modelo de Reservatório de Comburente.

## **Abstract**

In recent years the aerospace industry market expanding, much at the expense of a huge demand for launching services, such as the orbit placement of communication satellites, but also due to a growing interest in space tourism and the decommissioning of Space Shuttle. Therefore there is need and market for a rocket that allow lower costs and greater simplicity, while ensuring a good level of performance. It is in this context that, in the universe of chemical propulsion, a high interest in the hybrid rocket motor is growing. It turns out to be a compromise solution, since it allows performance closer to the liquid rocket engines, but with the simplicity of solid rocket motors.

However, there is still room for improvement. And it is here that this thesis proposes to develop an idea that allows further simplification of these hybrid engines, thereby making them more competitive. Behind this new concept is the use of the heat energy lost by heat transfer through the walls of the supersonic nozzle. This energy will be used to pressurize the oxidizer tank, helping to maintain its temperature and pressure conditions, and thereby avoiding more complex and cumbersome systems to pressurize the oxidizer.

The research begins by presenting a hybrid engine new concept preliminary design study, and then develops a simulator that respond to the possibility of using this heat transfer. The saturated oxidizer tank model was tested by the results of an experimental work.

### **Keywords:**

Hybrid Rocket, Rocket Propulsion, Computational Simulation, Heat Transfer, Experimental Work, Oxidizer Tank Model.

## Acknowledgement

First and foremost, my appreciation is addressed to my supervisor, Professor Teixeira Borges for his valuable scientific advice, discussions and suggestions that made this work possible.

I am also grateful to my co-supervisor, Professor António Relógio Ribeiro, for his valuable comments on my thesis and his influence to my work.

I owe my most sincere gratitude to Professor Nunes da Ponte who gave me the opportunity to use the experimental facilities at FCT/UNL.

I would like to thank to the Professor Vesna Nadjanovic and Professor Ana Nunes for the help with the experimental work in FCT/UNL and the numerous stimulating discussions.

I also would like to acknowledge to all the UNL/FCT staff for the help in the experimental work.

The support provided by Engineer Tiago Pardal from Omnidea during the investigation is also greatly acknowledged, as well as the entire Omnidea team, such as Engineers Pedro Silva, Pedro Lima, Pedro Ferreira, Nuno Fernandes, Rei Fernandes, Horácio Moreira, Ricardo Penedo.

The financial support provided by IDMEC/Omnidea is acknowledged.

Finally, my special gratitude to my mother Ivette Oliveira, my sister Cláudia Guerreiro, my family my friends and girlfriend for their encouragement and support.

# Contents

Resumo .....	ii
Abstract.....	iii
Acknowledgement .....	iv
List of Figures .....	vii
List of Tables .....	ix
List of Symbols .....	x
Acronyms and abbreviations .....	xiii
1 Introduction.....	1
1.1 Hybrid rocket propulsion and a proposed self-stable engine .....	1
1.2 Scope and goals.....	2
1.3 Document structure .....	2
2 State of the art.....	3
2.1 Hybrid Rocket Propulsion.....	6
2.1.1 Advantages and Disadvantages of HRP .....	6
2.1.2 Applying conditions of the HRP.....	7
2.2 History and recent developments of HPRE .....	8
2.3 Project motivation and innovation: what is new?.....	12
2.4 Propellant trade-off study and selection .....	13
2.4.1 Candidate combinations.....	13
2.4.2 Brief discussion on the several options considered .....	14
2.4.3 Selection .....	18
2.4.4 Safety considerations.....	19
3 Methodology.....	23
3.1 Hybrid rocket design.....	23
3.1.1 Hybrid rocket layout .....	23
3.1.2 Hybrid rocket sizing.....	24
3.1.3 Heat transfer system .....	31
3.1.4 Preliminary material selection .....	34
3.2 Hybrid rocket simulation .....	35
3.2.1 Simulation model.....	35
3.3 Tank validation model .....	46
3.3.1 Material characterization .....	47

3.3.2	Simulation model.....	49
3.3.3	Experimental setup .....	49
3.3.4	Experimental procedure .....	53
4	Results and Discussion .....	56
4.1	Hybrid rocket preliminary design .....	56
4.2	Tank validation model .....	56
4.2.1	Experiment 1 .....	57
4.2.2	Experiment 2 .....	60
4.2.3	Experiment 3 .....	63
4.3	Hybrid rocket simulation .....	65
4.3.1	Results without heat transfer.....	66
4.3.2	Results with heat transfer.....	68
5	Conclusions and Future Work .....	76
5.1	Viability .....	76
5.2	Engine stability .....	76
5.3	Test program and future developments .....	77
6	References .....	79
	Appendix.....	82



## List of Figures

Fig. 2.1 – Hybrid Propulsion System more common in rocketry (Sutton, 1992).....	6
Fig. 2.2 – Hybrid Rocket Engine history until 2000 (Zandbergen, 2013).....	8
Fig. 2.3 - <i>Space Ship One</i> (a) and <i>Space Ship Two</i> (b) from Scaled Composites.....	9
Fig. 2.4– Theoretical vacuum Specific Impulse of several liquid oxidizers for HTPB solid fuel (Sutton, 1992). Note that the mixture ratio is the oxidizer-to-fuel ratio.....	11
Fig. 2.5 – Common heat transfer distribution along the rocket engine (Sutton, 1992). ....	13
Fig. 2.6 - Propellant trade-off study and selection.....	18
Fig. 3.1 – Project hybrid rocket layout.....	24
Fig. 3.2 - Combustion products temperature based on OF ratio and pressure for N <sub>2</sub> O - C <sub>32</sub> H <sub>66</sub> combustion. ....	27
Fig. 3.3 – Conical nozzle geometry: (a) convergent section and (b) divergent section (Zandbergen, 2007).....	30
Fig. 3.4 – Enthalpy variation of liquid and gas phases for pure nitrous oxide.....	32
Fig. 3.5 – Simulation schematic. ....	35
Fig. 3.6 – Schematic of the stratified tank model showing the orifice through the vapor propellant escapes. ....	43
Fig. 3.7 – Molecular geometry of nitrous oxide and carbon dioxide.....	47
Fig. 3.8 – CO <sub>2</sub> and N <sub>2</sub> O: (a) saturated pressure and (b) saturated liquid and vapour density....	48
Fig. 3.9 - CO <sub>2</sub> and N <sub>2</sub> O saturated liquid and vapour specific internal energy. ....	49
Fig. 3.10 – Photo of the experimental setup at FCT/UNL laboratory. ....	51
Fig. 3.11 – Experimental schematic. ....	51
Fig. 4.1 – Simulation and experimental results of experiment 1: .....	60
Fig. 4.2 - Simulation and experimental results of experiment 2: .....	62
Fig. 4.3 – Simulation and experimental results of experiment 3: .....	65
Fig. 4.4 - Simulation results without heat transfer.....	68
Fig. 4.5 - Simulation results with a heat transfer fraction of 15%.....	70
Fig. 4.6 - Simulation results with a heat transfer fraction of 50%.....	73

Fig. 4.7 - Simulation results with a heat transfer fraction of 25%..... 75

Fig. 0.1 – Vulcain 2 rocket engine, from Astrium, that powers the Ariane 5 (LOX/LH2). With regenerative cooling system that supports the combustion chamber and also the active cooled nozzle by dump flow..... 82

## List of Tables

Tab. 2.1 – Propellant combination candidates.....	14
Tab. 2.2 – Some properties of oxidizer candidates comparison. A quality of 0.1 for saturated phase mixtures is considered in above properties. (NIST, 2013) .....	15
Tab. 2.3 – Flow rate coefficients comparison for a sonic throat. Values are at reference pressure of 45 bar. (NIST, 2013).....	15
Tab. 2.4 – Stoichiometric conditions for case study combinations. ....	16
Tab. 2.5 – Case study performance parameters.....	17
Tab. 3.1 – N <sub>2</sub> O and CO <sub>2</sub> critical properties. ....	48
Tab. 3.2 - Principal characteristics and pictures of the major experimental equipment.....	53
Tab. 4.1 – Hybrid rocket design results.....	56
Tab. 4.2 - Initial and final conditions of the experiment 1 tests. ....	58
Tab. 4.3 – Relative errors between the experimental and simulated data of experiment 1.....	60
Tab. 4.4 - Initial and final conditions of the experiment 2 tests. ....	61
Tab. 4.5 – Relative errors between the experimental and simulated data of experiment 2.....	62
Tab. 4.6 - Initial and final conditions of the experiment 3 tests. ....	63
Tab. 4.7 – Relative errors between the experimental and simulated data of experiment 3.....	65

# List of Symbols

## Latin Symbols

$A$	Area	$[m^2]$	$M$	Molar mass	$[kg/kmol]$
$a$	Speed of sound	$[m/s]$	$Ma$	Mach number	
$a_{eff}$	Effective acceleration	$[m/s^2]$	$\dot{m}$	Mass flow rate	$[kg/s]$
$C_d$	Discharge coefficient		$OF$	Oxidizer-to-fuel ratio	
$C_{SF}$	Surface-fluid combination constant		Pr	Prandtl number	
$c_p$	Specific heat at constant pressure	$[J/kg.K]$	$p$	Pressure	$[Pa]$
$c_v$	Specific heat at constant volume	$[J/kg.K]$	$q$	Heat power, heat transfer rate	$[W]$
$D$	Diameter	$[m]$	$q''$	Heat flux	$[W/m^2]$
$F$	Thrust force	$[N]$	$R_A$	Universal gas constant	$[J/kmol.K]$
$g_0$	Gravitational acceleration	$[m/s^2]$		(8314.472 J/kmol.K)	
$H$	Height	$[m]$	$\dot{r}$	Regression rate	$[m/s]$
$h$	Specific enthalpy	$[J/kg]$	$S$	Surface area	$[m^2]$
$\bar{h}$	Convection heat transfer coefficient	$[W/m^2.K]$	$s$	Specific entropy	$[J/kg.K]$
$I_{sp}$	Specific impulse	$[s]$	$T$	Temperature	$[K]$
$k$	Thermal conductivity	$[W/m.K]$	$U$	Velocity	$[m/s]$
$L$	Length	$[m]$	$u$	Specific internal energy	$[J/kg]$
			$V$	Volume	$[m^3]$

## Greek Symbols

$\beta$	Conical nozzle convergent angle	$\theta$	Conical nozzle divergent angle
$\gamma$	Specific heat ratio	$\mu$	Viscosity [kg/s.m]
$\Delta t$	Time variation, time step [s]	$\rho$	Specific mass, density [kg/m <sup>3</sup> ]
$\varepsilon$	Expansion ratio	$\sigma$	Surface tension [N/m]
$\eta$	Efficiency factor	$\chi$	Quality of a two – phase liquid – vapour mixture

## Subscripts

$a$	Ambient	$eq$	Equivalent
$base$	Base	$f$	Fuel
$CO_2$	Carbon dioxide	$fg$	Vaporization
$c$	Chamber	$film$	Film
$comb$	Combustion	$g$	Gas, vapour phase
$con$	Conical nozzle convergent section	$inj$	Injection
$cr$	Critical	$l$	Liquid phase
$d$	Dowstream	$lat$	Lateral
$div$	Conical nozzle divergent section	$max$	Maximum
$e$	Exit, exhaust	$min$	Minimum
		$new$	New value

<i>nozzle</i>	Nozzle	<i>tp</i>	Triple point condition
<i>old</i>	Old/Actual Value	<i>u</i>	Upstream
<i>ox</i>	Oxidizer	<i>vap</i>	Vaporization, evaporation
<i>p</i>	Grain port	<i>w</i>	Nozzle wall
<i>pos</i>	Post combustion chamber	<i>x</i>	Distance from the nozzle entrance
<i>pre</i>	Pre combustion chamber	0	Stagnation condition
<i>prod</i>	Combustion products	1	Conditions immediately behind normal shock wave
<i>reactor</i>	Reactor	2	Conditions immediately after normal shock wave
<i>res</i>	Tank reservoir		
<i>sat</i>	Saturation conditions		
<i>t</i>	Nozzle throat		

### ***Superscripts***

<i>n</i>	Prandtl number exponent	<i>a</i>	Interpolation data point <i>a</i>
*	Critical, sonic conditions	<i>b</i>	Interpolation data point <i>b</i>

## Acronyms and abbreviations

AMROC	American Rocket Company
BSP	British Standard Pipe
CEA	Chemical Equilibrium with Applications
CO <sub>2</sub>	Carbon Dioxide
EPS	Étage à Propegols Stockables (Storable Propellant Stage)
ESA	European Space Agency
GTO	Geostationary Transfer Orbit
GPRE	Gaseous Propellant Rocket Engines
GOX	Gaseous Oxygen
HCF	Hybrid Combustion Facility
HPRE	Hybrid Propellants Rocket Engines
HRP	Hybrid Rocket Propulsion
HTPB	Hydroxyl-Terminated Polybutadiene
ITI	Innovation Triangle Initiative
JATO	Jet Assisted Take-Off
LEO	Low Earth Orbit
LOX	Liquid Oxygen
LPRE	Liquid Propellant Rocket Engines
LRE	Liquid Rocket Engines
NASA	National Aeronautics and Space Administration
NIST	National Institute of Standards and Technology
NPT	National Pipe Thread
N <sub>2</sub> O	Nitrous Oxide
NRE	Nuclear Rocket Engines
OF	Oxidizer to Fuel ratio
O <sub>2</sub>	Oxygen
PCTFE	Polychlorotetrafluorethylene
PE	Polyethylene
PET	Polyethylene Teraphatalate
PTFE	Polytetrafluorethylene
PMMA	Plymethylmethacrylate (Plexiglass)
RTD	Resistance Temperature Detector
SPRE	Solid Propellant Rocket Engines
SRM	Solid Rocket Motors
S-SHE	Self-Stable Hybrid Engine

# 1 Introduction

## 1.1 Hybrid rocket propulsion and a proposed self-stable engine

Hybrid rocket propulsion, although not a new concept, has been gathering more attention in recent years. A hybrid rocket is an intermediate between a solid motor and a liquid engine. One of the propellants, usually the fuel, is stored as a solid grain in the combustion chamber. The other, usually the oxidizer, is stored as a liquid in a separate tank. This arrangement has an intermediate set of advantages and disadvantages, compared to solid and liquid propulsion. Compared to solid motors the main advantages of hybrids are the possibility of throttling and re-start and enhanced safety and reliability. Compared to liquid motors, the main advantages are the overall lower cost, potentially better density specific impulse and engine mass fraction.

A typical hybrid arrangement includes the aforementioned combustion chamber loaded with a solid propellant grain and a tank with a liquid propellant. For some liquid propellants, a pump or a separate tank of pressurized gas (usually helium) is necessary to force injection of the liquid propellant into the combustion chamber. The injection is made in the liquid phase and often requires a carefully designed and manufactured injector head, in order to ensure that, among other things, the liquid propellant is atomized in very fine droplets and will subsequently have a high reaction rate. Some propellants, such as nitrous oxide, which have a high vapour pressure at room temperature, does not require a separate pressurized tank, since it uses the gaseous phase of a saturated mixture to pressurize and inject the liquid phase.

A concept is proposed here, based on the idea proposed in Pardal (2012) patent, with a series of features that set it apart from state-of-the-art hybrids. This system comprises a solid fuel and a liquid oxidizer.

The first defining feature of the proposed engine is that the oxidizer is injected in the combustion chamber at the gaseous phase, rather than as liquid droplets. This is expected to enhance and stabilize combustion, as well as greatly simplifying the injector design, which, in the limiting case, could be reduced to a simple, single injection orifice. Although the injection in the proposed system is made using the gas phase, the oxidizer is stored in the liquid phase, in order to obtain a better density and reduce the mass fraction and volume of the storage tank. This means that it is necessary to vaporize the oxidizer prior to injection.

The second defining feature of the proposed system is that the energy obtained from cooling the nozzle to prevent it from reaching excessive temperatures, is fed back to the oxidizer tank and used to boil the liquid oxidizer for injection. This phase change induced from heating the oxidizer tank with waste heat will also cause the pressurization of the tank.



The third defining feature of the proposed system is that the injection orifice may be choked (sonic). This feature is intended to prevent propagation of pressure waves resulting from any potential instability, back to the oxidizer tank.

The defining features of the proposed system are expected to have together a stabilization effect in the operational parameters of the engine and allow a properly designed system to operate with predictable and near-constant performance through a burn. An engine using these concepts is expected to have advantages over the state of the art in terms of cost, reliability and performance.

## **1.2 Scope and goals**

This document presents some results of studies for the ESA's ITI project S-SHE (Self-Stable Hybrid Engine) carried out at IDMEC/IST under a contract with Omnidea Lda., and based on Omnidea's proprietary concept disclosed on the mentioned project. The objectives of these studies include a propellant selection for an experimental demonstrator, as well as preliminary design, simulation of the mentioned demonstrator and the experimental validation of the oxidizer tank model.

The goals of this document include not only presenting the work done by the author and the conclusions drawn from it regarding the feasibility of the proposed engine, but also to lay the foundations for other experimental work during future stages of the project.

## **1.3 Document structure**

This document is divided in six chapters, including this introduction. In chapter 2, a state-of-the-art in hybrid rocket propulsion is presented. Then, in chapter 3, some relevant theoretical, numerical and experimental methods are presented. Here the hybrid rocket engine is sketched. Sizing is mainly done with usual relations regarding rocket engine operation. Other design considerations include material selection. The engine simulation is also addressed here. The proposed algorithm and equations are described in the design section. Moreover, the experimental validation of a method to obtain a model for the heat transfer at the oxidizer tank is done.

The results are covered in chapter 4. Not only the engine preliminary design results, but also the simulation procedure and the experimental work results as well.

On chapter 5, conclusions drawn from the work described in this thesis, and some recommendations regarding future activities are presented.

References are given in chapter 6.

## 2 State of the art

**Propulsion**, *n* [U] *technical*, the force that drives a vehicle forward.

In Longman Dictionaries (1995).

The above definition is derived from two Latin words: *'pro'*, which means before or forwards, and *'pellere'*, meaning to drive. Combining both of them means to push forward or drive an object forward.

There are various ways of changing the motion of a body depending on the environment, for example: walking and wheels in land, bird flight in air and sailing in water. In aerospace environments, the jet propulsion is the most recognized. Here, the propulsion is generated by a high velocity exhaust jet which imparts a forward reaction on the vehicle.

According to Sutton (1992), jet propulsion can be divided in two classes: rocket propulsion and duct jet propulsion. In the first, the propulsive force (thrust) is generated by expelling stored mass, called the propellant. This is a pure reaction system, because it does not depend on some external medium for the production of the reaction effort. In the second, the device uses the surrounding medium as the "working fluid" rather than stored propellant as in rocket propulsion. For this reason they are called air-breathing engines, like turbojets and ramjets. These are also recognized as direct reaction systems, since the change in momentum of the external medium is purely obtained via energy addition to some ingested medium, like air. A special remark for the turboprop engines should be made, because they are not considered a true jet propulsion device, although 15 to 30% of their total thrust may come from the exhaust jet. For this reason, turboprops are considered indirect reaction systems, since the change in momentum is obtained via an engine and a propeller, Zandbergen (2007).

Rocket propulsion systems can be classified after the type of energy source used and how this is converted into useful work. Here it is distinguished between the systems that carry the energy source within (internal energy source), like chemical and nuclear sources, and the ones that obtain energy from some external source like the Sun or from a controlled remote laser or microwave source.

The most commonly used rocket propulsion systems technology, according to Sutton (1992) and Humble et al. (1995), are the chemical rockets engines, such as gaseous, liquid, solid and hybrid propellants, and the nuclear rocket engines, which are described next.

The gaseous propellant rocket engines (GPRES) use stored high-pressure gas as their working fluid or propellant. This high pressure gas is released by the feeding system and it is ejected at high velocity through a convergent/divergent nozzle. This technology presents some advantages: simplicity, operational safety and normally the use of cleaner propellants, such as  $H_2$ ,  $N_2$  and He. GPRES main disadvantage is the low performance values, since the amount of energy stored as a high pressure gas is usually much smaller than the amount of energy released in a chemical reaction. Moreover, stored gas requires relatively heavy tanks. Due to the small exhaust gas velocity, these engines are used as attitude control systems and secondary orbit transfer.

In the liquid propellant rocket engines (LPRES), the propellants (fuel and oxidizer for a bipropellant system) are stored inside high pressure tanks in liquid phase. They are transferred to the combustion chamber and here energy, in the form of hot gases, is released by chemical reactions. The hot gases are accelerated and ejected at high velocity through a supersonic nozzle. When the LPRES uses only one propellant, reacting by chemical decomposition, these systems are called monopropellants. The storage system is very important for LPRES. The necessary pressure to transport liquid propellants requires a bulky feed system: several precision valves, a complex feed mechanism including pumps, turbines, or a propellant-pressurizing device and a relatively intricate combustion or thrust chamber. This complexity represents, with the development costs, the major disadvantage of this rocket system. Nevertheless, from all the conventional chemical rocket systems, LPRES are the ones which deliver better performance. They also permit repetitive operation, engine start and shut off and throttling capability. The monopropellants LPRES are simpler than the bipropellants engines, but the performance is inferior. One example of LPRES combination is the liquid oxygen (LOX) and kerosene propellant pair, which was used on the Saturn V first stage rocket engine, in the Apollo missions.

The solid propellant rocket engines (SPRES) combine the feed and storage system in the same place: the combustion chamber. Here the solid propellant, also referred as the grain, contains all the chemical elements for complete burning. It is a highly reactive mixture and potentially explosive. When it ignites, the propellant is burned smoothly at a predetermined rate on the exposed surface of the charge and it is difficult to stop the reaction, once initiated. The chemical reaction generates heat and the combustion gases are then accelerated through a supersonic nozzle. SPRES are relatively small, having a high packing density. They are also easy to operate. However, they are difficult to manufacture, handle, transport and control due to the propellant explosive nature. Their performance is relatively small when compared to a LPRES. Also a drawback is the toxicity of their exhaust products. An example of a SPRES is the S44 engine of the VLS – 1 fourth stage, with a combination of ammonium perchlorate ( $NH_4 Cl O_4$ ) as oxidizer (70 %), and a mixture of hydroxyl-terminated polybutadiene (HTPB, 15 %) and aluminium (15 %), as fuel.

In the hybrid propellant rocket engine (HPRE), oxidizer and fuel are in different states. Normally, the fuel is in the solid state and stored in the combustion chamber, while the oxidizer is in liquid or gaseous state and is feed through a similar conventional LPRE system. The solid fuel is vaporized with the combustion heat and mixes with the oxidizer vapour to burn. The hot gases are ejected through a supersonic nozzle. The HPRE are simpler than the liquid bipropellants and can provide higher specific impulse than the solid propellants. Moreover they are commonly safer than the other systems and the exhaust products are nontoxic. As drawbacks, the HPRE have a lower packing density when compared to the solid rockets, and a performance smaller than the liquid bipropellants engines. As an example of HPRE, is the Space Ship One of Scaled Composites, which is motored with a hybrid rocket engine where the propellant pair is nitrous oxide ( $N_2O$ ), as oxidizer, and HTPB, as the fuel. The rocket design was such a success that the same manufacturer built the Space Ship Two, a more advanced spacecraft. Special attention should be given to this rocket, since last 30<sup>th</sup> April 2013 it completed its first successful powered flight.

The nuclear rocket engines (NRE) use nuclear energy to heat a working fluid, usually liquid hydrogen, so that it can be expanded in a nozzle and thus accelerated to high ejection velocities. The nuclear energy sources can be from three types: the fission reactor, the radioactive isotope decay source, and the fusion reactor. NRE can be seen as an extension of LPRE. While in liquid engines it is the chemical reactions that are responsible for heating the gas, in the nuclear rockets the energy is derived from transformations within the nucleus of atoms. The great advantage of this system is the high specific impulse and thrust level. The high system complexity and in some extent the political issues, are some of the disadvantages of this propulsion system. Safety issues could be a problem, but these engines can be designed to operate under safety conditions. Although the author does not know of operational systems of this type, studies seem to suggest that with the NRE, interplanetary voyages time is reduced in comparison with chemical engines. So the NRE will reduce cosmic radiation exposure. One example of this type of propulsion system is the Cassini/Huygens spacecraft engine.

Other way of classifying the rocket systems is related with its applications. Zandbergen (2007) refers that the most common practical uses of rocket systems are as weapons of war (missiles and anti-tank weapons), commercial and peaceful space exploration (space launchers <sup>1</sup>, orbit transfer, orbit acquisition/trim, repositioning, de-orbit, plane changes, etc). Rockets applications are also found in sounding/research rockets, amateur rockets, ejection seats, rocket assisted take off (JATO - jet assisted take off), race cars (rocket dragster), gas-generators (micro gas generators are used as air-bag inflators).

---

<sup>1</sup> An example of a space launcher is Ariane 5, as can be viewed in Appendix A.

## 2.1 Hybrid Rocket Propulsion

According to Casalino and Pastrone (2002) there is a great interest in Europe for the Hybrid Rocket Propulsion (HRP or HPRE) as an option for low cost propulsion system for small satellites orbit transfer. The hybrid engines characteristics are very competitive in many applications, from great launchers to small altitude control and orbit transfer thrusters.

Humble et al (1995) distinguishes between typical hybrid rocket engines, where the oxidizer is in liquid phase and the fuel is in solid state, and the reverse hybrid rocket engines consisting of solid oxidizer and liquid fuel. Due to this separation of oxidizer and fuel in two different states, the combustion of hybrid rockets differs from the solid and liquid rockets. In both of these, one little combustion chamber volume element contains a uniform mixture of oxidizer and fuel. In turn, the HPRE burns the fuel with a macroscopic diffusion flame, where the oxidizer-to-fuel ratio varies along the combustion grain port length.

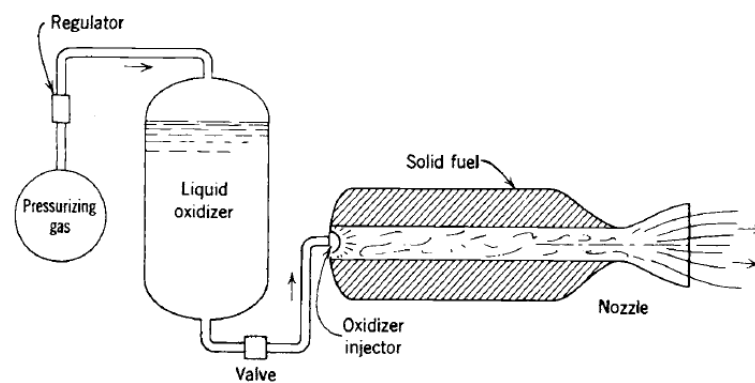


Fig. 2.1 – Hybrid Propulsion System more common in rocketry (Sutton, 1992).

In Fig. 2.1, it is represented the most usual hybrid rocket configuration. Special note should be made to the use of a pressurized equipment, so that it can maintain the same pressure level inside the oxidizer tank.

### 2.1.1 Advantages and Disadvantages of HRP

According to Sutton (1992), Humble et al. (1995) and to Jansen and Kletzkine (1998), the main advantages of the HRP are:

- Greater safety during manufacturing, storing and operation;
- The engine can be controlled by the flow rate of the liquid propellant, which controls the burn rate of the solid propellant (in liquid rockets engines, both bipropellant flows rate must be synchronized and modelled), this throttling feature is very useful;
- Start-Stop-Restart capabilities reflecting an engine more flexible;

- For various propellant combinations, the exhaust gases are environmentally safe;
- Potentially more reliable than the solid fuel propulsion system (the composition of fuel grain is stronger and inert in hybrid systems, therefore insensitive to overpressure due to fissures and cracks which occur occasionally in solid propellant grains) or in the liquid bipropellant system (hybrid rockets have less needs for plumbing and pumping, since there is only one liquid component to be handled);
- Possibility of introducing additive materials, such as aluminium, on solid fuel of typical hybrid rocket engines, which permits to increase the specific impulse, get advantage in density over hydrocarbons LPRE, reduce the oxidizer-fuel ratio to produce the maximum specific impulse and consequently a reduction of the liquid oxidizer;
- Design is relatively simple and also low-cost;
- Higher specific impulse than in SRMs and higher-density impulse than liquid bi - propellant engines;
- Possibility of smooth thrust change over a wide range on demand;
- Good performances.

According to the same authors, the main disadvantages of a Hybrid Rocket Engine are:

- The mixture ratio and the specific impulse varies during the steady-state operation and throttling;
- Small regression rate, for combustion chambers higher than 30 cm diameter, the fuel grain needs multiple combustion ports, which can be an advantage for long term applications, such as mobile targets and gas generator;
- Efficiency in nominal steady-state combustion are in the range of 93 to 97 %, which is slightly lower than liquid and solid systems;
- System density impulse is small, this means that needs more volume than solid propellant systems;
- The mass fraction of the engine is slightly reduced due to some fuel sliver that usually is retained in the combustion chamber at end-of-burn;
- Oxidizer-to-fuel ratio varies with the increase of combustion grain port diameter during burning, which can reduce the HPRE performance, but these losses can be minimized in a good design;
- Heat transfer problems during long operation periods of time;
- Design presents some difficulties due to the lack of experimental data for some propellants combinations.

### **2.1.2 Applying conditions of the HRP**

When safety and reliability are of concern, hybrid propulsion systems can be applied. Practically, it possesses all merits of modern Liquid Rocket Engines (LRE or LPRE) and Solid Rocket Motors (SRM or SPRE). Other important aspects are the simplicity and the cost of those systems. Environmental questions are becoming more and more important nowadays. HRP can be a good solution, since there are hybrid engines using non-toxic propellants.

Other conditions for applying the HRP are:

- The fuel and the oxidizer, needs to be in different physical states, i.e., oxidizer vapour/liquid – fuel solid or oxidizer solid – fuel vapour/liquid;
- When requires Start-Stop-Restart capabilities;
- When it is needed throttleable capability.

## 2.2 History and recent developments of HPRE

The concept of HRP is not new, as can be seen from the Fig. 2.2.

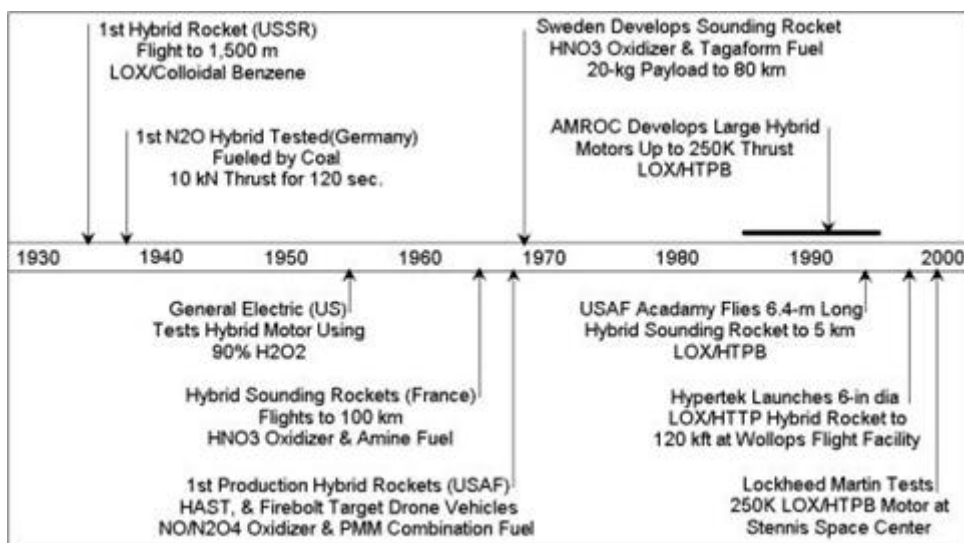


Fig. 2.2 – Hybrid Rocket Engine history until 2000 (Zandbergen, 2013).

In the last decade we have observed an increase in hybrid rocket propulsion engines (HRPE) projects. This is due to HRPE having a safe and reliable combustion process. Also it has small costs of development and comparatively cleaner environmental characteristics. Moreover, designers see in the small specific impulse (related with low regression rate) and the combustion efficiency, two points to develop even more.

Chang et al. (2005) highlight exactly that HPRE recover their attention not only because of the safety issues in the combustion process and the small development costs, but also because of its low specific impulse, which represent areas of opportunities to research and development.

The Korting et al. (1987) research results and experiments showed that the regression rate is affected by the following factors: the mass flux, the geometry, the pressure level, the presence of oscillation, the oxidizer composition and the burning time. Polymethylmethacrylate (PMMA) and polyethylene (PE) was used as solid fuel and gaseous oxygen (GOX) was used as oxidizer. The pressure interval in study was from 0.3 to 2.0 MPa. The regression rate varied from 0.2 to 1.0 mm/s (mean values), with high initial spikes.

The regression rate research of the propellant pair HTPB (solid fuel) and the oxygen (oxidizer) was done by Chiaverini et al. (2000). The hybrid motor geometry was laboratorial scale, allowing a radiography system to obtain, on real time, data of the instantaneous solid fuel regression rate in any axial position. It was also tested the effect of adding activated aluminium powder in the solid fuel. An addition of 20 % of the activated aluminium weight in the HTPB solid fuel represented a 70 % increase in the fuel mass flow, relatively to the HTPB pure case.

Risha et al. (2002) have done experiments to determine one combination of HTPB and additives of nanometric dimensions, such as aluminium, boron, boron carbide, covered and uncovered aluminium flakes.

Other research involving the HTPB solid fuel and ammonium perchlorate and aluminium additives was made by George et al. (2001). Here the regression rate was improved while reducing the port diameter and the addition of the mentioned additives. Nevertheless, the aluminium addition showed more significant results.

Karabeyoglu et al. (2004) identified a class of paraffin fuel that burns at high regression rate and proposes a burning model. The improvements involve using a material that while in fusion forms a liquid hydrodynamically unstable surface in the fuel.

A higher scale test series with GOX hybrid engines were conducted in the Hybrid Combustion Facility (HCF) of NASA Ames Research Center. These tests showed nice agreement with the small scale, lower pressure and small mass fluxes conducted by the Stanford University laboratories. Therefore, it confirmed a higher regression rate to solid fuels based on paraffin with chamber pressures and mass fluxes conditions representative of commercial applications.

The first applications of HRPE were as sounding rockets, launch vehicles, micro satellites and tactical missiles. Nevertheless, nowadays, this technology is applied in substitution of solid launchers and also in sub-orbital manned vehicles, like *Space Ship One* and more recently the *Space Ship Two* (see Fig. 2.3)



(a)



(b)

Fig. 2.3 - *Space Ship One* (a) and *Space Ship Two* (b) from Scaled Composites.



In 2004 the Lockheed Martin Space Systems Company, with the Stanford University, and following the Karabeyoglu et al (2004) researches, launched two sounding rockets of 4 in external diameter, based on hybrid technology and paraffin-N<sub>2</sub>O propellant pair.

Santos et al. (2004) conducted experimental investigations in hybrid rockets based on paraffin fuel and GOX and N<sub>2</sub>O oxidizer, with 200 N thrust. The results showed better behaviour of the paraffin against polyethylene.

Almeida and Santos (2005) designed, built and launched two hybrid rockets prototypes based on paraffin and nitrous oxide. It is believed to be the first paraffin hybrid rockets launches in Latin America.

SD-1 is another paraffin-N<sub>2</sub>O hybrid rocket engine designed and launched by Contaifer (2006). The prototype reached 5000 m height and transported an onboard computer and a recovery system.

The most commonly combined propellant solutions used in HRPE are the ones using hydroxyl-terminated polybutadiene (HTPB) as solid fuel. In Fig. 2.4, we can see the performance differences in using several liquid oxidizers with HTPB solid fuel.

Examples of engines, using the HTPB fuel are the Unity IV (1995), from Brigham Young University and the Utah State University, both from Utah, USA. The Unity IV, used as oxidizer gaseous oxygen. In 2003, it was launched a larger version, again with HTPB as solid fuel and now nitrous oxide as oxidizer.

Synthetic rubber, a common name for HTPB, as solid fuel and the nitrous oxide as oxidizer, better known as laughing gas, are the propellants for the *Space Ship One*. These engines were partially based on the results of AMROC (American Rocket Company) studies at E1 test facility in *NASA Stennis Space Center*. Here engines ranging from 4.4 kN to 1.1 MN thrust were successfully tested. Beyond this power range, *SpaceDev* tested engines using PMMA (Plexiglas) solid fuel and several oxidizers, like liquid oxygen (LOX), nitrogen oxide (N<sub>2</sub>O) and hydrogen peroxide (H<sub>2</sub>O<sub>2</sub>).

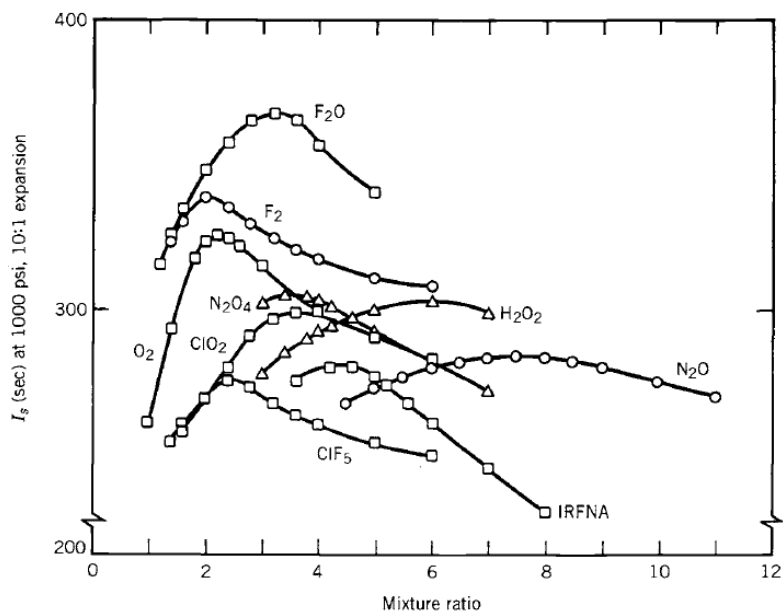


Fig. 2.4– Theoretical vacuum Specific Impulse of several liquid oxidizers for HTPB solid fuel (Sutton, 1992). Note that the mixture ratio is the oxidizer-to-fuel ratio.

Gouvêa (2007) investigated the application of paraffin-H<sub>2</sub>O<sub>2</sub> as a propellant pair for a 70 N hybrid rocket motor. Using a computational chemical equilibrium code, the author predicted the propulsive characteristics of these propellants.

A special remark for the combination of N<sub>2</sub>O and HTPB should be made, because is a non-toxic and benign combination. N<sub>2</sub>O at room temperature can be stored and self pressurized to 4.83 MPa. Recent studies carried out by Stanford University and by Universidade de Brasília on N<sub>2</sub>O and Paraffin combinations, show higher burning rates than using N<sub>2</sub>O and HTPB, while maintaining the non-toxic feature.

Zakirov et al. (2001) tested the use of nitrous oxide as propellant and compared with other conventional propellants. In this research it was concluded that nitrous oxide is a promising propellant for small and low cost satellites future missions.

Bertoldi (2007) established new values for the regression rate constants of a hybrid rocket engine working with paraffin and nitrous oxide as propellants.

Nevertheless, due to some accidents with nitrous oxide, handling precautions and procedures should be made, Thicksten et al. (2008). Karabeyoglu et al. (2008) presented a model of the nitrous oxide decomposition events. Besides its potential decomposition hazard, if handled properly, N<sub>2</sub>O is one of the safest oxidizers being used in rocket propulsion systems, nowadays.

Other non-toxic hybrid rocket propellant pair is oxygen and beeswax. This pair showed a regression rate at least three times as high as traditional hybrid propellant combinations such as hydroxyl-terminated polybutadiene (HTPB) and liquid oxygen(LOX). This was tested and developed by the Tennessee University, due to environmental concerns raised from the food and subsoil water contamination by rocket propellants, Lyne et al. (2005).

Carmicino and Sorge (2005) performed several tests to investigate the oxidizer injection influence in the solid fuel regression rate behaviour on HPRE. A conic subsonic nozzle was used to feed the GOX in a non-uniform condition at the circular polyethylene fuel grain port entry. Using a ultrasound pulse-echo technique, it was possible to measure the instant local regression rate, and observed that this type of injector strongly increase the regression rate in the fuel grain surface region where the oxygen collide.

## **2.3 Project motivation and innovation: what is new?**

As described before, the HPRE has a great development potential, which may turn it even more appellative for future space missions and other applications.

The present project's goal is to improve the hybrid rocket engine. For this, it is intended to make use of the thermal energy available in the walls of the exhaust nozzle and combustion chamber, to pump the oxidizer into the engine.

From Fig. 2.5, it is known that the highest heat transfer rate must occur at the throat section of the nozzle. Therefore, heat transfer effects should be taken into account in the design of the nozzle, particularly, in the choice of materials. Note that, from the mixing zone of the combustion chamber to middle of the nozzle expansion region, the heat transfer is more than  $1 \text{ MW/m}^2$ .

From Fig. 2.1, it is understandable that the pressurizing gas tank and its apparatus will not be needed anymore with this new concept. Also it is intended that the control mechanisms, most of them expensive, unreliable and particularly heavy, of the conventional HPRE are eliminated. This would simplify the common HPRE, becoming lighter and even more reliable. From the structural point of view, it is intended to use mechanically and thermally resistant, but also light, material.

In the same way, it is intended to use cheap propellants, with the lowest possible pollution levels, that permits simplified ignition mechanisms.

The idea of this project is to develop a conceptual hybrid engine that uses the heat transfer, from the nozzle walls to the surroundings, to pressurize the oxidizer inside the tank. This idea is proposed in Pardal (2012) patent.

Zakirov and Li (2005) and Whitmore and Chandler (2010) presented two self-pressurizing models using high pressure saturated nitrous oxide inside tanks. On one hand, Zakirov's model takes into consideration heat transfer through tank walls, but does not take into consideration possible boiling of the oxidizer. On the other hand, the Whitmore's model assumes an adiabatic expansion and a vapour fluid evacuation mass flow through an outlet orifice.

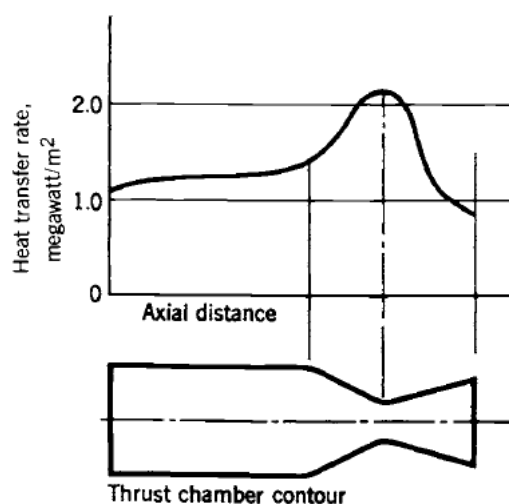


Fig. 2.5 – Common heat transfer distribution along the rocket engine (Sutton, 1992).

## 2.4 Propellant trade-off study and selection

A brief propellant trade-off study is presented in this section (see Fig. 2.6). An initial selection is made of propellant combinations (oxidizer and fuel pairs) which are then evaluated in aspects important for the selection. Choosing propellants for a certain mission is a very important step for the design of the propulsion system and aspects such as level of performance, costs and environmental impact must be taken into consideration. Safety factors and ease of use, as well as the specific goals, are also key factors.

### 2.4.1 Candidate combinations

The candidate combinations selected for a trade-off study that determined the propellant choice for the present proof of concept engine are given in Tab. 2.1 and Fig. 2.6.

The combination of nitrous oxide and hydroxyl-terminated polybutadiene (HTPB) is one of the most common in hybrids. In fact, this combination was already used successfully in manned suborbital craft, like Space Ship One from SC (2013), and is also widely used in amateur rocketry. The same oxidizer used with paraffin is also known and has been studied by the SPG (2013), among others.

Use of oxygen as oxidizer with either fuel has also been considered. Oxygen is one of the best known and best performing oxidizers in rocketry. However, oxygen has issues that may limit its usefulness with the present system, or at least at the current initial stage of development, as will be discussed in the next section.

Oxidizer	Fuel	Abbreviation
Nitrous oxide (N <sub>2</sub> O)	Hydroxyl-terminated polybutadiene ((C <sub>4</sub> H <sub>6</sub> ) <sub>n</sub> )	N <sub>2</sub> O/HTPB
Nitrous oxide (N <sub>2</sub> O)	Paraffin wax (C <sub>20</sub> H <sub>42</sub> )	N <sub>2</sub> O/Par.
Oxygen (O <sub>2</sub> )	Hydroxyl-terminated polybutadiene ((C <sub>4</sub> H <sub>6</sub> ) <sub>n</sub> )	O <sub>2</sub> /HTPB
Oxygen (O <sub>2</sub> )	Paraffin wax (C <sub>20</sub> H <sub>42</sub> )	O <sub>2</sub> /Par.

Tab. 2.1 – Propellant combination candidates.

## 2.4.2 Brief discussion on the several options considered

### 2.4.2.1 Suitability of the proposed system

The main strengths to be incorporated in the proposed system are simplicity, safety and low cost. These characteristics naturally depend on the choice of propellants. To be suitable to the proposed system, the selected propellants must have characteristics that not only lead to the aforementioned strengths in the overall system, but that are also suitable to take full advantage of the features inherent to this system.

Being a hybrid engine, all the considered combinations include a component that is solid at storage temperatures. In most of the cases, this component is the fuel. Both HTPB and paraffin wax are hydrocarbons and they share characteristics that make them suitable to the proposed system. They are easy to handle and store, non-toxic, easily available and usually have sufficiently good regression rates. Neither of them includes metallic particles, although the option to add them at a future stage of development is not completely discarded. In this respect, they are both suitable to accommodate such addition.

Regarding oxidizers, there are differences that are important to consider. These differences are illustrated in Tab. 2.2.

A benchmark case where oxidizers are stored in a tank at a common pressure of 45 bar was considered. For this comparison, nitrous oxide is considered as a phase mixture (with a quality of 0.1, which means it's mostly liquid) and oxygen is considered both in purely gaseous form (compressed gas) and as a phase mixture with the same quality.

	<b>N<sub>2</sub>O (sat)</b>	<b>O<sub>2</sub> (g)</b>	<b>O<sub>2</sub> (sat)</b>
<b>Storage temperature [K]</b>	288.1	294.7	151.7
<b>Storage pressure [bar]</b>	45	45	45
<b>Storage density [kg/m<sup>3</sup>]</b>	752.3	60.4	599.1
<b>Specific enthalpy of vaporization, h<sub>fg</sub> [J/kg]</b>	188730	-	66624
<b>Specific enthalpy variation for 300 K, Δh [J/kg]</b>	199540	5958	249769

Tab. 2.2 – Some properties of oxidizer candidates comparison. A quality of 0.1 for saturated phase mixtures is considered in above properties. (NIST, 2013)

As the table shows, at the considered pressure, both saturated nitrous oxide and gaseous oxygen can be stored and used at ambient temperatures, although the density of gaseous oxygen is one order of magnitude lower than that of nitrous oxide, which indicates it would need a storage tank one order of magnitude larger (in volume) for the same mass of oxidizer. In order to have the same storage pressure, saturated oxygen would need to be kept at a cryogenic temperature, in which conditions the density of a 0.1 quality mixture is still inferior (although in the same order of magnitude) as that of nitrous oxide.

Regarding vaporization conditions (for the saturated oxidizers), the enthalpy of vaporization for the case of oxygen is about three times lower than that of nitrous oxide. For injection in the same conditions (45 bar, 300 K), the specific enthalpy required for nitrous oxide to reach the established conditions is less than that of oxygen stored under saturated conditions (although the different amounts required of each oxidizer for stoichiometry will reverse this difference). The higher enthalpy thus required for the vaporization of a suitable amount of nitrous oxide can also be viewed as a better capability to soak up waste heat from the nozzle without having to reject it to the outside. Considering this, nitrous oxide presents itself as more advantageous in a properly designed engine.

Finally, and regarding the possibility of sonic injection it is interesting to compare the flow rate conditions for a sonic throat in both gases. Tab. 2.3 shows the product of gas density and speed of sound for reference conditions.

	<b>N<sub>2</sub>O</b>	<b>O<sub>2</sub></b>
<b>ρ·a [kg/m<sup>2</sup>.s]</b>		
@ 300 K	25132	19648
@ 180 K	-	28456

Tab. 2.3 – Flow rate coefficients comparison for a sonic throat. Values are at reference pressure of 45 bar. (NIST, 2013)

As the numbers show, if oxygen is used, it is more favourable to use lower temperatures from the point of view of maximizing flow rate for a given throat area. If the two oxidizers are compared at the same temperature of 300 K, nitrous oxide has an advantage.

### 2.4.2.2 Performance and safety

Performance is not a critical point at this early stage of engine development. However, it is important to consider it, since a system which is limited by its development to propellants with a very low performance may be severely penalised when scaled up to operationally useful sizes.

A performance case study was made to compare the different propellant combinations. For a given (approximate) fuel mass, the stoichiometric ratio and the corresponding oxidizer mass were calculated (Tab. 2.4).

Propellant combination	Oxidizer/Fuel	Fuel mass (kg)	Oxidizer mass (kg)
<b>N<sub>2</sub>O/HTPB</b>	8.95	0.795	7.115
<b>N<sub>2</sub>O/Par.</b>	9.50	0.769	7.308
<b>O<sub>2</sub>/HTPB</b>	3.25	0.795	2.584
<b>O<sub>2</sub>/Par.</b>	3.45	0.769	2.653

Tab. 2.4 – Stoichiometric conditions for case study combinations.

As the table shows, in stoichiometric conditions the necessary nitrous oxide mass is larger (roughly three times larger) than that of oxygen, which hampers its advantages in terms of achieving a larger flow rate through the same sonic throat and having a better rate of vaporization.

A performance comparison in stoichiometric conditions was made using NASA CEA 2<sup>2</sup>. For this analysis, a benchmark pressure of 10 bar in the combustion chamber was considered. Initial reactant temperatures considered were 300 K for nitrous oxide, 180 K for oxygen, 330 K for paraffin and 370 K for HTPB.

As Tab. 2.5 shows, the oxidizer is more decisive in the performance than the fuel. Specifically, liquid oxygen outperforms nitrous oxide, with around 10% better specific impulse. Although this added performance is relevant in operational terms, it is not strictly necessary to prove the concepts and innovations proposed. Also, the difference is not large enough to rule out nitrous oxide as an option in larger engines, since it can be offset by the lack of some of the disadvantages of using oxygen which would bring a penalty to the system as a whole.

Regarding safety, both oxidizers have relevant issues that need addressing. The main hazards of handling liquid oxygen are the low temperatures involved and the corrosiveness of the oxidizer. Addressing these issues requires adequate procedures and equipment which requires higher investments.

<sup>2</sup> The NASA Computer program CEA (Chemical Equilibrium with Applications) calculates chemical equilibrium compositions and properties of complex mixtures. Applications include assigned thermodynamic states, theoretical rocket performance, Chapman-Jouguet detonations, and shock-tube parameters for incident and reflected shocks. CEA represents the latest in a number of computer programs that have been developed at the NASA Lewis (now Glenn) Research Center during the last 45 years.

Propellant combination	Exhaust gases properties					
	Flame temperature	Density	Isentropic expansion factor	Molar mass	Exhaust velocity	$I_{sp}^3$
	[K]	[kg/m <sup>3</sup> ]		[kg/kmol]	[m/s]	[s]
<b>N<sub>2</sub>O/HTPB</b>	3263	0.9971	1.1396	27.123	2003	204
<b>N<sub>2</sub>O/Par.</b>	3190	1.005	1.1385	26.534	2004	205
<b>O<sub>2</sub>/HTPB</b>	3529	0.8523	1.1253	25.008	2183	223
<b>O<sub>2</sub>/Par.</b>	3408	0.8532	1.1213	24.173	2186	223

Tab. 2.5 – Case study performance parameters.

Nitrous oxide is generally considered to be a safer substance to handle, although it is not without its own hazards. The main hazards include explosive decomposition and overpressure. These can be addressed by some of the practices and procedures that would be used with liquid oxygen (ensuring cleanliness standards, material compatibility, etc...) but the temperature control requirements are not as demanding as with liquid oxygen. Although there have been some well-publicized accidents involving nitrous oxide (Berger, 2007, Karabeyoglu et al., 2008, Scaled Composites, 2009 and Thicksten et al., 2008), the causes of these are now well understood and the propellant is considered to be one of the overall safest oxidizer choices in rocketry.

Further safety considerations about the selected oxidizer are given in section 2.4.4.

### 2.4.2.3 Acquisition and handling

Acquisition and handling considerations are, once again, dominated by the oxidizer. Both HTPB and paraffin wax can be obtained easily and cheaply.

Paraffin melting point is relatively low (which is connected to its good performance as solid fuel for hybrid rockets) and this makes it easy to cast into grains of various shapes. In this regard, paraffin may have a certain advantage since it allows easier casting and potential mixing with any additives that may come to be used in the future (Bertoldi, 2007). Note that paraffin waxes are hydrophobic, making them an ideal binder for metal, metal hydride or dense organic additives. Several paraffin waxes of different molecular weights can also be easily mixed to optimize engine performance.

In terms of oxidizers, both candidates have distinct acquisition and handling characteristics. As mentioned before, oxygen requires cryogenic temperatures for storage.

<sup>3</sup>  $I_{sp}$  is the specific impulse which is defined in Appendix B.



Aside from the options mentioned in 2.2.1, in theory, it is possible to store oxygen as a liquid at atmospheric pressure if temperatures below 90 K could be maintained. In this case, boil-off losses can be high and venting is a necessity after the tank is full. For the proposed system the common problems that may arise from valve freezing are not so critical since the injection is made with the gaseous phase of the oxidizer. Regarding costs, liquid oxygen is cheap on a per-quantity basis, but the requirement for suitable installations to handle it and potential minimum order issues may create difficulties in sourcing and handling this oxidizer for use in the current development effort.

On the other hand, nitrous oxide presents a different set of challenges. Although not requiring very low temperatures for storage, the proximity between its critical temperature (309.52 K) and normal room temperature causes the vapour pressure to be fairly high, which requires a suitable high pressure tank. The large variations of the vapour pressure with small changes in temperature must also be accounted for in the tank and piping design, often requiring some venting as well. Regarding costs, nitrous oxide is more expensive than liquid oxygen, but requires less infrastructure and equipment cost for safe handling and usage. Overall, it is considered easier and cheaper to use.

### 2.4.3 Selection

With all the aforementioned considerations in mind, a selection of oxidizer is made for nitrous oxide. Although liquid oxygen has advantages in performance and suitability to the proposed system, its storage and handling drawbacks were viewed as prohibitive at this stage.

Regarding the fuel, the choice is easier. Paraffin has slightly better handling characteristics and performance. To the lack of relevant compensating advantages on the side of HTPB, paraffin was selected as the fuel.

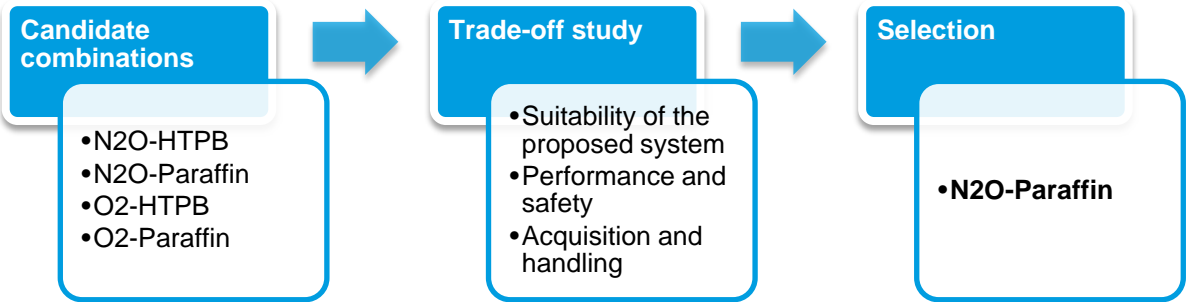


Fig. 2.6 - Propellant trade-off study and selection.

## 2.4.4 Safety considerations

Important safety issues can also rise from improper engine and tank design. Therefore, this section covers in some extent the safe usage of nitrous oxide in general and provides design guidelines for the next chapter, which covers some relevant aspects to be taken into account in the design of the hybrid rocket engine.

### 2.4.4.1 Possible issues

According to the literature consulted, like Berger (2007), Thicksten et al. (2008), Karabeyoglu et al. (2008) and Scaled Composites (2009), when using nitrous oxide, the main issues to look out for are:

- Heat sensitivity
- Material incompatibilities
- Oxidizer absorption and contamination
- Adiabatic compression of vapour
- Static discharges
- Flash-boiling of nitrous oxide
- Flashback
- Localized chilling

Heat sensitivity issues are twofold. On the one hand, at near room temperature conditions, nitrous oxide is near saturation. In fact, the proposed engine works in such conditions by design. In these conditions, the vapour pressure varies greatly with relatively small changes in temperature. This means that a small increase in temperature may lead to significant over - pressures, a possibility that must be considered for designing.

On the other hand, nitrous oxide can behave as a monopropellant. Above a certain temperature threshold (which becomes lower with increasing pressure), an exothermic decomposition reaction is initiated. This problem is prevalent in the gaseous phase of the oxidizer, although the literature indicates that it does not occur in the liquid phase. This hybrid engine, even more than others may have a significant source of heat, with the combustion chamber and the nozzle in the close vicinity of the tank. This issue is likely to be a main design driver for the engine layout.

Aside from pressure, another determining factor in the decomposition temperature threshold in the presence of incompatible materials. A non-extensive list of those materials includes:

- Copper alloys and copper oxides
- Nickel alloys
- Platinum
- Iron oxides

The aforementioned materials act as catalysts for the decomposition reaction of nitrous oxide and their contact must be avoided with the oxidizer. Non stainless steels should also be avoided, since they are liable to produce rust (iron oxide). Stainless steel and aluminium alloys are generally considered compatible in the literature.

When it comes to (rigid) polymers, only polytetrafluorethylene (PTFE), polychlorotetrafluorethylene (PCTFE), and polyethylene terephthalate (PET) are considered compatible. Other plastics behave as fuels, and mixing them with nitrous oxide creates a potential explosion hazard.

Furthermore, nitrous oxide has been known to be absorbed by several plastics, including epoxy resin matrices in composite materials. A plastic saturated with nitrous oxide is effectively a high explosive.

Similarly, contamination of the oxidizer by substances that may act as a fuel, such as incompatible lubricants, grease or others may substantially lower the activation temperature for an explosive reaction. In this case, a localized combustion may provide the initiation energy to start a much wider exothermic decomposition reaction.

Adiabatic compression is another possible ignition source for a decomposition reaction in the piping. This phenomenon usually occurs just upstream of closed valves or flow restrictions, when a valve further upstream is opened and the momentum of the flowing gas is converted to heat when it encounters the restriction. This heat is usually insufficient to start a reaction by itself, but it may be more than enough to ignite slightly contaminated oxidizer. Adiabatic compression can also occur in other places in the piping where a localized increase in pressure occurs, such as pipe bends or sudden contractions.

Another possible and more obvious ignition source is an electrical discharge. The entire system should be properly designed so as to avoid any build ups of static electricity and any electrical discharge, especially near fill and drain valves, vents or pressure relief devices.

Flashback of a reaction front from the chamber to the piping and tank is another possible issue. Although this engine concept involves by design a sonic gaseous oxidizer injection into the combustion chamber, something which cannot be accomplished without a suitable pressure difference relative to the tank, care must be taken so as to not allow a severely off-design condition to occur, in which a decomposition wave flows back into the tank.

In general, although combustion with vapour phase oxidizer is at the core of the system, it is undesirable to have a large amount of it at any time in the system. Two particular situations may lead to this: a combustion chamber filled with unreacted oxidizer, and a nearly empty tank with much of its volume already occupied by vapour. The first situation is avoidable with good engine design practices. However, the latter situation is unavoidable without a large propellant waste. Since the basic concept of this system is to heat the oxidizer for self-pressurization, contact between the heat source (tank wall or heat exchanger) and the vapour phase poses a serious risk and the design should carefully take this into account.

The final issue considered does not necessarily lead to immediate catastrophic failure but may nonetheless cause problems. Any nitrous oxide vent will be subject to cooling due to the expansion of the gas from its high vapour pressure to ambient pressure. This cooling, although useful to detect leaks in tank and tests piping, may cause icing and damage the vents and drain valves, as well as injury any operators not suitably protected.

#### **2.4.4.2 Design guidelines**

##### **2.4.4.2.1 Design features against overpressure**

In order to cope up with possible overpressures, there are two main strategies to be used. One of them is to use a suitable safety factor for the tank, piping and other pressurized components. Since the proof of concept for this tank is not to be made with a flight vehicle, weight is a less substantial issue and therefore greater factors of safety may be used. A safety factor above three, based upon the critical point pressure of the nitrous oxide can be considered acceptable, making the minimum burst pressure for the tank 210 bar. Aside from this large safety factor, a pressure relief device should also be employed in the tank. This device may be either a relief valve or a burst disk.

##### **2.4.4.2.2 Design features against unintended ignition**

The recommended design features against unintended ignition are aimed primarily at preventing such ignition. To do that, it is useful to recall from the previous section the potential sources of unintended ignition (both for combustion and decomposition reaction) considered:

- Contact of the gaseous oxidizer with hot surfaces;
- Adiabatic compression of the gaseous oxidizer;
- Electrical discharge near the gaseous oxidizer;
- Flashback from the combustion chamber;
- Decomposition catalysis due to incompatible materials and
- Abnormally low ignition threshold due to oxidizer contamination.

Considering that, by design, at least part of the tank surface will be purposefully heated, the challenge in preventing contact of the gaseous phase with hot surfaces is mainly centred around limiting the hot tank surface to an area that will only contact the liquid portion of the oxidizer. The geometry of the tank should play an important role solving this problem. Another relatively simple solution is to add diluting gases to the nitrous oxide. Literature suggests that molecular nitrogen, molecular oxygen or helium would be suitable candidates. Carbon dioxide would be another suitable candidate, which has the advantage of having physical properties that are very similar to those of nitrous oxide itself. The dilution ratings can be higher than 30%. These considerations will be further elaborated upon in the test planning.

The possibility of adiabatic compression is most adequately prevented with suitable test procedures (which will be defined further ahead in the project). As far as design is concerned, the greatest concern is to ensure smooth internal flow in the piping, without sudden contractions or geometry that can give rise to shockwaves. For another reason, sudden expansions should also be avoided, since the recirculating flow they induce can act as an effective flame trap for any reaction initiation events. Some care should also be taken in selecting valves with adequate internal geometry and minimizing dead volumes between valves.

To prevent ignitions caused by electrical discharge, all the components of the engine should be well grounded, and electrically conducting materials should be preferred.

The risk of flashback from the combustion chamber refers to enough energy moving upstream to initiate a decomposition reaction within the piping. Properly calculated operating parameters should minimize this risk, and a flashback arrestor comprised of a bundle of tubes may also be used. The tubes should act to quench any reaction initiation, absorbing excess heat from the nitrous oxide.

A common source of concern for the space industry is materials incompatibility. There are well known suitable materials for the engine design and manufacture. The main materials to be used should be the aforementioned aluminium alloys and stainless steels for the tank, valves and piping. According to the literature consulted, sealing should be performed preferentially with fluorocarbon or PTFE-coated O-rings and lubrication should ideally be made with perfluoropolyether grease (commercial name: Krytox, CAS registry number: 60164-51-4). Valve seals on the valves used should also be checked for compatibility.

Finally, oxidizer contamination is best countered with thorough cleaning procedures (to be further described in a test plan). At design level, however, geometry should be defined so as to avoid potential sites of contaminant accumulation (such as internal corners) and to ease the cleaning procedure.

## 3 Methodology

In this chapter the preliminary design methodology of the new conceptual type of hybrid rocket motor is presented. A first theoretical design work will deliver the input project values necessary to the computer simulation of the motor. Here, the numerical work will take into consideration a simplified heat transfer model from the nozzle walls towards the wet region of the oxidizer tank. A model of the combustion and nozzle flow is also included, as well as for the oxidizer feeding system and the oxidizer tank model. In fact, to understand the oxidizer behaviour inside the tank as it exits through an orifice, as well as receiving or not heat transfer from the walls, experimental work is done and presented.

### 3.1 Hybrid rocket design

In this section, it is presented a layout of the conceptual hybrid rocket engine. The design starts with sizing, which involves scale parameters of the project, but also burning, injection and exhaust parameters, which will be fundamental for chamber and nozzle geometry calculations. Besides that, a heat transfer system is also sized. Some material selection issues are addressed.

#### 3.1.1 Hybrid rocket layout

The new conceptual hybrid rocket system is to be composed of five main components (see Fig. 3.1):

- Oxidizer tank;
- Oxidizer piping, flow control and injection orifice;
- Combustion chamber;
- Exhaust nozzle;
- Heat transfer system.

These five main components form a closed loop, during operation. The goal is that all these components interact with each other in an expectably stable manner to ensure the operation of the engine.

For a test demonstrator, the actual layout will include an axisymmetric combustion chamber and nozzle, which should be mounted on a test stand. The feeding line should be installed on the upper side of the oxidizer tank in order to allow only vapour oxidizer flow. The contact surface between the oxidizer tank and the heat transfer system should be maximized.

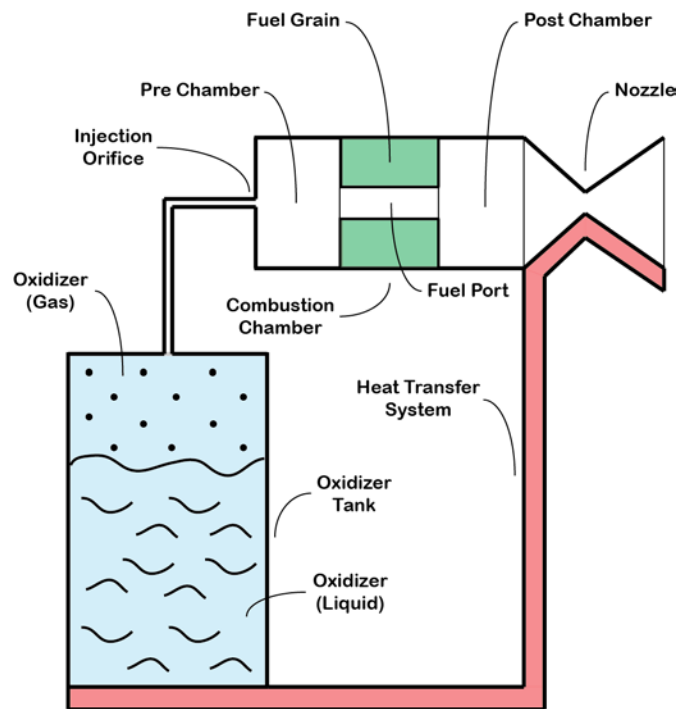


Fig. 3.1 – Project hybrid rocket layout.

The relative position of the oxidizer tank and the combustion chamber and nozzle imposes restrictions on the injection piping and also on the feedback heat transfer system. The first may easily accommodate greater separation between the components on a test stand. The latter does not easily accommodate a large distance between the nozzle and the tank without introducing an undesirable extra amount of thermal inertia. In case the test plan and procedures (in future developments) indicate that the oxidizer tank and the combustion chamber should not be in very close proximity, the heat transfer may be made indirectly, with the nozzle being cooled by its own cooling system and a proportional amount of heat being transferred to the oxidizer tank by a separate, electronically-controlled heater.

## 3.1.2 Hybrid rocket sizing

### 3.1.2.1 Scale parameters

The sizing of the proof of concept demonstrator engine is based on an expected burn time, which determines the length of the test, and a nominal exhaust mass flow rate, which determines the size of the engine and the thrust developed. After these two parameters are fixed, the physical dimensions and the operating parameters of the engine can be set and the components of the engine can be designed.

Burn time for a demonstration firing was considered the primary variable for overall sizing. A burn time that is too short may not be conclusive enough to demonstrate viable operation for longer times. A burn time that is too long requires an oversized system, with a greater amount of propellant loaded (potential energy) and may not bring additional benefit. A value of 15 seconds was considered relevant enough for a proof of concept level, without being unnecessarily long. Moreover, this burn time is common to the burn times of research hybrid rockets, as can be found in reviews of the state-of-the-art, like Bertoldi (2007).

The (average) exhaust mass flow rate was selected as a variable to determine the size of the system, since it is proportional, for the chosen burn time, to the physical size of the demonstrator, the amount of propellant involved and the thrust developed. It is important to maintain the physical size at a level which keeps prototype manufacturing costs low, while the amount of propellant involved and the thrust developed (which will drive the design of the test stand) should also be kept low, but not so much that makes the tests inconclusive with regard to viability and scalability of the system. A value of 0.1 kg/s was chosen for the exhaust mass flow rate. This will put the total mass of propellants for each firing at 1.5 kg, which is a reasonable value to be handled and allows for a sufficient number of tests with a reasonably sized bottle of oxidizer (around 25 tests for a 37 kg bottle). The thrust developed, which will condition the choice or development of the test stand, should be on the order of magnitude of  $10^2$  N, as could be understandable from data of Tab. 2.5

### 3.1.2.2 Burning parameters

Regarding the burning parameters, the main nominal burn parameter to be defined is the oxidizer-to-fuel ratio (OF). Here the regression rate for the nitrous oxide - paraffin pair was assumed as the one established by Bertoldi (2007):

$$\dot{r} = 0.42 \cdot \left( \frac{4 \cdot \dot{m}_{ox}}{\pi \cdot D_p^2} \right)^{0.47} \cdot 10^{-3} \quad (3.1)$$

This is a time-averaged overall fuel regression rate. Therefore, the expected fuel mass flow rate is given by:

$$\dot{m}_f = \rho_f \cdot \pi \cdot D_p \cdot L_p \cdot 0.42 \cdot \left( \frac{4 \cdot \dot{m}_{ox}}{\pi \cdot D_p^2} \right)^{0.47} \cdot 10^{-3} \quad (3.2)$$



The theoretical OF ratio is then given by:

$$OF = \frac{\dot{m}_{ox}}{\dot{m}_f} = \frac{\dot{m}_{ox}}{\rho_f \cdot \pi \cdot D_p \cdot L_p \cdot 0.42 \cdot \left( \frac{4 \cdot \dot{m}_{ox}}{\pi \cdot D_p^2} \right)^{0.47} \cdot 10^{-3}} \quad (3.3)$$

For the solid fuel  $C_{32}H_{66}$  paraffin with an assumed density  $812 \text{ kg/m}^3$ , this expression becomes:

$$OF = 0.83328 \cdot (L_p)^{-1} \cdot (D_p)^{-0.06} \cdot (\dot{m}_{ox})^{0.53} \quad (3.4)$$

This expression shows that the port diameter, which varies during the burn, has a very small - valued exponent (0.06). This feature is a consequence of the values of the characteristic exponent and coefficient used to calculate the regression rate, 0.47 and 0.42, respectively. These values were obtained by Bertoldi (2007) but correspond to a regular hybrid motor, in which the nitrous oxide is injected in the liquid phase to a pre chamber. Thus, it may not be directly applicable to the proposed system. Nevertheless, and due to the lack of more adequate experimental correlations, this equation is used to size the fuel grain based on a selected OF ratio (and in the simulation routine described in the following section), with the possibility that, regardless of the proportions of the fuel grain, the OF ratio may change little throughout the burn, as long as the oxidizer mass flow rate is fairly constant.

Considering the total mass flow rate selected before, it is possible to obtain the ideal oxidizer mass flow rate and the corresponding fuel grain length for a selected value of the OF ratio:

$$\dot{m}_{ox} = \frac{\dot{m} \cdot OF}{(1 + OF)} \quad (3.5)$$

$$\dot{m} = \dot{m}_e = \dot{m}_f + \dot{m}_{ox}$$

$$L_p = 0.83328 \cdot (OF)^{-1} \cdot (D_p)^{-0.06} \cdot (\dot{m}_{ox})^{0.53} \quad (3.6)$$

Although the stoichiometric OF ratio is 9.5, the combustion data pre-calculated in CEA 2 (CEA, 2013) shows that the maximum reaction product temperature is obtained with a slightly rich mixture (i.e. more fuel). The peak seems to be around a ratio of 8, moving down slightly for lower pressures. A value of 7.7 from Fig. 3.2 was selected as a target. In this situation, the resulted oxidizer mass flux is  $0.0885 \text{ kg/s}$ , which gives a length of  $29.9 \text{ mm}$  for the fuel grain.

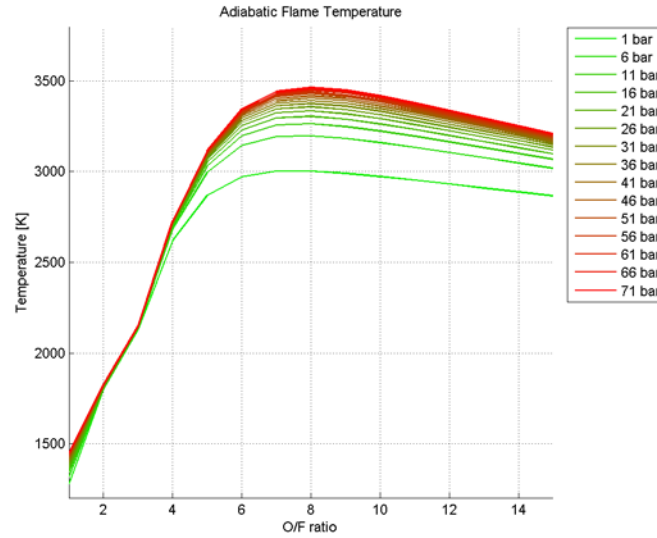


Fig. 3.2 - Combustion products temperature based on OF ratio and pressure for N2O - C32H66 combustion.

### 3.1.2.3 Injection and exhaust parameters

With the burning parameters set, the next parameter to be selected is the combustion chamber pressure. It should be noted that in an engine with this configuration, considering a single "chamber pressure" value is an approximation, since the entire operation of the engine is one continuous flow of gas which is altered by changes in the grain port diameter, mass flow rate, composition (thus molecular mass and the isentropic expansion factor changing) and stagnation enthalpy. Therefore, a more adequate analysis would be similar to a complex multi-dimensional compressible flow problem, rather than a traditional solid or liquid bi-propellant rocket engine analysis. However, to avoid the need for an elaborate mathematical treatment or a complete multi-physics numerical simulation, it is assumed that the pressure variation throughout the chamber is relatively small and an average value may be assumed.

In order to choose the target value for chamber pressure, the operating condition for having both the injection orifice and the exhaust nozzle throat choked ( $Ma = 1$ ) is considered. This is done because the maximum mass flux is achieved in these critical conditions. The choked condition can be given in terms of pressure ratio by:

$$\frac{p_u}{p_d} \geq \left( \frac{\gamma + 1}{2} \right)^{\frac{\gamma}{\gamma - 1}} \quad (3.7)$$

Applied to the present case, and considering that the mass of oxidizer in the combustion chamber at any instant is much smaller than the mass of reaction products, the condition would be rewritten as:

$$\frac{p_{ox}}{\left(\frac{\gamma_{ox} + 1}{2}\right)^{\frac{\gamma_{ox}}{\gamma_{ox} - 1}}} \geq p_c \geq p_a \cdot \left(\frac{\gamma_e + 1}{2}\right)^{\frac{\gamma_e}{\gamma_e - 1}} \quad (3.8)$$

Considering values of the ratio of specific heats of 1.6 to 2.0 for the oxidizer (which is no longer saturated at the injection, since gas acceleration causes a drop in static temperature and pressure) and 1.15 for the combustion products (from the combustion calculations), the interval for the average chamber pressure becomes approximately:

$$0.44 \cdot p_{ox} > p_c > 1.7 \cdot p_a \quad (3.9)$$

For reasons of performance, it is common to select a chamber pressure closer to the top of the interval. However, given the particular features of the proposed engine, a drop in the oxidizer tank pressure may be verified in the initial instants of the burn, until the feedback heat transfer mechanism can overcome its thermal inertia and begin to pressurize the tank. Therefore, the chamber pressure must be chosen based on a minimum threshold for oxidizer tank pressure.

Considering a lower value for tank pressure to be around 40 bar and an ambient pressure at the test site corresponding to standard conditions (1 bar = 10<sup>5</sup> Pa), the operating chamber pressure can then be allowed to vary in a range between about 2 to 17.6 bar with both injection and exhaust throats remaining choked, assuming of course that the throat area is adequately sized for the intended mass flow rate.

The injection orifice area can then be calculated from the intended mass flow rate and upstream stagnation pressure at critical conditions:

$$A_{inj} = \frac{\dot{m}_{ox}}{C_{d,inj} \cdot \sqrt{2 \cdot \rho_{ox,g} \cdot p_{ox} \cdot \left(\frac{2}{\gamma_{ox} + 1}\right)^{\frac{\gamma_{ox} + 1}{\gamma_{ox} - 1}}}} \quad (3.10)$$

$$D_{inj} = \sqrt{\frac{4 \cdot A_{inj}}{\pi}} \quad (3.11)$$

For injection in nominal conditions ( $T_{ox} = 298$  K,  $p_{ox} = 56.3$  bar – this is the oxidizer saturation pressure at  $T_{ox}$ ,  $\dot{m}_{ox} = 0.0885$  kg/s) and with a discharge coefficient of 0.6, this calculation yields an injection area of  $6.86 \times 10^{-6}$  m<sup>2</sup>, which, for a circular cross - section injection hole, is equivalent to a diameter of about 3 mm (2.96 mm to be more precise). For safety reasons, the injection should be made through small diameter orifices in order to avoid propagation of a decomposition front to the piping.

### 3.1.2.4 Chamber geometry

The combustion chamber has a tubular geometry for simplicity, with a pre-chamber and a post-chamber, respectively, before and after the fuel grain. As explained before in 3.1.2.2, the fuel grain port has a diameter that has little impact on the combustion parameters, and therefore a value can be chosen for it with few constraints.

The major constraint in the selection of the port diameter is that its value is not smaller than the injection orifice diameter in order not to cause a local choking at the port entry with potential subsequent shockwaves in the rest of the chamber. Sections further inside the grain port are not as problematic, as the ongoing combustion heats the gas and raises the speed of sound in the resulting mixture, thereby making choking more difficult. Nevertheless, a value for the port diameter of 10 mm is chosen. This is more than three times the injection orifice diameter.

After a port diameter is selected, the outer diameter can be easily calculated by considering the total amount of fuel to be burned and its density.

$$m_f = \frac{m}{(1 + OF)} \quad (3.12)$$
$$m = m_f + m_{ox}$$

$$D_c = \sqrt{\frac{4 \cdot m_f}{\pi \cdot L_p \cdot \rho_f} + D_p^2} \quad (3.13)$$

Therefore, a grain with a length of 30 mm, 10 mm of port diameter and a mass of 0.172 kg of paraffin (again modelled as solid  $C_{32}H_{66}$ ) will have an outer diameter of 100 mm.

The last geometric parameters to be determined are the lengths of the pre-chamber and post-chamber. The pre-chamber has the main function of allowing the injected gas to expand enough to cover the port surface completely and ensuring an even burn, while the post-chamber allows extra space for a more complete combustion prior to admission of the combustion products to the exhaust nozzle. Typical values for the post-chamber  $L/D$  ratio are from 0.5 to 1.0, Humble et al. (1995). Due to this, the pre and post chamber lengths were chosen as 30 mm and 50 mm, respectively.

### 3.1.2.5 Nozzle geometry

For the conical convergent-divergent nozzle design, it is necessary to know the hot combustion gas properties. With CEA 2 (CEA, 2013) this values can be retrieved, assuming that  $T_{ox} = 298$  K and  $T_f = 298$  K,  $OF = 7.7$ ,  $p_c = 10$  bar, for the paraffin ( $C_{32}H_{66}$ ) -  $N_2O$  propellant pair:  $T_c = 3257.5$  K,  $\rho_c = 0.947$  kg/m<sup>3</sup>,  $\gamma_c = 1.1420$  and  $M_c = 25.659$  kg/kmol. Considering that the throat area and diameter at critical conditions, for an isentropic flow, are:

$$A_t = A^* = \frac{\dot{m}}{C_{d, nozzle} \cdot \rho_c \cdot \sqrt{\gamma_c \cdot \left(\frac{R_A}{M_c} \cdot T_c\right) \cdot \left(\frac{2}{\gamma_c + 1}\right)^{\frac{\gamma_c + 1}{\gamma_c - 1}}} \quad (3.14)$$

$$D_t = D^* = \sqrt{\frac{4 \cdot A^*}{\pi}} \quad (3.15)$$

With  $R_A = 8314.472 \text{ J/kmol.K}$  the universal gas constant and the nozzle discharge coefficient being equal to 0.99. The critical throat area is  $0.161 \times 10^{-3} \text{ m}^2$ , which corresponds to a critical throat diameter of 14 mm.

The nozzle exit area and diameter can be calculated using the expansion ratio formula:

$$\varepsilon = \frac{A_e}{A_t} = \frac{\sqrt{\gamma_c \cdot \left(\frac{2}{\gamma_c + 1}\right)^{\frac{\gamma_c + 1}{\gamma_c - 1}}}{\sqrt{\frac{2 \cdot \gamma_c}{\gamma_c - 1} \cdot \left(\frac{p_e}{p_c}\right)^{\frac{2}{\gamma_c}} \cdot \left[1 - \left(\frac{p_e}{p_c}\right)^{\frac{\gamma_c - 1}{\gamma_c}}\right]}}} \quad (3.16)$$

$$D_e = \sqrt{\frac{4 \cdot A_e}{\pi}} \quad (3.17)$$

This results in a nozzle exit area of  $0.385 \times 10^{-3} \text{ m}^2$ , representing an expansion ratio of 2.39 and a nozzle exit diameter of 22 mm. Note that for this calculations several assumptions were made: the exhaust gases are homogeneous and have constant composition, the gas or gas mixture expelled obeys the ideal gas law, the heat capacity of the gas or mixture of gases expelled is constant, and the flow through the nozzle is one-dimensional, steady and isentropic. In other words it was assumed ideal rocket motor assumptions.

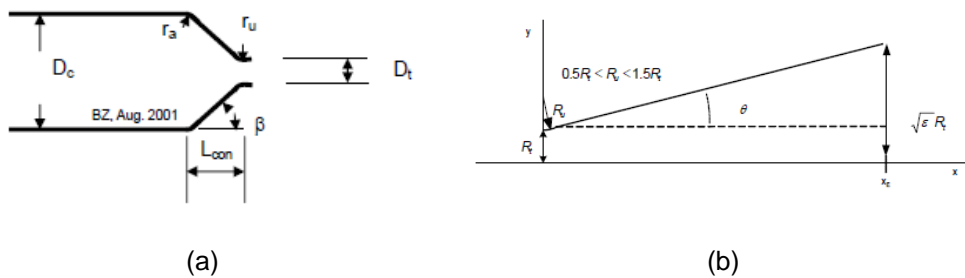


Fig. 3.3 – Conical nozzle geometry: (a) convergent section and (b) divergent section (Zandbergen, 2007).

The length of the convergent and divergent region of the nozzle can now be calculated with the following expressions:

$$L_{con} = \frac{1}{\tan \beta} \cdot (D_c - D_t) \quad (3.18)$$

$$L_{div} = \frac{(\sqrt{\varepsilon} - 1) \cdot \frac{D_t}{2} + 0.7 \cdot D_t \cdot (\sec \theta - 1)}{\tan \theta} \quad (3.19)$$

With  $\beta = 30^\circ$  and  $\theta = 15^\circ$ , the convergent side length is 70 mm, while the divergent side length is 16 mm. The total nozzle length is 86 mm.

### 3.1.3 Heat transfer system

The heat transfer system is not as easy to define as the rest of the engine. The parameters to be considered for this system are the amount of heat that is transferred and the conditions, in terms of areas, convection coefficients and temperatures involved in the process.

The minimum heat power needed to maintain the desired mass flow rate is given by:

$$q_{vap} = (h_g - h_l) \cdot \dot{m}_{ox} \quad (3.20)$$

For a nominal tank temperature around 298 K and the chosen mass flow rate, this value is of the order of 14.65 kW. In practice, the heat power necessary is larger, since there is a need to have extra gaseous oxidizer to take up the space left by the liquid oxidizer that is vaporized to inject in the combustion chamber. The simulations indicate this larger value to be around 19 kW, as can be viewed in the results chapter, see Fig. 4.7, (I). This value decreases as the tank temperature increases, since the enthalpy of vaporization drops drastically as the fluid approaches the critical point, as can be viewed in Fig. 3.4. Nevertheless, the power required to vaporize the needed oxidizer mass flow rate is about one order of magnitude lower than the power available in the exhaust gas.

Regarding the conditions at which the transfer takes place, these can be divided in three parts:

- Heat transfer by convection from the exhaust gases to the wall;
- Heat transfer from the oxidizer tank wall to the liquid oxidizer, and
- Heat transfer between the nozzle wall and the oxidizer tank wall.

The heat transfer between the exhaust gas and the nozzle wall is no different than in state-of-the-art rocket engines. The nozzle needs to be properly cooled in order to be maintained at a temperature that does not exceed the service temperature of the nozzle wall material.

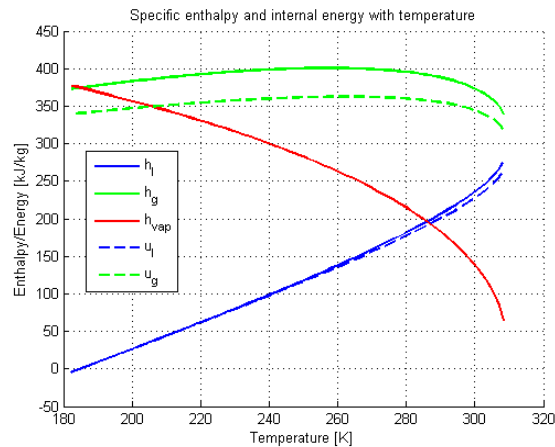


Fig. 3.4 – Enthalpy variation of liquid and gas phases for pure nitrous oxide.

Regarding the heat transfer between the tank wall and the liquid oxidizer, the process requires greater attention. Unlike other oxidizers used in rocket engines, such as oxygen, nitrous oxide is also a monopropellant by itself and therefore requires some special care when being heated. Specifically, the heat transfer must be localized and performed only to the liquid phase of the oxidizer. With this condition satisfied, two different boiling regimes are possible, depending on the difference between the temperature in the tank's wall and the oxidizer saturation temperature. For a wall temperature which does not exceed the saturation temperature of the fluid by a certain amount, the boiling occurs in the nucleate regime, with small bubbles of gas forming at the wall and afterwards detaching and rising through the fluid. If the excess temperature is greater than this critical value, the vaporization rate increases to a point where the solid surface is completely covered by a blanket of vapour (film boiling), which severely decreases the convection coefficient and the heat flux.

The typical consequence of film boiling is that the lower convection coefficient causes the wall to overheat, dangerously approaching or exceeding the service temperatures of the wall material (the choice of tank wall materials is mainly limited to stainless steel and aluminium alloys due to issues of compatibility with nitrous oxide).

For the current case, however, there is also the possibility of deflagration or detonation in the vapour blanket near the wall. Although it is widely acknowledged that decomposition waves do not propagate on uncontaminated liquid nitrous oxide, once there is a substantial amount of vapour near the wall, it is impossible to ensure that a decomposition wave started at the wall will not propagate to the gaseous phase of the oxidizer inside the tank, especially near the end of the burn, when the vapour fraction of the mixture approaches unity. Therefore, it was considered that the heat transfer mechanism should only work with nucleate boiling on the oxidizer tank wet side. The critical heat flux at which nucleate boiling starts to decline is given by:

$$q''_{\max} = \frac{q_{\text{vap}}}{S_{\text{res,min}}} = 0.131 \cdot h_{fg} \cdot \rho_g \cdot \left( \frac{\sigma \cdot a_{\text{eff}} \cdot (\rho_l - \rho_g)}{\rho_g^2} \right)^{\frac{1}{4}} \quad (3.21)$$

For a given minimum heat power that needs to be transferred at a maximum heat flux, there is a minimum tank surface area ( $S_{\text{res,min}}$ ) that needs to be heated. Considering the operating variables already set and the properties of nitrous oxide, this value is around 0.0225 m<sup>2</sup>. However, this area corresponds to a critical heat flux, which does not necessarily correspond to the desired operating point. For a safer operation, the operational heat flux may be around 70% of the maximum heat flux, which will give an area of 0.0322 m<sup>2</sup>. The corresponding heat flux is around 454 kW/m<sup>2</sup>.

This area is relatively large compared to the intended volume of the oxidizer tank. This form factor is not really suited for a pressure vessel, which means that the heat transfer to the oxidizer will have to be accomplished with a heat exchanger in which the nitrous oxide is the working fluid, or other suitable device.

The last parameter that can be estimated before a more thorough design of a specific heat transfer system is the maximum wall temperature for heat transfer to the oxidizer. This parameter can be estimated with the Rohsenow correlation:

$$q'' = \mu_l \cdot h_{fg} \cdot \sqrt{\frac{a_{\text{eff}} \cdot (\rho_l - \rho_g)}{\sigma}} \cdot \left( \frac{c_{p,l} \cdot (T_{w,ox} - T_{\text{sat}})}{C_{SF} \cdot h_{fg} \cdot \text{Pr}_l^n} \right)^3 \quad (3.22)$$

Since the oxidizer is always considered to be saturated, the saturation temperature  $T_{\text{sat}}$  is the same as the oxidizer temperature. Of all the parameters required by the correlation, the only ones that are not known are the surface-fluid combination ( $C_{SF}$ ) and the exponent of the Prandtl number ( $n$ ). These are determined experimentally for each surface-fluid pair and depend not only of the material and substance in question, but also on surface parameters. In the absence of more accurate data, values of 0.013 for  $C_{SF}$  and 1 for  $n$  were adopted from Incropera et al. (2002). The value for the effective acceleration ( $a_{\text{eff}}$ ) was considered to be equal to the gravitational acceleration, 9.81 m/s<sup>2</sup>, for the conditions of the test. This correlation can be used to estimate the maximum wall temperature for a given heat flux.

The calculations and considerations presented here show that the exact mechanism and devices for the heat transfer to the oxidizer tank will require a more careful analysis and design in future works. In fact, for a direct heat transfer from the exhaust gas to the oxidizer tank, through the nozzle walls, as mentioned, the minimum heat transfer surface is 0.0322 m<sup>2</sup>. This value is greater than the lateral surface available in the conical nozzle (0.0149 m<sup>2</sup>). So any solution for increasing the transfer surface of the nozzle should be carefully analysed in the future. Apart from that, the nitrous oxide nucleate boiling should also be more experimentally studied. This would result in a more updated nucleate boiling correlation.



Meanwhile, it may be acceptable to simplify the heat transfer model, considering that the heat used in the oxidizer tank is only a portion of the total heat transferred from the exhaust gas to the nozzle walls at a fixed temperature ( $T_w = 700$  K).

### 3.1.4 Preliminary material selection

Material selection is constrained by three types of reasons: those of material strength, those of compatibility of the candidate materials with the selected propellants, especially the oxidizer, and those of cost and availability. It is considered that for an exploratory activity such as the present, and since there are no unavoidable technical reasons that demand it, the use of exotic or expensive materials is unjustified. For reasons of compatibility, the workhorse materials chosen for the demonstrator are aluminium alloys and stainless steels.

Regarding aluminium, the choice of specific alloys to be used is pending further research and/or testing but since copper and nickel have known potential issues, a 6000 series alloy, with high concentration of silicium and magnesium and very low copper and nickel content, may be a good choice. Anodization of the surfaces in contact with the oxidizer is also an option. An aluminium alloy would be most indicated for the oxidizer tank.

For piping and fittings, as well as the combustion chamber, the material chosen will be a stainless steel alloy. Stainless steel pipes and fittings exist off the shelf in suitable sizes and can be readily adapted. The combustion chamber will be subjected to some degree of thermal stress, especially in the post chamber section. This may not be very problematic since the burn time is relatively short and the expected flow pattern near the post chamber wall should not allow very large convection coefficients.

For the nozzle, both stainless steel and a nickel-based super alloy are under consideration. The final decision will depend on cost and availability considerations, as well as the design of the test stand. It should be noted that if the feedback heat transfer were to take place through a wall separating the oxidizer and the nozzle, use of nickel-based alloys on the oxidizer tank side would not have been possible. A carbon-carbon nozzle would also be an unsuitable choice, due to its lower thermal conductivity.

### 3.2 Hybrid rocket simulation

A numerical simulation of the hybrid rocket operation is carried out. Here, the calculation algorithms supporting the simulation are described. The physical and mathematical considerations behind them are explained.

#### 3.2.1 Simulation model

Referring back to the layout presented in the previous chapter (Fig. 3.1), the five logical divisions of the dynamic model are the combustion chamber and nozzle, where the combustion and subsequent expansion of the exhaust gases take place, the oxidizer tank, from which gaseous oxidizer is injected into the combustion chamber through an injection hole and a heat transfer device which transfers part of the waste heat from the engine nozzle to the oxidizer tank in order to help vaporize more oxidizer for injection.

The algorithm devised comprises a time-marching explicit method with discrete time steps (Fig. 3.5). For each time step the relevant system variables are computed from the state and process equations or retrieved from relevant databases (NIST oxidizer saturation state tables and CEA 2 combustion results tables).

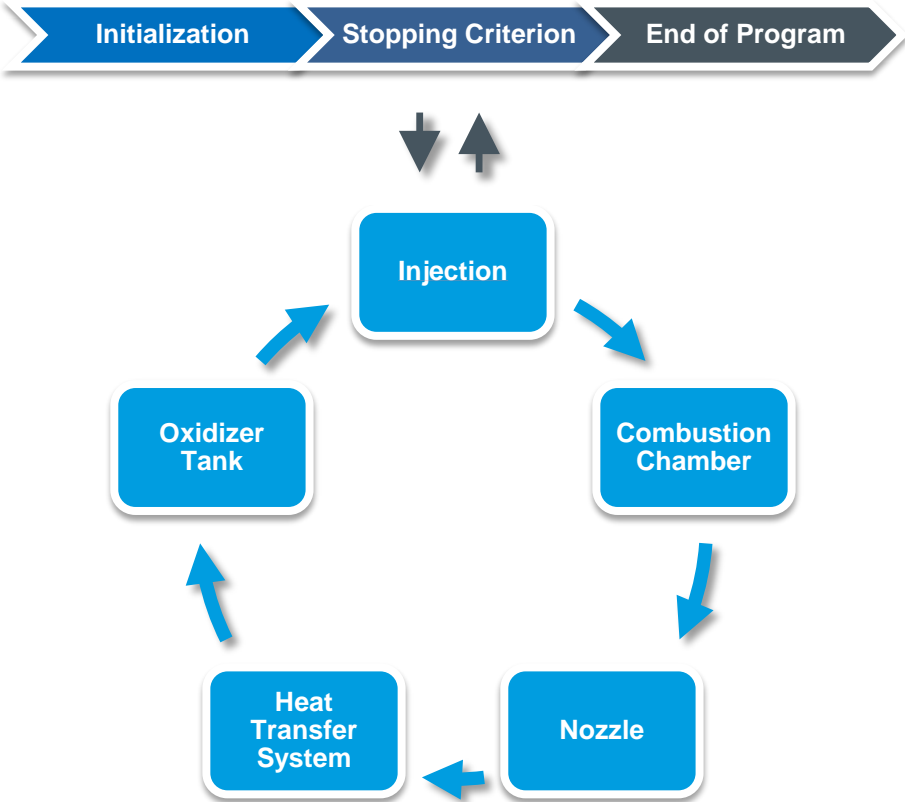


Fig. 3.5 – Simulation schematic.

Initialization of the script is simply the initial part of the program where variables and constants are declared and memory is allocated for the calculation. Likewise, the last part of the program only generates graphical representations of the quantities calculated and their evolution with simulation time.

The iterative burning calculation is the part that deserves the most attention. The time step was defined as 0.02 s, since it generated good numerical stability, while performing in a reasonable simulation time. The sequence it follows for each time step will be defined in the following subsections, as well as the equations used in the calculation and the associated assumptions and approximations.

The main stopping criterion in this simulation procedure is the complete burn condition. In other words, it means that the program will finish when the solid fuel is completely consumed. Nevertheless, there are other stopping criteria inside the simulation, like: the possibility of backflow into oxidizer tank, or the possibility of oxidizer pressure exceeding its critical pressure inside the tank.

### 3.2.1.1 Injection

The first step of each time step is to calculate the oxidizer mass flow rate that feeds the combustion chamber. This calculation is based on chamber pressure and the stagnation properties of the gas in the oxidizer tank (all of them calculated in the previous iteration/time step, or given as initial conditions). First, the pressure ratio is calculated and compared with that which would cause the injection hole to be choked. This happens if:

$$\frac{p_{ox}}{p_c} \geq \left( \frac{\gamma_{ox} + 1}{2} \right)^{\frac{\gamma_{ox}}{\gamma_{ox} - 1}} \quad (3.23)$$

There are three approximations in this calculation. The first is that upon reaching the injection hole, the gas has dropped away from the tank saturation conditions by virtue of already being accelerated when flows through the injection orifice. The second is that there is no condensation of liquid droplets in the piping. The third is that the isentropic expansion factor  $\gamma_{ox}$  is equal to the one inside the tank. The latter approximation is more reasonable for tank conditions further away from the critical point of the oxidizer. The target operating range for tank conditions (up to 298 K) is considered distant enough to make this approximation.

The mass flow rate through the injection hole is then calculated using one of two expressions, for sonic or subsonic conditions:

$$\text{Subsonic:} \quad \dot{m}_{ox} = C_{d,inj} \cdot A_{inj} \cdot \sqrt{2 \cdot \rho_{ox,g} \cdot p_{ox} \cdot \left( \frac{\gamma_{ox}}{\gamma_{ox} + 1} \right) \cdot \left[ \left( \frac{p_c}{p_{ox}} \right)^{\frac{2}{\gamma_{ox}}} - \left( \frac{p_c}{p_{ox}} \right)^{\frac{\gamma_{ox} + 1}{\gamma_{ox}}} \right]} \quad (3.24)$$

Sonic:

$$\dot{m}_{ox} = C_{d,inj} \cdot A_{inj} \cdot \sqrt{2 \cdot \rho_{ox,g} \cdot p_{ox} \cdot \left( \frac{2}{\gamma_{ox} + 1} \right)^{\frac{\gamma_{ox} + 1}{\gamma_{ox} - 1}}} \quad (3.25)$$

Note that the use of these two expressions will depend on the conditions inside the tank and the combustion chamber. For this reason the simulation is prepared both for subsonic and sonic flow at the injection.

The discharge coefficient,  $C_{d,inj}$ , is an efficiency factor dependent on the geometry of the injection hole. A worst-case scenario value of 0.6 was assumed, at the absence of an accurate calculation (which would have required a fluid dynamics simulation or experimental determination).

After the oxidizer mass flow rate is known, the fuel mass flow rate is calculated from equation (3.2), which is repeated here for convenience:

$$\dot{m}_f = \rho_f \cdot \pi \cdot D_p \cdot L_p \cdot 0.42 \cdot \left( \frac{4 \cdot \dot{m}_{ox}}{\pi \cdot D_p^2} \right)^{0.47} \cdot 10^{-3}$$

The fuel density and the length of the grain are considered constant throughout the grain. The port diameter is taken from the previous iteration and recalculated afterwards from:

$$(D_p)_{new} = D_p + 2 \cdot \dot{r} \cdot \Delta t \quad (3.26)$$

The oxidizer-to-fuel ratio is calculated as the quotient of the two mass flow rates:

$$OF = \frac{\dot{m}_{ox}}{\dot{m}_f} \quad (3.27)$$

The next step in the calculation is the temperature of the oxidizer as it enters the fuel grain port. This temperature is calculated based on isentropic compressible flow relations:

$$T_{ox,p} = \frac{T_{ox}}{1 + \frac{(\gamma_{ox} - 1)}{2} \cdot Ma_p^2} \quad (3.28)$$

$$\rho_{ox,p} = \frac{\rho_{ox}}{\left( \frac{T_{ox}}{T_{ox,p}} \right)^{\frac{1}{\gamma_{ox} - 1}}} \quad (3.29)$$

$$Ma_p = \frac{\dot{m}_{ox}}{A_p \cdot \rho_{ox,p} \cdot \sqrt{\gamma_{ox} \cdot \frac{R_A}{M_{ox}} \cdot T_{ox,p}}} \quad (3.30)$$

These three relations are solved iteratively until convergence of the oxidizer temperature is reached in each simulation time step. The process is initialized assuming a value for  $Ma_p$ . With this value, the  $T_{ox,p}$  and  $\rho_{ox,p}$  is found. With both of this values and the other values of the actual state, a new Mach number is found,  $Ma_p$ . With this new value, it gets a new  $T_{ox,p}$ . This process will continue until convergence of the old and the new  $T_{ox,p}$  is achieved. Thereby this is an implicit method. This method of calculation is valid for adiabatic and isentropic flow, like the one found in a subsonic and sonic injection. For a sonic injection, if there is a shockwave downstream of the injection orifice (in the pre - chamber), it is assumed that the shock is not strong enough to significantly alter the stagnation properties of the flow. In other words, the change of entropy is not really found. This assumption is valid since the chamber is supposed to operate at the highest possible pressure in which injection can be sonic, and thus the injection is only barely in this condition.

### 3.2.1.2 Combustion chamber

The next step is the combustion products properties calculation. These are interpolated from pre-calculated combustion tables, which are given as a function of chamber pressure, OF ratio and reactant temperatures.

The combustion calculations were handled by the CEA 2 code, developed and published by NASA Glenn Research Centre, CEA (2013), Gordon and McBride (1994) and McBride and Gordon (1996). With the help of this code some combustion data tables were produced. These tables were calculated with the fuel in solid state and at 298 K. Therefore, the vaporization of the fuel is covered in the combustion calculations. The fuel was modelled as pure dotriacontane ( $C_{32}H_{66}$ ) and its properties were retrieved from an extended reactant database made available for use with CEA 2 by Alexander Ponomarenko, RPA (2013).

The interpolation subroutine can be expressed by the following:

$$\left[ T_c, \rho_c, h_c, c_{p,c}, \gamma_c, \mu_c, Pr_c, M_c \right]_{prod} = f_{comb}(p_c, OF, T_{ox,p}) \quad (3.31)$$

Note that the left side of (3.31) represents the combustion gas values for the actual simulation time step. These values are calculated by interpolating various tables, using as inputs the actual OF,  $T_{ox,p}$  and  $p_c$ . Equations in (3.33) represents the interpolation of the various values. Note that the superscript  $a$  and  $b$  shows the interval values found on the combustion tables. Note that the combustion tables resulted from the CEA 2 combustion calculations with OF, varying from 1 to 15,  $T_{ox,p}$ , varying from 190 K to 310 K, and  $p_c$ , varying from 1 bar to 71 bar.

$$\begin{aligned}
T_c &= \frac{p_c - (p_c)^a}{(p_c)^b - (p_c)^a} \times [(T_c)^b - (T_c)^a] + (T_c)^a \\
\rho_c &= \frac{p_c - (p_c)^a}{(p_c)^b - (p_c)^a} \times [(\rho_c)^b - (\rho_c)^a] + (\rho_c)^a \\
h_c &= \frac{p_c - (p_c)^a}{(p_c)^b - (p_c)^a} \times [(h_c)^b - (h_c)^a] + (h_c)^a \\
c_{p,c} &= \frac{p_c - (p_c)^a}{(p_c)^b - (p_c)^a} \times [(c_{p,c})^b - (c_{p,c})^a] + (c_{p,c})^a \\
\gamma_c &= \frac{p_c - (p_c)^a}{(p_c)^b - (p_c)^a} \times [(\gamma_c)^b - (\gamma_c)^a] + (\gamma_c)^a \\
\mu_c &= \frac{p_c - (p_c)^a}{(p_c)^b - (p_c)^a} \times [(\mu_c)^b - (\mu_c)^a] + (\mu_c)^a \\
Pr_c &= \frac{p_c - (p_c)^a}{(p_c)^b - (p_c)^a} \times [(Pr_c)^b - (Pr_c)^a] + (Pr_c)^a \\
M_c &= \frac{p_c - (p_c)^a}{(p_c)^b - (p_c)^a} \times [(M_c)^b - (M_c)^a] + (M_c)^a
\end{aligned} \tag{3.32}$$

The combustion is considered to take place in the port of the fuel grain and the post chamber, with the composition and exhaust properties frozen at the nozzle entrance.

### 3.2.1.3 Nozzle

After the product properties are calculated, nozzle flow properties are calculated in the following subroutine:

$$\begin{aligned}
& \left[ (p_c)_{new}, p^*, T^*, p_e, T_e, a_e, U_e, Ma_x, T_x, p_x, \rho_x, A_x \right]_{nozzle} = \\
& = f_{nozzle} (R_A, p_a, T_c, \rho_c, \gamma_c, M_c, \dot{m}_e, D_c, L_{con}, L_{nozzle}, x_{nozzle})
\end{aligned} \tag{3.33}$$

Here and according to the exhaust mass flow rate calculated previously by the sum of oxidizer and fuel mass flow rates, but also with the combustion gas properties, it is determined the new combustion chamber pressure due to nozzle compressible flow. Pressure, temperature and specific mass profiles and nozzle section areas are also determined. Thereby this subroutine represents an explicit method using several implicit methods for some values calculations.

The new combustion chamber pressure is calculated by using the perfect gas law:

$$(p_c)_{new} = \rho_c \cdot \frac{R_A}{M_c} \cdot T_c \quad (3.34)$$

The exhaust mass flow rate is given by the combustion chamber mass balance as:

$$\dot{m} = \dot{m}_e = \dot{m}_{ox} + \dot{m}_f \quad (3.35)$$

Since in the nozzle, isentropic flow with area variation is assumed, the maximum exhaust mass flux is reached when the throat is at critical conditions (sonic conditions), which gives:

$$\dot{m}_{max} = (p_c)_{new} \cdot A^* \cdot \sqrt{\frac{\gamma_c}{\frac{R_A}{M_c} \cdot T_c} \cdot \left(\frac{2}{\gamma_c + 1}\right)^{\frac{\gamma_c + 1}{\gamma_c - 1}}} \quad (3.36)$$

If  $\dot{m} > \dot{m}_{max} \Rightarrow (\dot{m})_{new} = \dot{m}_{max}$ , and due to that, the new combustion chamber pressure requires to be recalculated by the following expression:

$$(p_c)_{new} = \frac{\sqrt{\frac{R_A}{M_c} \cdot T_c} \cdot (\dot{m}_{ox} + \dot{m}_f)}{\sqrt{\gamma_c \cdot \left(\frac{2}{\gamma_c + 1}\right)^{\frac{\gamma_c + 1}{\gamma_c - 1}}} \cdot A^* \quad (3.37)$$

The rest of the nozzle flow function will use the isentropic relationships for compressible flow, such as:

$$\frac{T_0}{T} = 1 + \frac{\gamma - 1}{2} \cdot Ma^2 \quad (3.38)$$

$$Ma = \frac{U}{a} \quad (3.39)$$

$$a = \sqrt{\gamma \cdot \frac{R_A}{M} \cdot T}$$

$$\frac{p_0}{p} = \left(\frac{T_0}{T}\right)^{\frac{\gamma}{\gamma - 1}} \quad (3.40)$$

$$\frac{\rho_0}{\rho} = \left(\frac{T_0}{T}\right)^{\frac{1}{\gamma - 1}} \quad (3.41)$$

$$\frac{A}{A^*} = \frac{1}{Ma} \cdot \left[ \frac{1 + \frac{1}{2} \cdot (\gamma - 1) \cdot Ma^2}{\frac{1}{2} \cdot (\gamma + 1)} \right] \quad (3.42)$$

In case there is a condition to appear a normal shock wave in the divergent side of the nozzle, the function will make use of the following expressions:

$$\frac{p_2}{p_1} = \frac{1}{\gamma + 1} \cdot [2 \cdot \gamma \cdot Ma_1^2 - (\gamma - 1)] \quad (3.43)$$

$$Ma_2^2 = \frac{(\gamma - 1) \cdot Ma_1^2 + 2}{2 \cdot \gamma \cdot Ma_1^2 - (\gamma - 1)} \quad (3.44)$$

$$\frac{\rho_2}{\rho_1} = \frac{(\gamma + 1) \cdot Ma_1^2}{(\gamma - 1) \cdot Ma_1^2 + 2} = \frac{V_1}{V_2} \quad (3.45)$$

$$\frac{T_2}{T_1} = [2 + (\gamma - 1) \cdot Ma_1^2] \cdot \frac{2 \cdot \gamma \cdot Ma_1^2 - (\gamma - 1)}{(\gamma + 1)^2 \cdot Ma_1^2} \quad (3.46)$$

$$T_{02} = T_{01} \quad (3.47)$$

$$\frac{p_{02}}{p_{01}} = \frac{\rho_{02}}{\rho_{01}} = \left[ \frac{(\gamma + 1) \cdot Ma_1^2}{2 + (\gamma - 1) \cdot Ma_1^2} \right]^{\frac{\gamma}{\gamma - 1}} \cdot \left[ \frac{\gamma + 1}{2 \cdot \gamma \cdot Ma_1^2 - (\gamma - 1)} \right]^{\frac{1}{\gamma - 1}} \quad (3.48)$$

$$\frac{A_2^*}{A_1^*} = \frac{Ma_2}{Ma_1} \cdot \left[ \frac{2 + (\gamma - 1) \cdot Ma_1^2}{2 + (\gamma - 1) \cdot Ma_2^2} \right]^{\frac{1(\gamma + 1)}{2(\gamma - 1)}} \quad (3.49)$$

Two remarks should be made here. The first says that these normal shock wave calculations will require an iterative procedure to determine the normal shock wave position. Thereby it is used an implicit method. The second is that an assumption of adiabatic flow is done in these relationships. Considering adiabatic flow is seemingly conflicting with the heat transfer in the nozzle, but since the amount of heat transferred can be made relatively small compared to the energy in the exhaust flow, this was accepted.

The results from the nozzle flow routine will affect the rocket performance. The exhaust velocity, which for non-adapted nozzles will be substituted by an equivalent velocity, is given by:

$$U_{eq} = U_e + \frac{p_e - p_a}{\dot{m}} \cdot A_e \quad (3.50)$$



The Tsiolkowsky's equation, i.e., the rocket thrust equation, for conical nozzles, follows:

$$F = \frac{1 + \cos \theta}{2} \cdot \dot{m} \cdot U_e + (p_e - p_a) \cdot A_e \quad (3.51)$$

The specific impulse is another performance parameter that measures how much impulse is produced per propellant weight that the rocket spends. It is given by the following equation:

$$I_{sp} = \frac{U_{eq}}{g_0} \quad (3.52)$$

### 3.2.1.4 Heat transfer system

The next step is to calculate the heat transfer away from the nozzle: for this, it is assumed that the heat is transferred by convection, on the entire nozzle, and that the heat transfer system keeps the wall at a constant temperature ( $T_w = 700$  K) which is below the maximum service temperature of the material. In order to calculate the heat transferred, and to account for the variation of both the geometry and the gas properties through the nozzle, the latter is divided into discrete sections and the heat transfer is then calculated at each section and integrated to yield a global result. The film temperature at section  $x$  of the nozzle is:

$$T_{x, film} = \frac{T_x + T_w}{2} \quad (3.53)$$

The convective heat coefficient of the hot gases inside the nozzle can be retrieved by the Cornelisse et al. correlation presented in Zandbergen (2007):

$$\bar{h}_{x,c} = 0.023 \cdot \text{Pr}_c^{0.33} \cdot k_c \cdot \left( \frac{\dot{m}_e}{A_x \cdot \mu_c} \right)^{0.8} \cdot \left( \frac{1}{D_x} \right)^{0.2} \cdot \left( \frac{T_c}{T_{x, film}} \right)^{0.68} \quad (3.54)$$

The heat transferred is given by:

$$q_x = A_{x, lat} \cdot \bar{h}_{x,c} \cdot (T_x - T_w) \quad (3.55)$$

After all the discrete sections are calculated, the total heat power is obtained by adding up all the contributions from the individual sections. An efficiency factor is also applied. This factor represents the fraction of the heat transferred from the nozzle that reaches the oxidizer tank. The rest of the energy is considered to be dissipated by the feedback heat transfer system.

$$q_{ox, nozzle} = \eta_{ox, nozzle} \cdot \sum_x q_x \quad (3.56)$$

It should be noted that the one-dimensional approximation used to calculate the flow in the nozzle may not be very accurate for very short nozzles as will be the case. A two-dimensional calculation of the flow pattern and the heat transfer would be necessary for a more accurate calculation, but such a change would require a different approach, and would involve a far greater effort. This is yet another reason why the heat transfer system should be considered with extra care.

### 3.2.1.5 Oxidizer tank

In this section it was developed a complete engineering model for the  $N_2O$  tank with heat transfer through the tank walls. This model simulates the thermodynamics of liquefied gas evaporation out of the storage reservoir, as can be showed in Fig. 3.6.

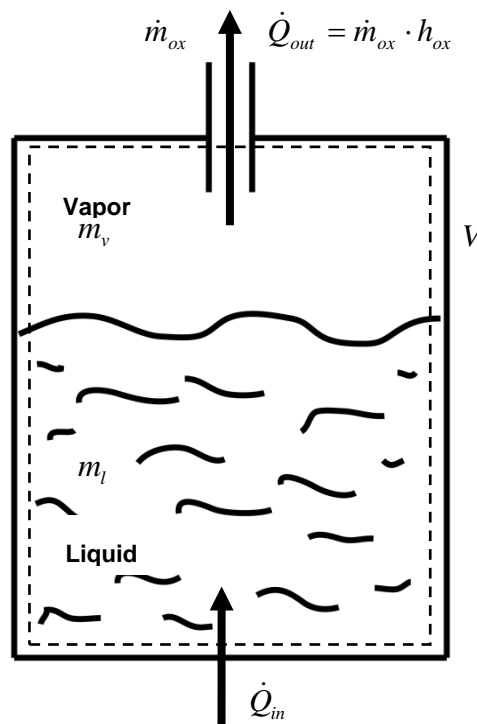


Fig. 3.6 – Schematic of the stratified tank model showing the orifice through the vapor propellant escapes.

A control volume is assigned to the fluid inside the tank, as can be seen by the dash line in Fig. 3.6. At the beginning, there is no gas flow out of the tank, so the thermodynamic system is a closed one. The saturated fluid inside the reservoir is assumed to remain at equilibrium for a defined temperature. Depending on its initial conditions the equilibrium can be of single phase: vapor or liquid; or a two - phase one: liquid - vapor.

Heat transfer through tank walls is also contemplated in this model. Here, the walls can be adiabatic, with no heat transfer to and from the surroundings, given heat or heat specified via a heat transfer coefficient and the temperature of the surrounding fluid.

When the tank is open, thermodynamically the system becomes an open one. A saturated vapor leaves the tank through a circular and a constant cross-section area throat expelled by pressure difference, between vapor pressure and exterior pressure. Depending on the heat rate entering the system through the tank walls and the heat and mass inside the system, evaporation proceeds till a new equilibrium state is reached inside.

The following assumptions are used for developing this model:

- 1) The tank forms an open/closed system.
- 2) 1 – Dimensional analysis, homogeneous.
- 3) The tank is small enough, so that the pressure equalizes instantly within the entire internal tank volume during evacuation.
- 4) The fluid in the tank is stratified with distinct liquid and vapor layers.
- 5) The fluid in the tank is in equilibrium, in two - phase (liquid-vapor) and in single - phase (vapor or liquid).
- 6) The fluid hydrostatic pressure is negligible when compared with the saturation vapor pressure.
- 7) The fluid exiting the tank is in vapor phase.
- 8) Properties of the saturated fluid retrieved from the multi-parameter NIST formulation, in form of tables, i.e., real gas and compressible liquid effects in consideration.
- 9) Regular geometry shape of storage tank (cylinder, sphere, and cylinder with spherical ends), and tank volume remains constant.
- 10) Heat transfer through the tank walls.
- 11) No chemical reactions inside the tank.
- 12) No mechanical work.
- 13) No potential energy change.

The engineering model presented here is based on the conservation of mass and energy inside the control volume. The mass balance for the open system can be written as:

$$\begin{aligned} \frac{dm}{dt} &= -\dot{m}_{ox} \\ \Rightarrow (m_{ox})_{new} &= m_{ox} - \dot{m}_{ox} \cdot \Delta t \end{aligned} \quad (3.57)$$

The energy balance for this system gives the following expression:

$$\begin{aligned} \frac{dE}{dt} &= \dot{Q}_{in} - \dot{m}_{ox} \cdot h_{ox} \\ \Rightarrow (u_{ox})_{new} &= \frac{\dot{Q}_{in} \cdot \Delta t - \dot{m}_{ox} \cdot h_{ox} \cdot \Delta t - (m_{ox})_{old} \cdot (u_{ox})_{old}}{(m_{ox})_{new}} \end{aligned} \quad (3.58)$$

In (3.57) and (3.58), the subscript *old* is the discrete time index, and the time interval between indices is  $\Delta t$ . From the mass balance, (3.57), it can be retrieved the propellant mass inside the tank for the next time index (*new*), while in the energy balance, (3.58), the specific internal energy for *new* can be calculated. Note that these values are calculated by numerical integration of the mass and energy balance.

Where, in the above equations:

$$\begin{aligned} (m_{ox})_{old} &= (m_{ox,l})_{old} + (m_{ox,g})_{old} \\ (m_{ox})_{new} &= (m_{ox,l})_{new} + (m_{ox,g})_{new} \end{aligned} \quad (3.59)$$

And:

$$\begin{aligned} (u_{ox})_{old} &= (u_{ox,l})_{old} + (\chi_{ox})_{old} \cdot [(u_{ox,g})_{old} - (u_{ox,l})_{old}] \\ (u_{ox})_{new} &= (u_{ox,l})_{new} + (\chi_{ox})_{new} \cdot [(u_{ox,g})_{new} - (u_{ox,l})_{new}] \end{aligned} \quad (3.60)$$

With  $\chi$  being the fluid quality, which is the ratio of the mass of the vapor divided by the total fluid mass.

The vapor mass flow exiting the tank was already calculated in the injection subroutine. Since the tank volume remains constant, the updated effective density can be retrieved from the following equation:

$$(\rho_{ox})_{new} = \frac{(m_{ox})_{new}}{V} \quad (3.61)$$

The updated density and specific internal energy values are now used to calculate the new temperature, pressure, and fluid quality in the tank, using a table lookup on the data in the NIST property tables described next. The fluid's density and specific internal energy are dependent of the fluid's quality but also of its saturated point, as can be seen in the following equations:

$$\begin{aligned} \rho &= \frac{m}{V} = \frac{m_l + m_g}{V_l + V_g} = \frac{\rho_l \cdot \rho_g}{\rho_l \cdot \chi + (1 - \chi) \cdot \rho_g} \\ u &= u_l \cdot (1 - \chi) + u_g \cdot \chi \end{aligned} \quad (3.62)$$

Taking (3.62) into consideration and the data from NIST tables, the saturated fluid database is parsed using an interpolation routine. The remaining liquid and vapor masses in the tank are calculated as follow:

$$\begin{aligned} (m_{ox,g})_{new} &= \chi \cdot (m_{ox})_{new} \\ (m_{ox,l})_{new} &= (1 - \chi) \cdot (m_{ox})_{new} \end{aligned} \quad (3.63)$$

The heat transfer is specified via a heat transfer coefficient and the temperature of the surrounding fluid, and varies with time, because the conditions inside the tank changes:

$$\dot{Q}_{in} = q_{ox, nozzle} \quad (3.64)$$

Equations (3.57) to (3.64), along with saturation properties, form the core of the engineering model that describes this system. These equations are numerically integrated over time (and the database is parsed) to continuously calculate the tank-fluid state properties as a function of time. This model intrinsically takes into account the masses of liquid and vapor that change phase due to boiling and condensations.

The computational algorithm is based on the above model and can be summarized in the following steps:

1. Calculate  $(m_{ox})_{new}$  from (3.57).
2. Calculate  $(\rho_{ox})_{new}$  from (3.61).
3. Considering  $\dot{Q}_{in}$  from the heat transfer system subroutine, calculate  $(u_{ox})_{new}$  from (3.58).
4. Interpolation routine where the inputs are  $(u_{ox})_{new}$  and  $(\rho_{ox})_{new}$ , and the outputs are  $(T_{ox})_{new}$  and  $(\chi_{ox})_{new}$ .
5. Calculate the upgraded properties with  $(T_{ox})_{new}$ .
6. Save parameter values for this time step, and actualize the parameters, i.e., the upgraded values become the older ones:

$$\left[ T, p, \chi, \rho_l, h_l, u_l, s_l, c_{p,l}, c_{v,l}, \sigma_l, \rho_g, h_g, u_g, s_g, c_{p,g}, c_{v,g}, \gamma_g \right]_{ox} = f_{sat}(\rho_{ox}, h_{ox}) \quad (3.65)$$

The calculation of the mixture properties in the oxidizer tank closes the iteration. Success termination conditions are then checked and if neither is met, the iteration continues. Failure conditions, on the other hand, are checked throughout the iteration instead of only at the end.

### 3.3 Tank validation model

In order to validate the theoretical and numerical oxidizer tank model, which is an important part of the simulation scheme, as can be seen in Fig. 3.5, experimental work is necessary. In fact, the studies related to this subject found in the literature were based only on experimental analysis without heat transfer through the tank walls. Whitmore et al (2010) and Zakirov et al (2005) are good examples of this.

Three types of experiments were performed at the Chemistry Department of the School of Science and Technology (FCT) in Universidade Nova de Lisboa (UNL), with the collaboration of its Processes with Supercritical Fluids group. The first one, tests the two-phase liquid-vapour CO<sub>2</sub> conditions inside a small reactor without adiabatic walls. A saturated carbon dioxide vapour is slowly withdrawn through a pressure-regulating valve at the top of tank. The use of CO<sub>2</sub> in this stage of the research allows for testing the method with a safer gas and increase the understanding of the process before repeating the experiment with the more dangerous and expensive N<sub>2</sub>O.

In the second experiment, the difference from the previous one is that the walls are isolated from the exterior. In the third experiment, a thermal resistance inside the reactor is used to simulate a heat source directly applied to the CO<sub>2</sub> liquid phase inside the reactor, while a saturated carbon dioxide vapour is slowly withdrawn through a pressure-regulating valve at the top of tank. The objective is to test an experimental method to obtain a model for a N<sub>2</sub>O tank thermodynamic behaviour in the same conditions.

In the following section, it will be presented the material characteristics, the equipment and methodology used in the tests and interpretation of the experimental data.

### 3.3.1 Material characterization

The carbon dioxide (CO<sub>2</sub>) was chosen as the test fluid for its ease of acquiring and handling. Due to its lower toxicity, carbon dioxide (CO<sub>2</sub>) is rather safer than nitrous oxide (N<sub>2</sub>O). Moreover, the similarity of both compounds in the saturated regime and critical point are also extremely important for the choice made.

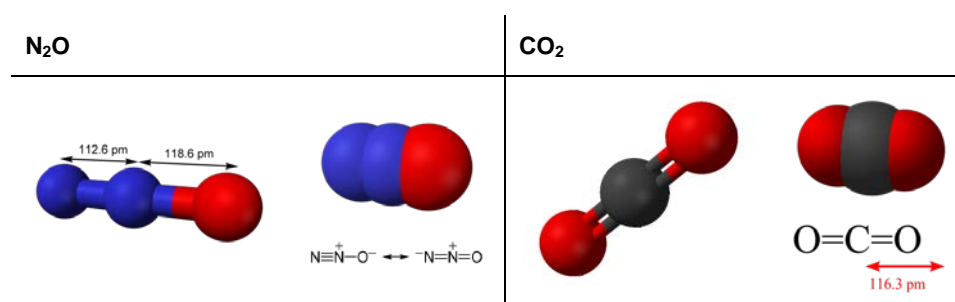


Fig. 3.7 – Molecular geometry of nitrous oxide and carbon dioxide.

From Fig. 3.7, it can be viewed that the nitrous oxide is a slightly polar molecule, while the carbon dioxide is symmetrical. As can be read in Karabeyoglu et al (2008), this polarization is the reason why N<sub>2</sub>O is a highly effective solvent for hydrocarbons, introducing many material compatibility problems. This means more safety concerns, which with a practically inert substance like CO<sub>2</sub>, does not required.

The physical properties of  $N_2O$  and  $CO_2$  are very similar both in the saturation regime and at critical point. Tab. 3.1 compares the critical and triple point of both molecules. The similitude of the critical properties, such as temperature, pressure and density, allows for considering that the phenomena simulated will not change enough to render the test useless for  $N_2O$ .

Fig. 3.8 (a) shows the variation of saturated pressure with temperature for both molecules. At low temperatures the saturated pressure is almost the same, while in high temperatures, near critical point, a considerable difference (of the order of almost 1 MPa) exists. Nevertheless, what is important is the saturation behaviour of the carbon dioxide, which is very similar to the nitrous oxide.

The variation of density with temperature in saturated regime is represented in Fig. 3.8 (b) for both substances. The solid lines represent the saturated liquid state, while the dash line corresponds to the saturated vapour state.

Properties	$N_2O$	$CO_2$
<b>Critical Temperature (<math>T_{cr}</math>) [K]</b>	309.52	304.13
<b>Critical Pressure (<math>p_{cr}</math>) [MPa]</b>	7.245	7.377
<b>Critical Density (<math>\rho_{cr}</math>) [kg/m<sup>3</sup>]</b>	452.0	467.6
<b>Triple Point Temperature (<math>T_{tp}</math>) [K]</b>	182.33	216.59
<b>Triple Point Pressure (<math>p_{tp}</math>) [MPa]</b>	0.0878	0.5180

Tab. 3.1 –  $N_2O$  and  $CO_2$  critical properties.

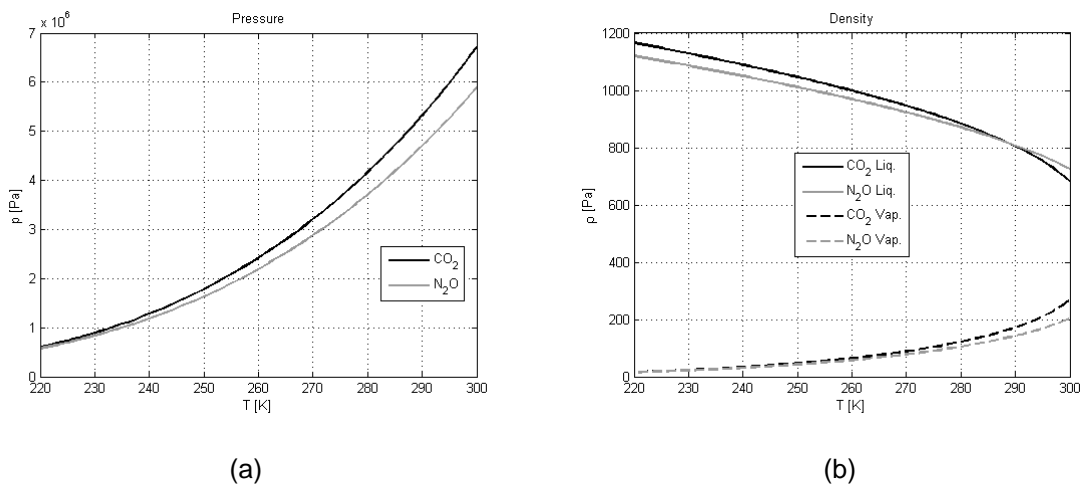


Fig. 3.8 –  $CO_2$  and  $N_2O$ : (a) saturated pressure and (b) saturated liquid and vapour density.

The property where the molecules show more differences is the specific internal energy (Fig. 3.9). This is due to the inert and polar characteristics that  $CO_2$  and  $N_2O$  respectively presents.

Nevertheless, the similarity of both the curves is noticeable. Again the solid line represents the saturated liquid state, while the dashed line presents the saturated vapour state.

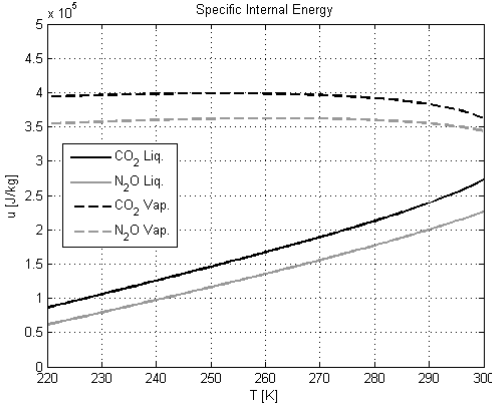


Fig. 3.9 - CO<sub>2</sub> and N<sub>2</sub>O saturated liquid and vapour specific internal energy.

### 3.3.2 Simulation model

The oxidizer tank simulation procedure is an important part of the global simulation scheme, as mentioned in Fig. 3.5. The simulation procedure is the same as described in section 3.2.1.5. Nevertheless, because the experimental work consists of three different tests, small changes will be made in each test. All these changes will be made in the heat transfer calculation. While in the first experiment, the heat transfer  $\dot{Q}_{in}$  of (3.64) is given as a convective form, in the second experiment, this value is equal to zero due to the adiabatic assumption. In the third experiment, the  $\dot{Q}_{in}$  value is equal to the power of the thermal resistance.

### 3.3.3 Experimental setup

The experimental setup consists of the following equipment:

- High pressure reactor
- Feeding lines and fittings
- Valves
- Manometers
- Thermoresistance
- Cartridge heater
- Flow meter
- CO<sub>2</sub> tank
- Pump
- Calibration tank
- Thermal insulation
- Digital displays
- Multimeter
- Electrical Dimmer
- Hairdryer
- Hood



A photo and a schematic of the experimental apparatus are shown in Fig. 3.10 and Fig. 3.11, respectively. As shown in Fig. 3.11, the carbon dioxide inside the vessel (1) is introduced to a calibrated volume screw-injector (6) using compressor (3) to a certain desired pressure through valve (4). The pressure is measured by pressure gauge (5). Valve (2) is installed for safety features.

The calibrated screw-injector is connected to the high-pressure reactor/tank (9) through valve (8), permitting introduction of CO<sub>2</sub> into the reactor. The line is equipped with a safety released valve (7), allowing quick depressurization. Previously determined volume of the screw-injector, known conditions of pressure and temperature are used to calculate the mass of CO<sub>2</sub>. Note that the screw-injector is involved with icepacks (22), so that the CO<sub>2</sub> can be at 0 °C.

Beside the CO<sub>2</sub> entrance, there is a second entry of the reactor for the installation of the cartridge heater (10) which is equipped with a thermocouple of type J. This allows measuring the heater surface temperature which can be monitored with a digital display (11). The heat power is regulated using a dimmer (12). A multimeter (Kaise MY64) (13) is installed to measure the voltage at dimmer's terminals.

The third and last port of the reactor is for the exhaust line. Upstream this line is found a union cross, dividing the line in three paths. In one branch a thermo resistance (model Pt 100 from Omega) (15) is installed and measures the CO<sub>2</sub> temperature inside the reactor, which is displayed in (16). On the other one, an analogue pressure transducer (HPO model from Heise) (17) is installed, which measures the pressure inside the reactor and can be monitored with a digital display (18). In the third branch, the CO<sub>2</sub> is released to the environment (to the hood) by opening two sets of valves, (19) and (20), which controls the exhaust flow. In order to avoid freezing during depressurization, a hairdryer (23) is used. The exhaust flow is measured downstream by a flow meter (DM3C model from Alexander Wright a division of the Zeal Group) (21).

High-pressure stainless steel tubes of various diameters, as well as fittings, T - junctions and cross - junctions are used in this installation to connect the various pieces of equipment together.

The measurements of the amount of CO<sub>2</sub> that enters and exits the reactor are very important in this set of experiments. For that reason it will be described in more detailed in the following lines.

By filling totally the volume of a calibration tank at a certain temperature and pressure, the amount of carbon dioxide can be found. At high pressure (200 bar = 20 MPa) and low temperature (0 °C), carbon dioxide is in liquid phase and its density is known. A screw mechanism that operates outside, by rotating a wheel, moves a piston inside the calibration tank, which reduces the internal volume. Calculating the number of turns needed for the piston to cover the total volume and dividing the total volume by this number, gives a volume per complete wheel turn. In these experiments, this volume is 0.2546 mL. Consequently a mass per complete wheel turn can be derived by multiplying this volume with the density known.



Fig. 3.10 – Photo of the experimental setup at FCT/UNL laboratory.

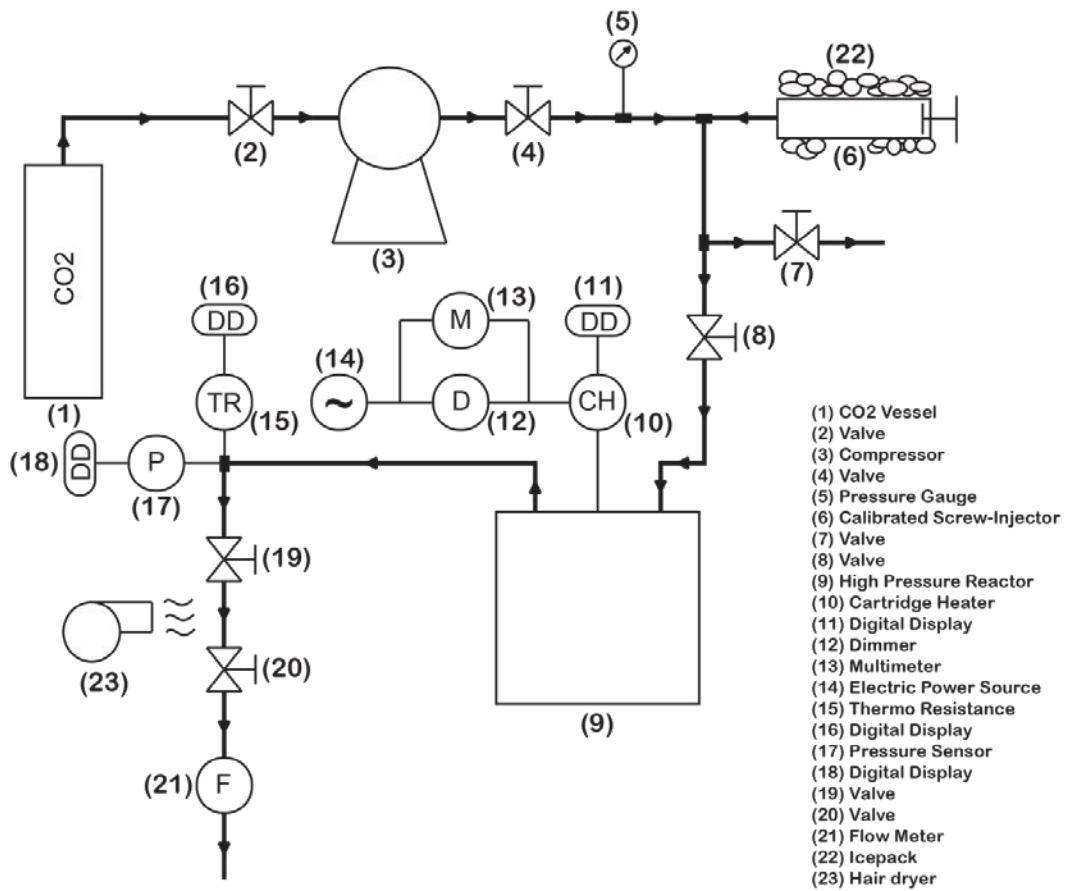


Fig. 3.11 – Experimental schematic.

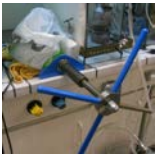


When the reactor inlet valve is opened, CO<sub>2</sub> will enter the tank. After closing this valve, the amount of CO<sub>2</sub> entered inside the reactor can be known by accounting the number of complete wheel turns needed to reach the same initial inline pressure. If this number is multiplied by the volume and the mass per complete wheel turn, the total carbon dioxide volume and mass that enters the high pressure reactor can be known, respectively.






To calculate the amount of carbon dioxide that exits the reactor, an initial and final volume is measured by the flow meter. With these values the total CO<sub>2</sub> volume is determined. By applying the ideal gas law to this data, the total carbon dioxide mass is found, and knowing the time interval between the two volume measurements, the mass flow can be easily calculated. Moreover, taking into consideration the carbon dioxide properties and the geometrical characteristics the liquid height inside the pressure reactor can be found by the following expression:

$$H_l = \frac{m_{CO_2} - (V_{reactor} \cdot \rho_g)}{(\rho_l - \rho_g) \cdot A_{reactor,base}} \quad (3.66)$$

With  $m_{CO_2}$  the carbon dioxide mass inside the reactor,  $V_{reactor}$  is the reactor volume,  $A_{reactor,base}$  is bottom surface area of the reactor and  $\rho_g$  and  $\rho_l$  are respectively the vapour and liquid densities at the saturated temperature and pressure inside the tank.

A review of the principal characteristics of the major experimental equipment is mentioned in Tab. 3.2.

Equipments	Characteristics	Figures
<b>Calibration tank</b>	<ul style="list-style-type: none"> <li>• A calibration tank is used to know the quantity of CO<sub>2</sub> that enters inside the high pressure reactor.</li> <li>• Volume: 30 mL.</li> <li>• Use of icepacks to ensure a low temperature inside the calibration tank.</li> </ul>	
<b>High pressure reactor</b>	<ul style="list-style-type: none"> <li>• Is a two piece stainless steel cylinder with an internal diameter of 44 mm, an internal height of 96 mm and a wall thickness of 6 mm, which represents 146 mL of internal volume.</li> <li>• The top has 3 ports, two of them are 1/16" NPT size, which are used for the inline and the exhaust lines, and the third one is a 1/4" BSP size, for fastening the cartridge heater.</li> <li>• A NBR o-ring is installed on the reactor cover to avoid any leaks that might occur due to interior high pressure environment.</li> <li>• Insulation foam is used to cover the entire reactor in the adiabatic walls experiences.</li> </ul>	 

Equipments	Characteristics	Figures
<b>Thermoresistance</b>	<ul style="list-style-type: none"> <li>• Is an instrument that allows to know the environment temperature, using the relationship between the electrical resistance of a material and its temperature.</li> <li>• The model used in the experiments is a Pt-100 from Omega.</li> <li>• Material: platinum, it shows at 0 °C a resistance of 100 Ω.</li> <li>• Dimensions: 3 mm diameter and 110 mm length.</li> <li>• Accuracy: ± 0.2 °C.</li> </ul>	
<b>Pressure Transducer/ Manometer</b>	<ul style="list-style-type: none"> <li>• Measures reactor pressure.</li> <li>• Accuracy: ± 0.7 bar.</li> <li>• Model: Heise HPO pressure transducer.</li> </ul>	
<b>Cartridge Heater</b>	<ul style="list-style-type: none"> <li>• The cartridge heater is essentially a highly compacted electrical resistance, with a 50 W/cm<sup>2</sup>.</li> <li>• Add-ons include: a J-type thermocouple to measure the cartridge heater surface temperature, a stainless steel tube extension and a BSP threaded fitting so that could be installed in the high pressure reactor.</li> <li>• Dimensions: 122 mm total length, which 50 mm length is for the heating zone, and 8 mm diameter.</li> <li>• The heating source maximum power is 160 W at 240 V.</li> <li>• Accuracy of type J thermocouple: ± 0.2 °C.</li> <li>• The heating power control is done by a modified dimmer and a multimeter.</li> <li>• Accuracy of measured voltage: ± 0.5 V.</li> <li>• Knowing the electric resistance installed in the cartridge heater is 360 Ω, the heating power comes from the Joule's law (<math>P = V^2/R</math>).</li> </ul>	 
<b>Flow meter</b>	<ul style="list-style-type: none"> <li>• Is a positive displacement type flow meter.</li> <li>• Model: DM3C from Alexander Wright a division of the Zeal group.</li> <li>• Accuracy: ± 0.00005 m<sup>3</sup>.</li> </ul>	

Tab. 3.2 - Principal characteristics and pictures of the major experimental equipment

### 3.3.4 Experimental procedure

As mentioned before, in the present work three different experiments were conducted. The procedure for each one will be described in the following.

#### 3.3.4.1 Experiment 1: Withdrawing CO<sub>2</sub> vapour from a tank without adiabatic walls

The following describes the steps of the experiment 1.

1. Setup leaks verification, covering the calibrated screw-injector with icepacks and open the compressed air valve that feeds the compressor.
2. Take note of the ambient conditions, like temperature and pressure.
3. With the safety valve and the inlet reactor valve closed, and the control valve upstream the compressor opened, open the CO<sub>2</sub> tank valve.

4. Through compressor regularization, pressurize the CO<sub>2</sub> in the inlet line to 200 bar.
5. Close the control valve and switch off the compressor.
6. Filling the high pressure reactor with CO<sub>2</sub> by opening the inlet valve, and close it when the line pressure levels with the reactor's one.
7. Count the number of wheel turns in the calibrated screw-injector until the line pressure reaches the initial 200 bar. Note that if the total screw-injector volume is covered by wheel turns and the line pressure does not trend to its initial value, then it is necessary to refilling its total volume and steps 3 to 6 are repeated until step 7 is verified.
8. Knowing the total wheel turns and the CO<sub>2</sub> density, at 200 bar and 0 °C, it is determined the total mass of carbon dioxide injected into the high pressure reactor.
9. After waiting some minutes for stabilization of the reactor's interior saturated conditions, take note of its temperature and pressure.
10. With these values, the density and other properties at this saturated condition are known by consulting NIST tables. Moreover, knowing the amount of CO<sub>2</sub> inside the reactor and its dimensions, the initial quality of the liquid-vapour mixture inside the reactor is calculated.
11. Take note of the initial volume measurement by the flow meter. Turn on the hairdryer and point it to the exhaust valves.
12. With the cartridge heater switched off, start recording with a camcorder and clocking with a stopwatch while the exhaust valves are opened.
13. First open one valve, and then the exhaust flow is controlled by a second one until a certain wanted flow is achieved.
14. While the experiment is being taken take notes of the volumes monitored in the flow meter. If necessary readjust the exhaust flow so that it is maintained approximately constant.
15. The experiment stops when the interior pressure reaches the ambient value and the flow meter stops.

#### **3.3.4.2 Experiment 2: Withdrawing CO<sub>2</sub> vapour from a tank with adiabatic walls**

The procedure of this second experiment is the same as the one described in experiment 1, with the difference that here the reactor is covered by insulation material.

#### **3.3.4.3 Experiment 3: Withdrawing CO<sub>2</sub> vapour from a tank at a constant pressure with adiabatic walls and heat source**

This third experiment procedure differs from the second one in the fact that the cartridge heater is switched on and regulated to a certain voltage, depending on the initial carbon dioxide quantity inside the high pressure reactor. Moreover, the experiment time is reduced since only a certain defined amount of CO<sub>2</sub> is exhausted from the reactor. For this reason, step 10, 12, 13 and 14 requires some adding tasks.

In step 10, it is necessary to calculate the amount of heat power in form of voltage to impose in the cartridge heater through the dimmer. This value is calculated knowing the amount of heat necessary to vaporize a certain liquid height inside the reactor, while maintaining its interior conditions.

The cartridge heater can be switched on in step 12, before opening exhaust valves, or in step 13, after opening the exhaust valves. It will be a study parameter in this experiment. Note that the camcorder records the data shown in all digital displays, including the multimeter.

During the experiment, the voltage of the cartridge heat must need to be regulated through the dimmer, so that the interior conditions remain the same. This procedure is added to the previous step 14.

## 4 Results and Discussion

### 4.1 Hybrid rocket preliminary design

The proposed HRPE demonstrator preliminary design and some thermodynamic results can be summarized in next table:

Project Values								
Design Operational Point			Combustion Chamber Geometry			Nozzle Geometry		
$p_c$	$\times 10^5$ [Pa]	10	$L_p$	$\times 10^{-3}$ [m]	29.9	$A^*$	$\times 10^{-3}$ [m <sup>2</sup> ]	0.161
$p_a$	$\times 10^5$ [Pa]	1	$D_c$	$\times 10^{-3}$ [m]	95.5	$D^*$	$\times 10^{-3}$ [m]	14.2
$T_{ox}$	[K]	298	$L_{pre}$	$\times 10^{-3}$ [m]	30.0	$\epsilon$		2.39
$T_f$	[K]	298	$L_{pos}$	$\times 10^{-3}$ [m]	50.0	$A_e$	$\times 10^{-3}$ [m <sup>2</sup> ]	0.385
$OF$		7.7				$D_e$	$\times 10^{-3}$ [m]	22.1
$\dot{m}$	[kg/s]	0.1				$L_{con}$	$\times 10^{-3}$ [m]	70.3
						$L_{div}$	$\times 10^{-3}$ [m]	15.9

Tab. 4.1 – Hybrid rocket design results.

These values will be the input project parameters in the following hybrid rocket simulation study.

### 4.2 Tank validation model

In this section, the experimental results and discussion will be presented. The total number of experiments was three, which each of them required several tests. Taking this into consideration, the total number of tests were 13. Six of them were related to the first experiment, while other two were connected to the second experiment. The last five trials were dedicated to the third experiment. Nevertheless, due to several problems found in the tests, some of these were not able to be taken into account. The difficulty in regularizing the exhaust valve for a certain mass flow value, the unused hairdryer to avoid valve freezing due to expansion of CO<sub>2</sub> gas at the exhaust, the difficulty of establish a certain voltage/power for the cartridge heater, all these represents some of the problems mentioned earlier. So all in all, for the first experiment, four in six tests were considered, while two out of two and three out of five tests were considered, for the second and the third experiments, respectively.

### 4.2.1 Experiment 1

In the first experimental studies, the CO<sub>2</sub> vapour is withdrawing from a tank without adiabatic walls. As mentioned, only 4 tests were validated, which initial and final conditions are described in Tab. 4.2.

In this table, for all trials, it is noticed that only vapour carbon dioxide remains inside the reactor at the end of the experiment ( $\chi_f = 1$ ). This is confirmed by the final pressure and temperature values ( $p_f$  and  $T_f$ ), which are representative of the CO<sub>2</sub> vapour state. Further, it means that the saturation conditions no longer are present inside the reactor after a certain moment.

Taking into consideration the plots of Fig. 4.1, it can be noticed that this passage of saturated to vapour state conditions happens particularly in the end of the tests. Here the experimental results diverge from the simulated ones. This is due to the full opening of the exhaust valves.

Also in Fig. 4.1, several inflection points on the experimental lines can be understandable from the flow regulation point of view. This was done during the tests so that the flow could be maintained constant. Note that as the carbon dioxide is expelled to the exterior, the interior conditions are changed. So, if there was not any flow regulation, the flow cross section area would remain constant, and due to density variation, the flow would change also. For this reason the flow must be compensated by changing the cross section area, which is controlled by opening/closing the exhaust valve.

This feature shows that this flow controlling procedure is not the most accurate one for this experiment, since the experimental results diverge from the simulated ones. Nevertheless, the difference found here is acceptable.

In this context, test 3 was the one in which the flow control was more imperceptible, and that is why it shows better results among all the tests. As can be viewed from Fig. 4.1 (a) and (b), respectively, the pressure and temperature plots, the experimental results are very close to the ones calculated by the model. Nevertheless, it is perceptible in all trials and plots - Fig. 4.1 (c), (d), (e), (f), (g) and (h) - that until the first flow regulation, the behaviour of the experimental curve is very similar to the simulated one. This validates the computational model used here.

Test 4 deserves a particular analysis and discussion, since initially the reactor is filled with a small quantity of liquid carbon dioxide ( $\chi_0 = 0.96$  and  $h_{l0} = 1.2$  mm, from Tab. 4.2). Due to this small initial liquid quantity, the experimental curves rapidly diverge from the computational ones. When the exhaust valves open, the remaining liquid is vaporized, and with further flow regulation, the saturated conditions are not preserved. Because this flow regulation is smooth, the plots (c) and (d) of Fig. 4.1, does not present any sharp inflection points.

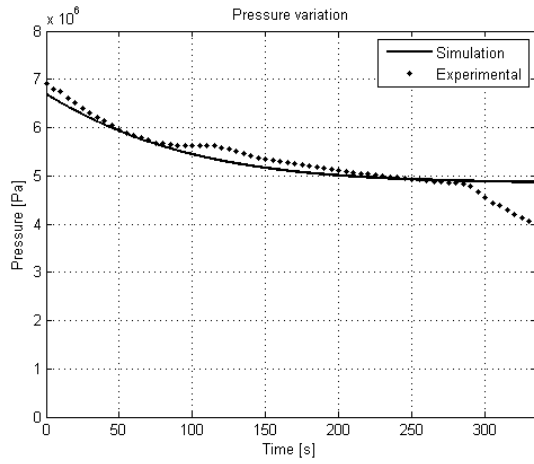


The relative error,  $\epsilon$ , expressed in Tab. 4.2, compares the mass value that enters the reactor with the one that exits. The first is based on the measurement procedure done in the screw-injector, while the second is given by observing the flow meter values. It is calculated by the difference of the intake and exit mass, which is divided by the mass entered in the reactor. Then it is multiplied by 100, so that a percentage can be obtained.

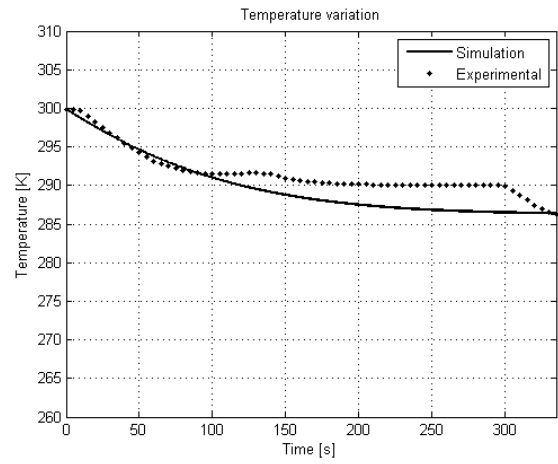
<b>Trial Number</b>		<b>3</b>	<b>4</b>	<b>5</b>	<b>6</b>
$T_o$	[°C]	27.0	27.0	27.0	25.3
$p_o$	$\times 10^5$ [Pa]	1.00	1.00	1.00	1.00
$T_f$	[°C]	11.7	14.1	4.3	7.4
$p_f$	$\times 10^5$ [Pa]	25.52	0.87	1.35	0.96
$V_{in}$	$\times 10^{-6}$ [m <sup>3</sup> ]	84.0	31.9	96.3	99.9
$m_{in}$	$\times 10^{-3}$ [kg]	85.8	32.6	98.3	101.9
$V_{out}$	$\times 10^{-3}$ [m <sup>3</sup> ]	53.05	25.74	50.48	68.36
$m_{out}$	$\times 10^{-3}$ [kg]	94.7	46.0	90.2	122.8
$\Delta t$	[s]	490	245	535	660
$\dot{m}_{CO_2}$	$\times 10^{-3}$ [kg/s]	0.19	0.19	0.17	0.19
$h_{I0}$	$\times 10^{-3}$ [m]	73.9	1.2	85.7	92.8
$h_{If}$	$\times 10^{-3}$ [m]	0	0	0	0
$X_o$		0.10	0.96	0.037	0.011
$X_f$		1	1	1	1
$\epsilon$	[%]	10.4	41.0	8.1	20.5

Tab. 4.2 - Initial and final conditions of the experiment 1 tests.

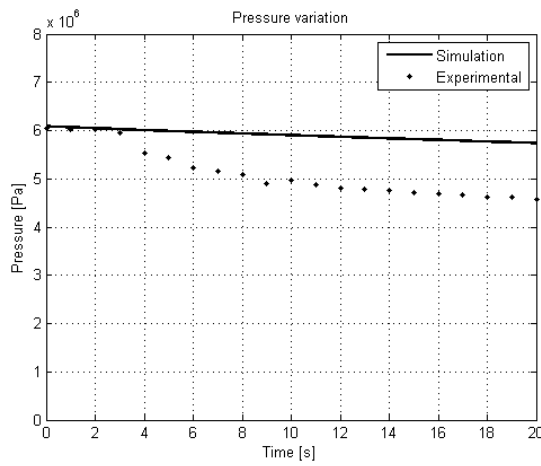
The error values were higher than expected, and several reasons can explain this feature. Firstly the intake mass was calculated by knowledge of the number of full turns made by the screw-injector wheel, which carries an observation error by itself. Further, a 0 °C temperature inside the screw-injector may not be achieved during the trials, carrying an error itself. Moreover, some measurement errors of the flow meter can also explain this type of discrepancies.



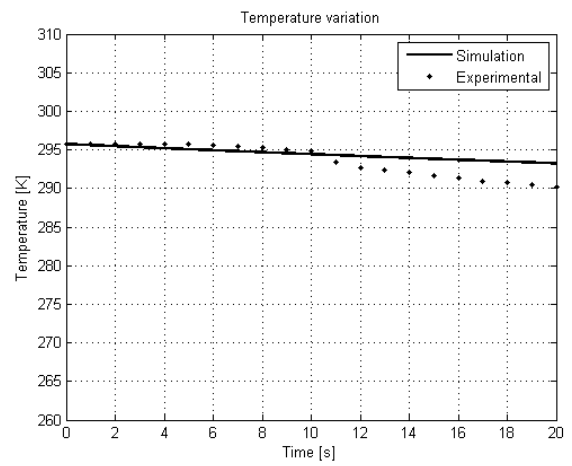
(a) Trial 3 pressure variation



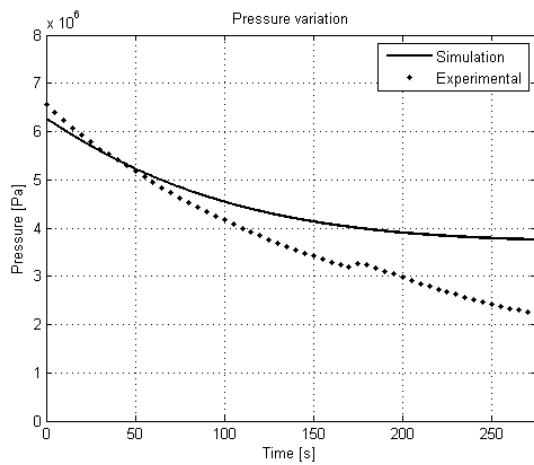
(b) Trial 3 temperature variation



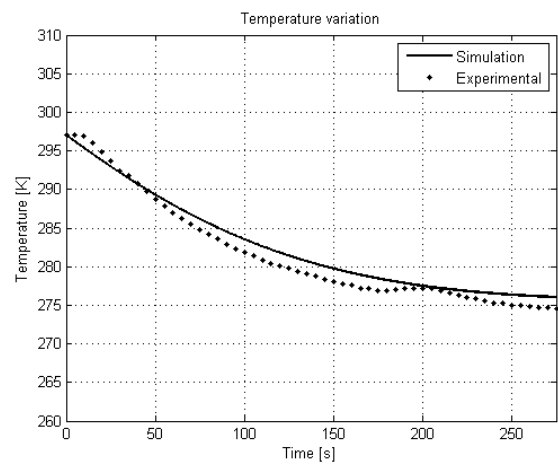
(c) Trial 4 pressure variation



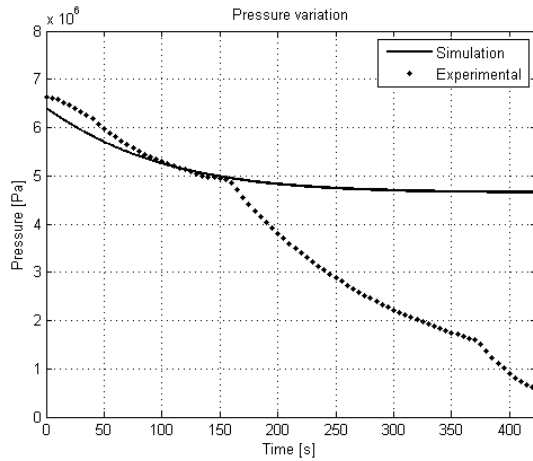
(d) Trial 4 temperature variation



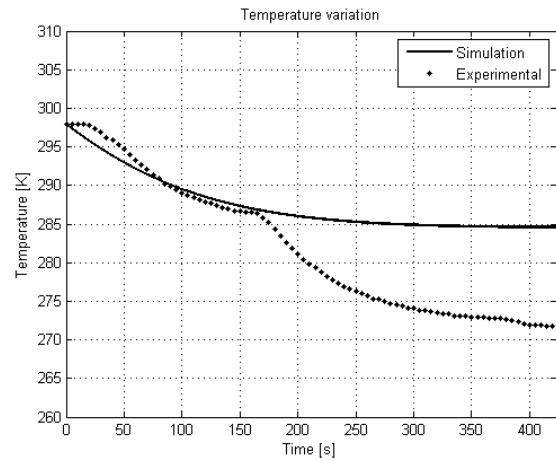
(e) Trial 5 pressure variation



(f) Trial 5 temperature variation



(g) Trial 6 pressure variation



(h) Trial 6 temperature variation

Fig. 4.1 – Simulation and experimental results of experiment 1:

From a simple relative error analysis of the experimental and simulated data, the following Tab. 4.3 can be made.

Trial Number	$\epsilon_{\rho\min}$ [%]	$\epsilon_{\rho\max}$ [%]	$\epsilon_{\rho\text{mean}}$ [%]	$\epsilon_{T\min}$ [%]	$\epsilon_{T\max}$ [%]	$\epsilon_{T\text{mean}}$ [%]
3	0.1	13.3	2.7	0	1.2	0.6
4	0.4	19.2	13.0	0	1.0	0.4
5	0.1	25.1	10.5	0	0.6	0.4
6	0.1	64.7	23.1	0	4.3	2.0

Tab. 4.3 – Relative errors between the experimental and simulated data of experiment 1.

From this table, it can be noticed that in general the pressure relative errors have higher values than the temperature ones. This can be understandable by the fact that the pressure is measured by a pressure sensor installed outside the reactor and it is linked to it through a lengthy line. This carries small losses in the pressure measurements which contribute for these higher relative errors values.

As mentioned before, the constant effort to maintain the same exhaust mass flow during the trials, is also a major contribute for these discrepancies in the pressure relative errors.

## 4.2.2 Experiment 2

In this second experiment the CO<sub>2</sub> vapour is withdraw from the reactor with adiabatic walls. Two tests were validated and its initial and final conditions are described in Tab. 4.4.

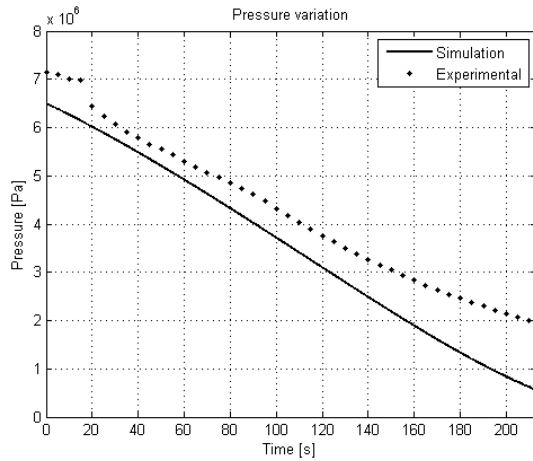
From this table, and as in the first experiment, a similar final carbon dioxide vapour state was reached in the end of these two tests ( $\chi_f = 1$ ), which were confirmed by the final pressure and temperature values ( $p_f$  and  $T_f$ ). This means that saturation conditions were no longer present in the interior of the reactor, the reasons are the same as mentioned earlier in the experiment 1, i.e., full valve opening. This feature can be viewed in the plots of Fig. 4.2.

Trial Number		1	2
$T_o$	[°C]	25.5	24.5
$p_o$	$\times 10^5$ [Pa]	1.00	1.00
$T_f$	[°C]	-2.9	-24.9
$p_f$	$\times 10^5$ [Pa]	0.93	0.95
$V_{in}$	$\times 10^{-6}$ [m <sup>3</sup> ]	101.7	96.4
$m_{in}$	$\times 10^{-3}$ [kg]	103.8	98.4
$V_{out}$	$\times 10^{-3}$ [m <sup>3</sup> ]	58.28	54.22
$m_{out}$	$\times 10^{-3}$ [kg]	104.6	97.7
$\Delta t$	[s]	395	280
$\dot{m}_{CO_2}$	$\times 10^{-3}$ [kg/s]	0.26	0.35
$h_{i0}$	$\times 10^{-3}$ [m]	97.7	75.8
$h_{if}$	$\times 10^{-3}$ [m]	0	0
$\chi_o$		0	0.053
$\chi_f$		1	1
$\varepsilon$	[%]	0.7	0.7

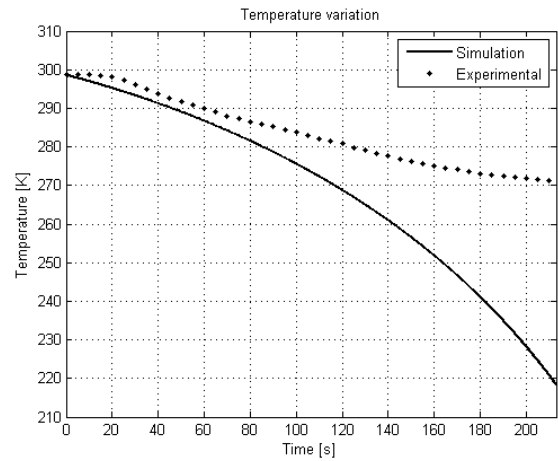
Tab. 4.4 - Initial and final conditions of the experiment 2 tests.

Like in the experiment 1, Fig. 4.2 also shows a divergence increase between the experimental and simulated curves with time. This is due to the mentioned flow regulation, which was necessary to maintain the mass flow during these tests.

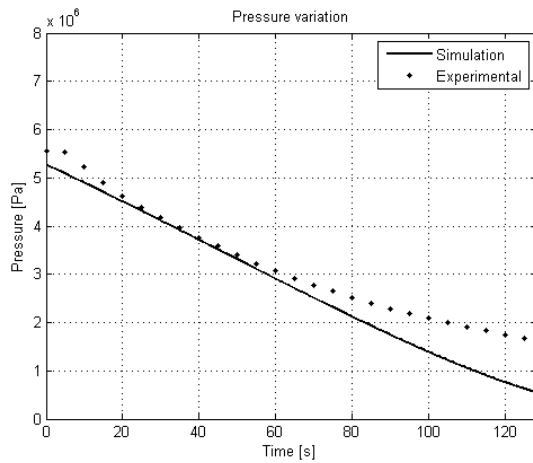
Special remark for the relative error value presented in Tab. 4.4, where here the difference between the inlet mass estimation and the exhaust mass calculated by the flow meter was very small ( $\varepsilon = 0.7\%$ , for both trials). This happens because, in this set of tests, more observations were made in an attempt to minor the measurement errors.



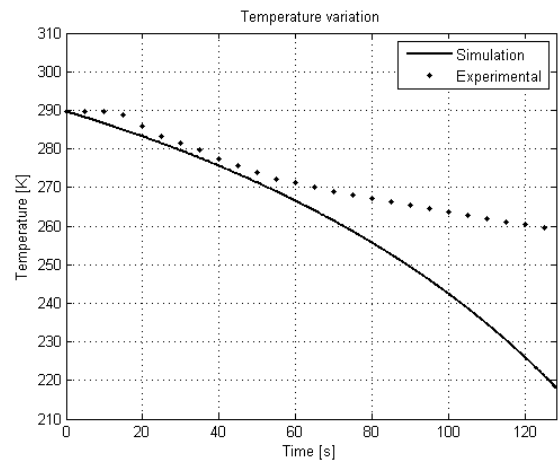
(a) Trial 1 pressure variation



(b) Trial 1 temperature variation



(c) Trial 2 pressure variation



(d) Trial 2 temperature variation

Fig. 4.2 - Simulation and experimental results of experiment 2:

The relative error analysis between the experimental and modelling calculations is resumed in the following Tab. 4.5.

Trial Number	$\epsilon_{pmin}$ [%]	$\epsilon_{pmax}$ [%]	$\epsilon_{pmean}$ [%]	$\epsilon_{Tmin}$ [%]	$\epsilon_{Tmax}$ [%]	$\epsilon_{Tmean}$ [%]
1	4.7	21.6	11.3	0	17.0	4.9
2	1.0	20.3	7.6	0	13.4	3.9

Tab. 4.5 – Relative errors between the experimental and simulated data of experiment 2.

The difference between the pressure and temperature relative errors has the same explanation of experiment 1.

### 4.2.3 Experiment 3

The third experiment was different from the previous two. Here the carbon dioxide inside the adiabatic walled reactor is heated with a cartridge heater, while vapour CO<sub>2</sub> is exhausted to the environment. The cartridge heater power is controlled by a dimmer. The constant imposed heat power was set accordingly some previous calculations, which took into consideration the initial reactor conditions, as mentioned in Tab. 4.6, for the three validated tests.

As can be noticed from this table, liquid carbon dioxide remains inside the reactor in the end of the tests ( $\chi_f > 0$ ). Note that the final height of CO<sub>2</sub> liquid in the interior of the reactor is similar to the height of the heated part of the cartridge heater. This was a safety measure to prevent the cartridge sheath of overheating when in contact with vapour environment. Due to this, the mass relative error calculation was no longer necessary to be estimated.

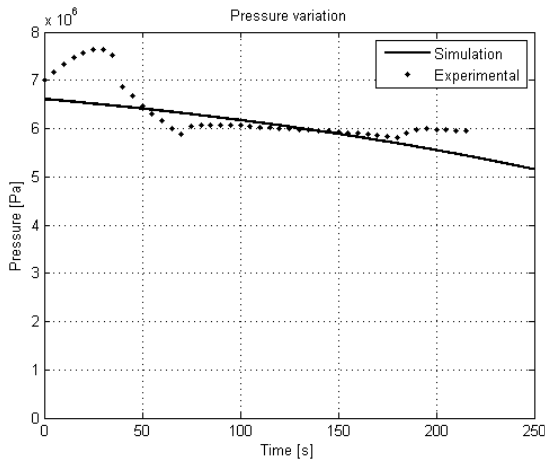
<b>Trial Number</b>		<b>1</b>	<b>3</b>	<b>5</b>
$T_i$	[°C]	26.2	29.4	27.9
$p_i$	$\times 10^5$ [Pa]	70.01	76.50	71.49
$T_f$	[°C]	23.6	29.6	25.3
$p_f$	$\times 10^5$ [Pa]	59.15	74.41	61.94
$V_{in}$	$\times 10^{-6}$ [m <sup>3</sup> ]	92.5	93.9	92.5
$m_{in}$	$\times 10^{-3}$ [kg]	94.4	95.8	94.4
$V_{out}$	$\times 10^{-3}$ [m <sup>3</sup> ]	15.72	15.55	45.75
$m_{out}$	$\times 10^{-3}$ [kg]	28.1	27.8	66.9
$\Delta t$	[s]	215	150	250
$\dot{m}_{CO_2}$	$\times 10^{-3}$ [kg/s]	0.13	0.19	0.11
$h_{l0}$	$\times 10^{-3}$ [m]	86.1	89.3	88.9
$h_{lf}$	$\times 10^{-3}$ [m]	43.3	46.6	44.2
$\chi_0$		0.040	0.028	0.031
$\chi_f$		0.270	0.365	0.290
$P$	[W]	19.7	16.0	3.8

Tab. 4.6 - Initial and final conditions of the experiment 3 tests.

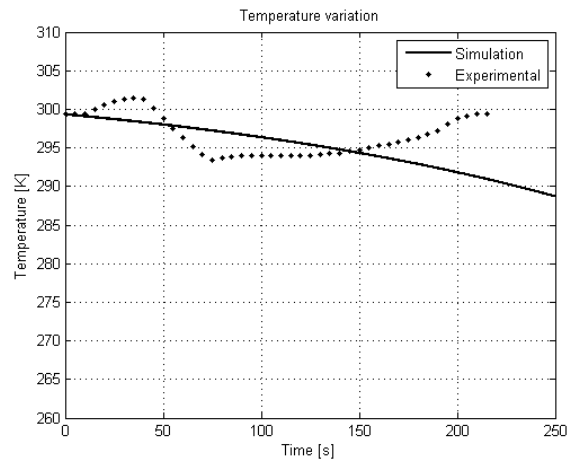
Further, the initial temperature and pressure,  $T_i$  and  $p_i$ , respectively, are measured inside the reactor, while in the other experiments it was used the temperature and pressure outside the reactor,  $T_0$  and  $p_0$ , respectively.

While  $T_0$  and  $p_0$  are very important for the calculation of the total mass exhausted through the flow meter,  $T_i$  and  $p_i$  are important to determine the energy necessary to maintain those conditions until the liquid height of carbon dioxide is above a certain level.

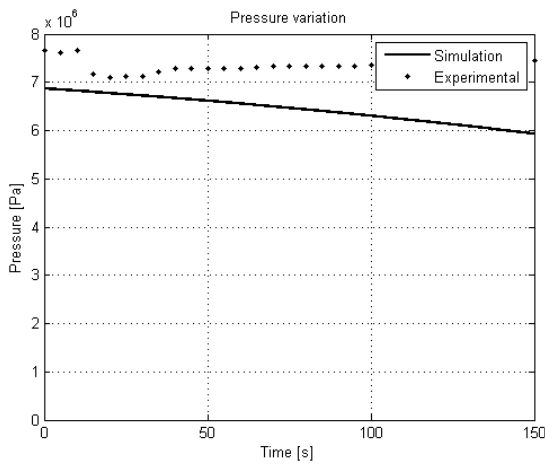
Fig. 4.3 shows the pressure and temperature variation results for the three validated tests. As can be noticed, the experimental results follow the simulated ones, validating the model. Of course, there are some differences which are explained by the difficult control of the exhaust valve. For example, in the beginning of the trials it is noticed a certain flow stabilization. Also, in Fig. 4.3 (c) and (d), it is noticed the effect of constant flow control, which is responsible for the slightly difference in experimental and computational results for test 3.



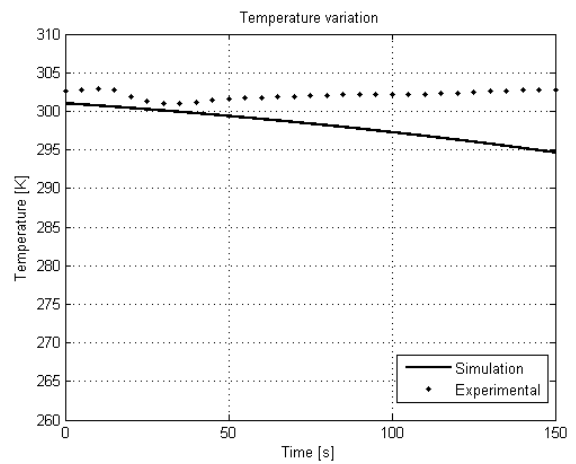
(a) Trial 1 pressure variation



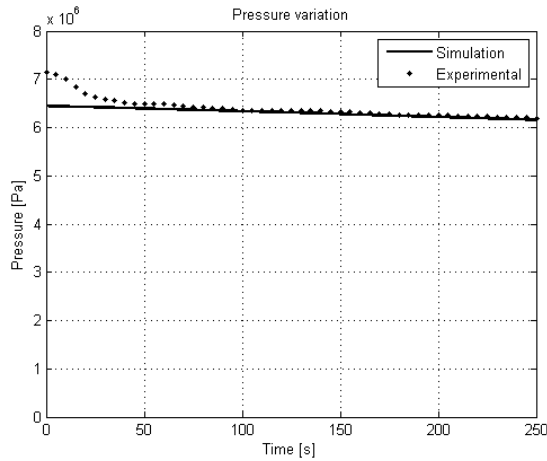
(b) Trial 1 temperature variation



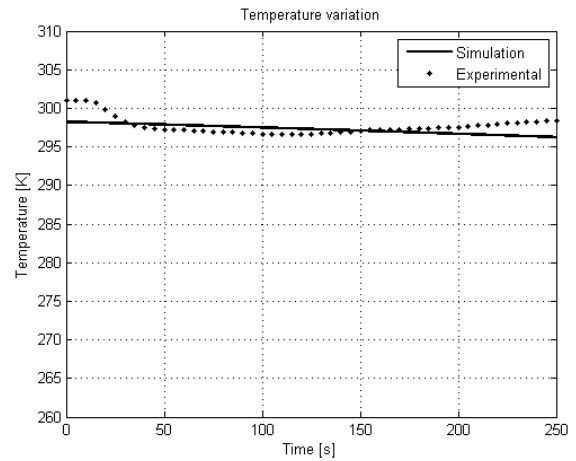
(c) Trial 3 pressure variation



(d) Trial 3 temperature variation



(e) Trial 5 pressure variation



(f) Trial 5 temperature variation

Fig. 4.3 – Simulation and experimental results of experiment 3:

In terms of results, test 5 was the one which produce better results, as can be seen in Fig. 4.3 (e) and (f). This can be explained by the fact that in this test, the cartridge heater was not turned on first and before opening the exhaust valves. As result, the carbon dioxide did not have time to increase pressure and temperature, as it was experienced in the other tests.

Tab. 4.7 shows a relative error analysis of the experimental and modelled data of experiment 3 tests.

Trial Number	$\epsilon_{\rho\min}$ [%]	$\epsilon_{\rho\max}$ [%]	$\epsilon_{\rho\text{mean}}$ [%]	$\epsilon_{T\min}$ [%]	$\epsilon_{T\max}$ [%]	$\epsilon_{T\text{mean}}$ [%]
1	0.1	17.4	4.8	0	2.8	0.8
3	4.8	22.0	13.2	0.3	2.7	1.3
5	0	10.9	1.3	0	2.1	0.8

Tab. 4.7 – Relative errors between the experimental and simulated data of experiment 3.

Taking into consideration the results expressed in this table and the results of the previous experiments, it is obvious that the pressure relative error of test 3 is slightly higher than expected due to the flow control influence.

### 4.3 Hybrid rocket simulation

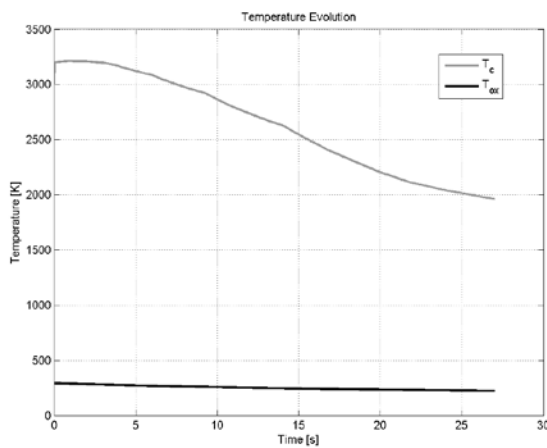
In the following results, the time step used in the simulations was 0.02 s.



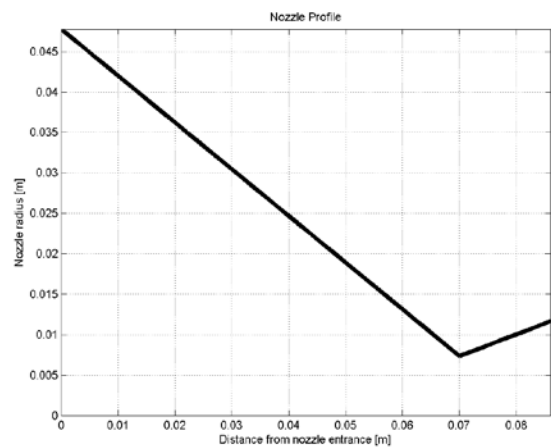
### 4.3.1 Results without heat transfer

The results for a simulation without feedback heat transfer are shown. It should be noted that this simulation still features nozzle cooling. However the heat transferred away from the nozzle is not used to heat the oxidizer tank.

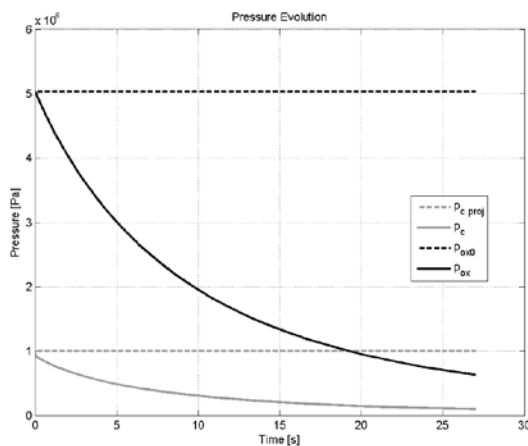
The plots showing the simulation result are shown on the figures of Fig. 4.4. As it can be seen, without heating the oxidizer tank, the initial conditions cannot be maintained. The tank temperature and pressure drop, and so does the mass flow rate. The combustion is sustained by natural vaporization in the tank and lasts for longer than the design indicated, albeit with a very low performance. The mean specific impulse in this simulation is 95.9 s. The simulation ends with the hybrid engine extinguish, since the chamber pressure reaches the ambient pressure. From the pressure and temperature profile plots, it is noticed, that the nozzle flow changes from supersonic to subsonic, during the simulation. It is also noticed that during burning, the nozzle divergent section experiences normal shock waves, which will decrease performance and heat transfer.



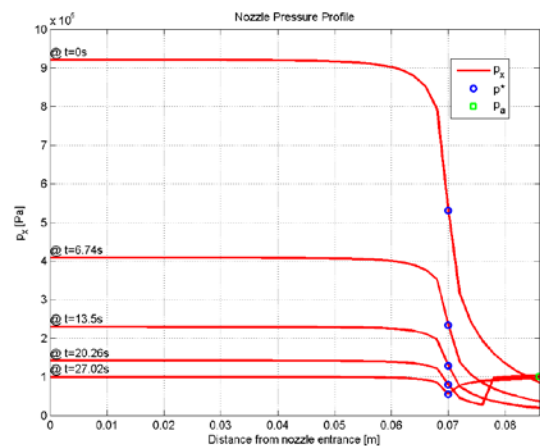
(a) Temperature Evolution



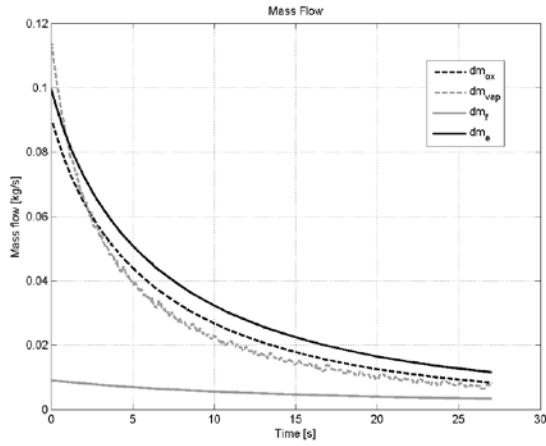
(b) Nozzle Profile



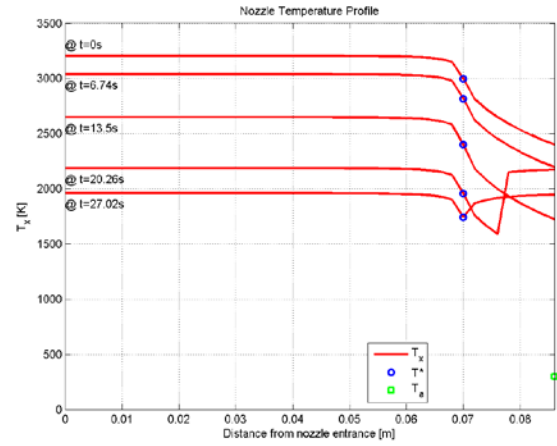
(c) Pressure Evolution



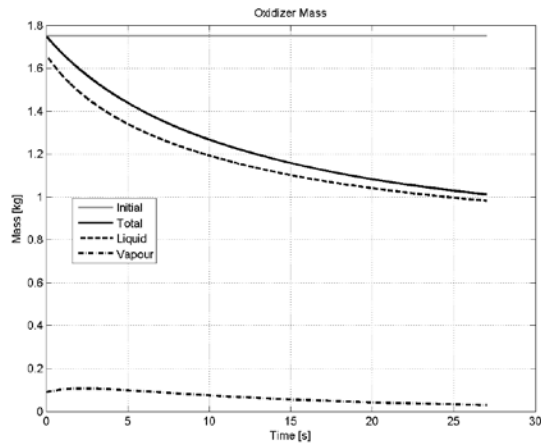
(d) Nozzle Pressure Profile



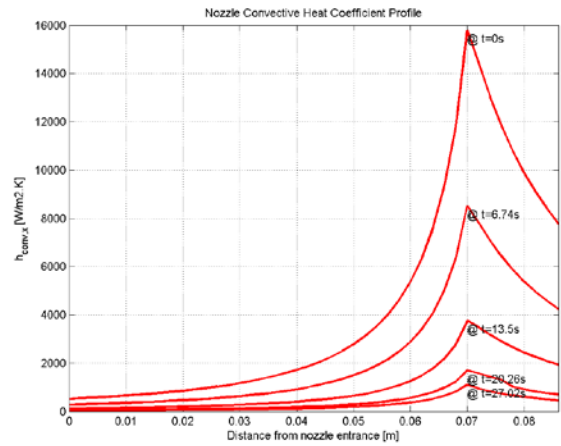
(e) Mass Flow



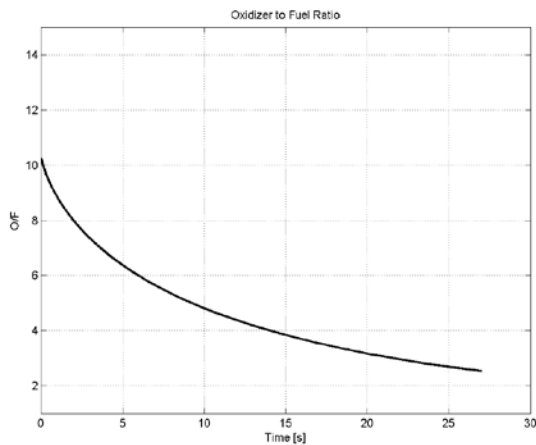
(f) Nozzle Temperature Profile



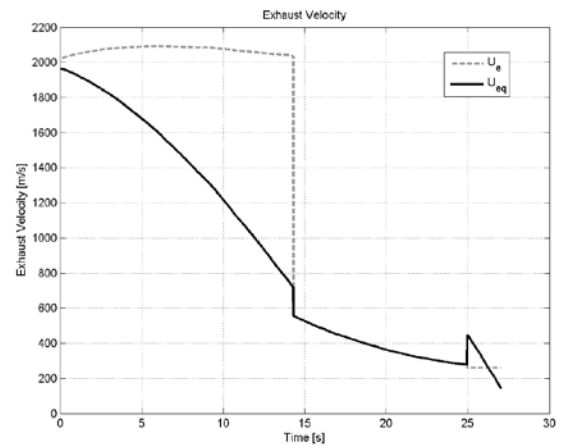
(g) Oxidizer Mass



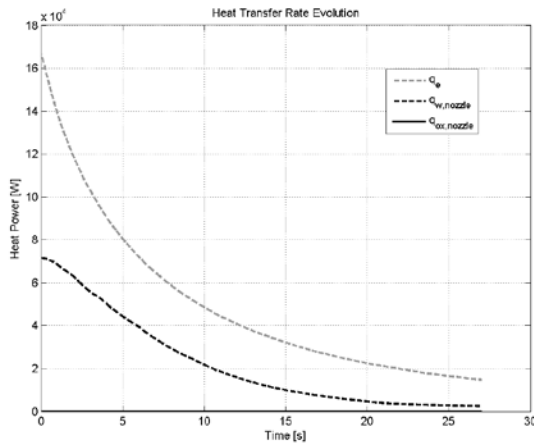
(h) Nozzle Convective Heat Coefficient Profile



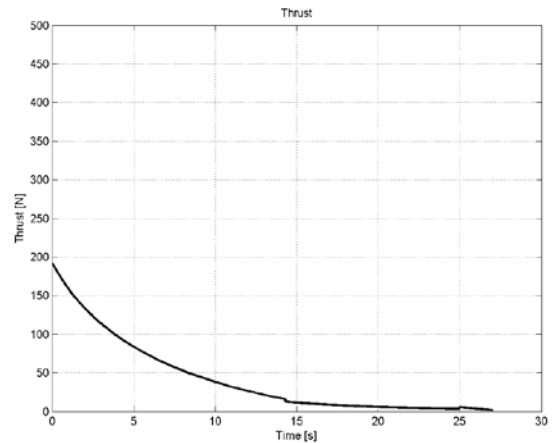
(i) Oxidizer to Fuel Ratio



(j) Exhaust Velocity



(l) Heat Transfer Rate Evolution



(m) Thrust

Fig. 4.4 - Simulation results without heat transfer.

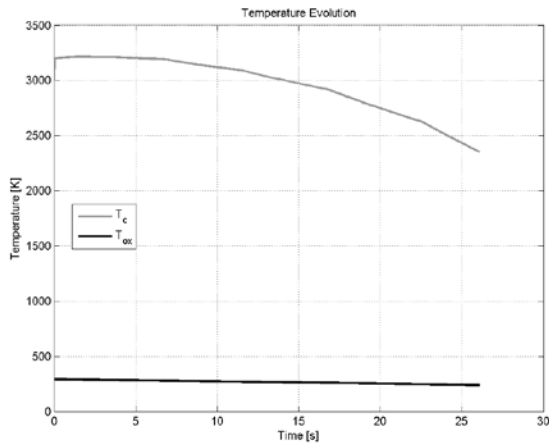
This case is presented as a benchmark to compare the performance of the system with heat transfer.

### 4.3.2 Results with heat transfer

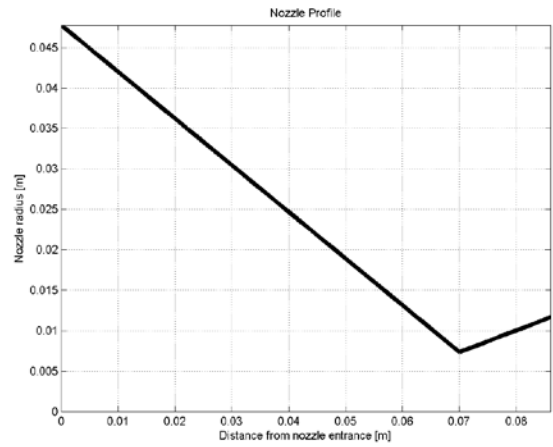
Several simulations were performed with heat transfer. Three particular sets of results will be shown, for the same operating parameters and changing only the fraction of heat rejected from the nozzle that was transferred to the oxidizer tank.

Fig. 4.5 shows the result of a simulation in which there is heat transfer to the oxidizer tank, but it is insufficient to maintain steady conditions in the combustion chamber. This particular simulation is terminated when the fuel is completely burned. It also last longer than the nominal burn time (established as 15 s), since the OF ratio is lower than the design value.

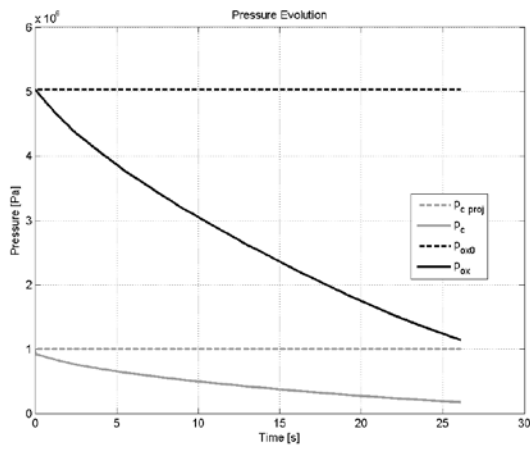
It can be seen, from the exhaust velocity, but also from the pressure and temperature profile plots, that the nozzle flow is supersonic for most of the burning. However, from a certain burning time, a normal shock wave inside the divergent side of the nozzle appears, leading to a sudden reduction of the performance, but also of the heat convection through the walls. The mean specific impulse is 144.6 s. When comparing this case with the one without any heat transfer recovery, a special remark should be made. Here the nozzle remained choked, while in the previous case subsonic flow appeared at the end of the burning.



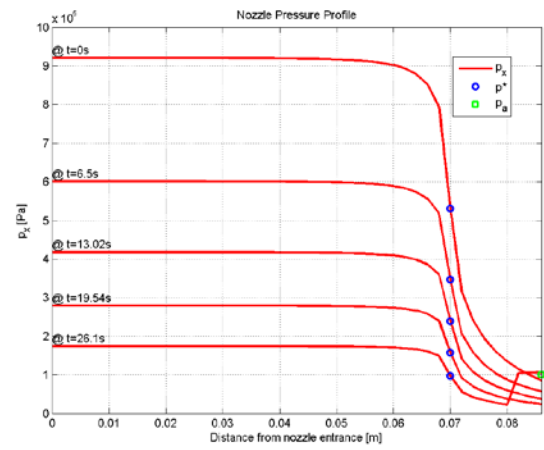
(a) Temperature Evolution



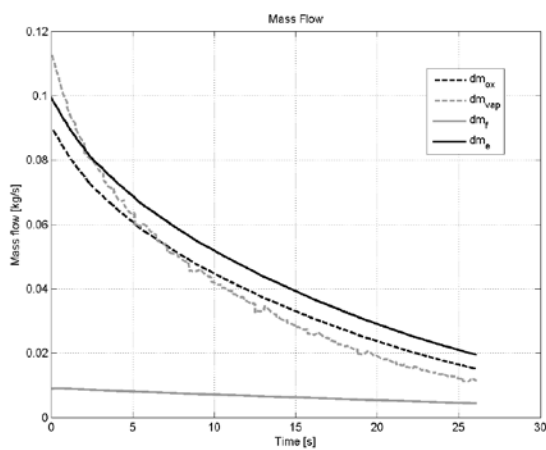
(b) Nozzle Profile



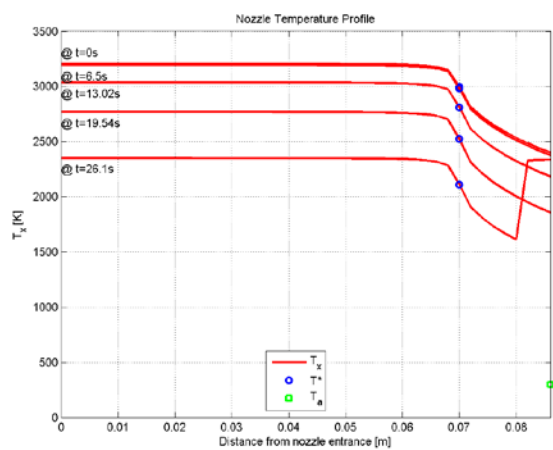
(c) Pressure Evolution



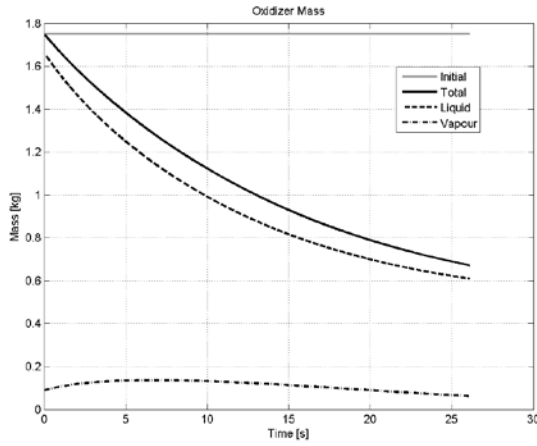
(d) Nozzle Pressure Profile



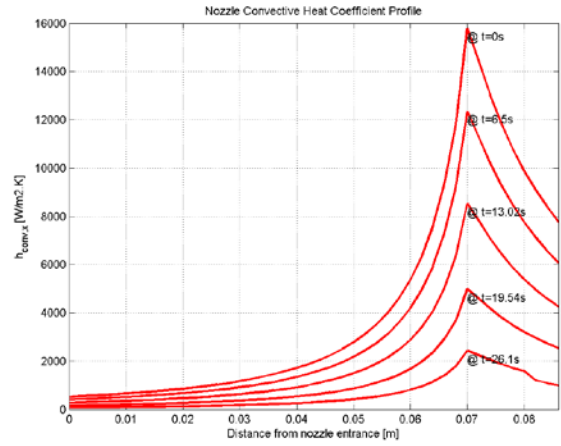
(e) Mass Flow



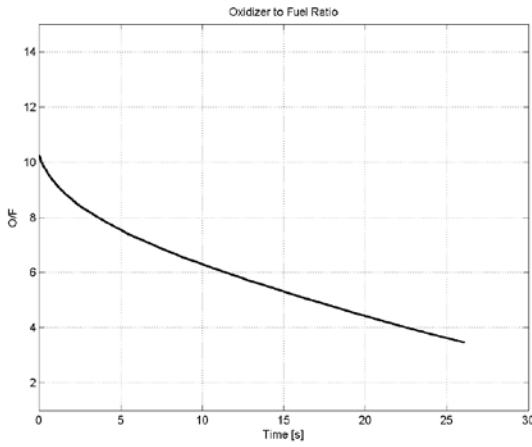
(f) Nozzle Temperature Profile



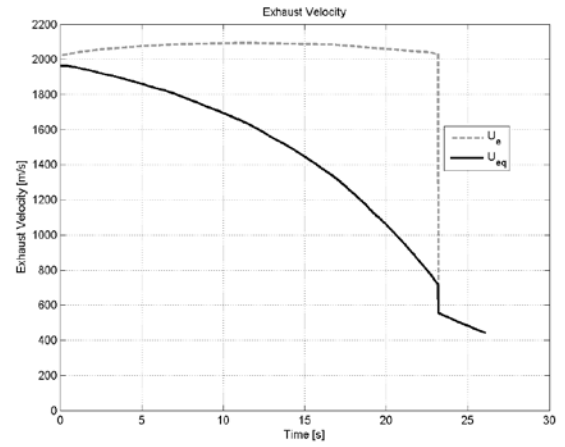
(g) Oxidizer Mass



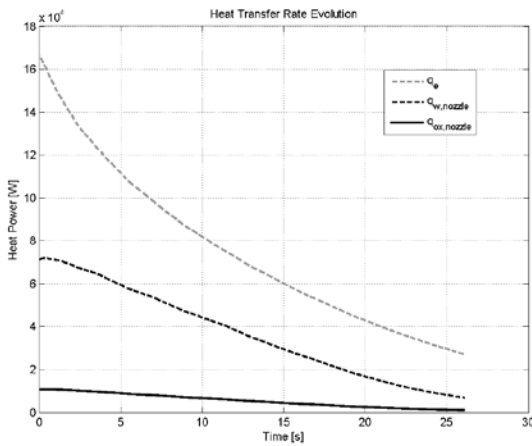
(h) Nozzle Convective Heat Coefficient Profile



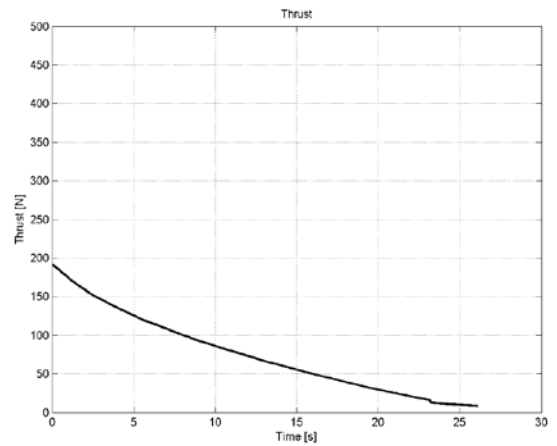
(i) Oxidizer to Fuel Ratio



(j) Exhaust Velocity



(l) Heat Transfer Rate Evolution

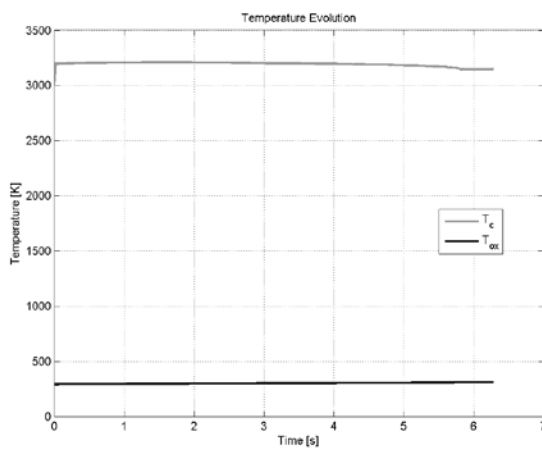


(m) Thrust

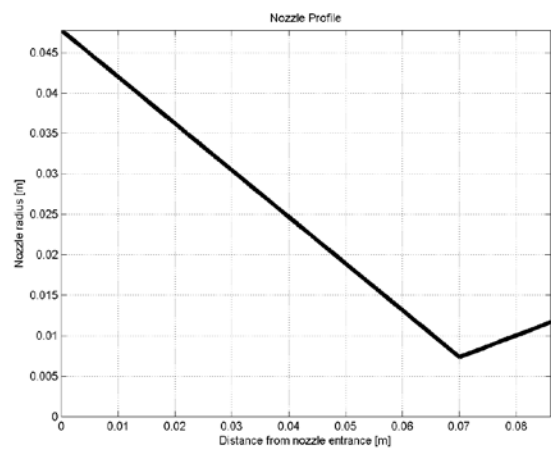
Fig. 4.5 - Simulation results with a heat transfer fraction of 15%.

The plots in Fig. 4.6, show the results of a simulation in which the heat transfer to the oxidizer tank was excessive. It is noticeable that the pressures, temperatures and flow rates increase, though not at a very dramatic rate. This simulation is terminated as the liquid oxidizer ran out (although there is still gaseous oxidizer in the tank). In fact, the simulation is stopped when the gas oxidizer mass is higher than 95 % of the total oxidizer mass. Note that this happened still before the oxidizer mixture in the tank became supercritical.

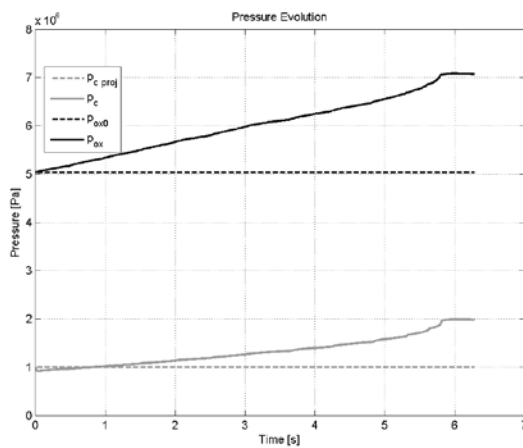
In this case, the flow is entirely supersonic in the nozzle divergent region. With the increase of the combustion chamber pressure, it is noticed that a “under-expanded” behaviour at the nozzle exit. This behaviour influences the performance, as can be viewed in the exhaust velocity and thrust plots. The mean specific impulse is 208.8 s, in this case.



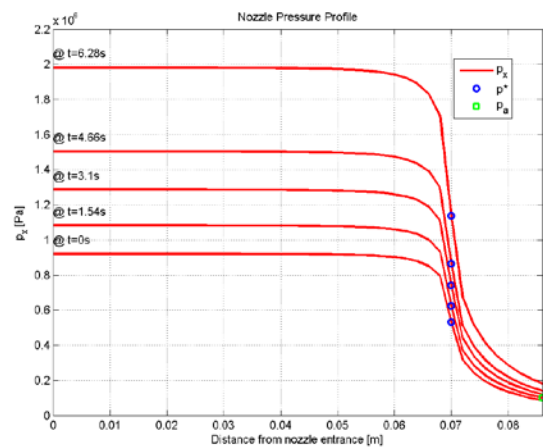
(a) Temperature Evolution



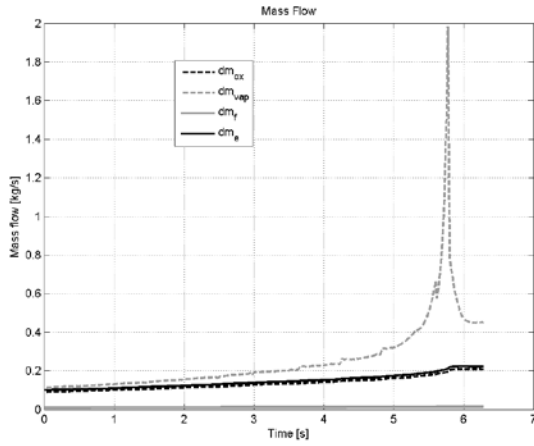
(b) Nozzle Profile



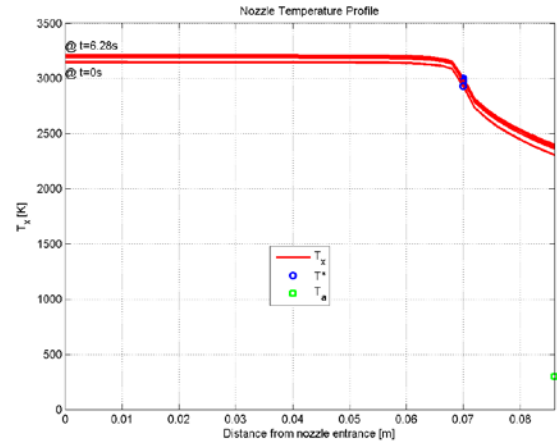
(c) Pressure Evolution



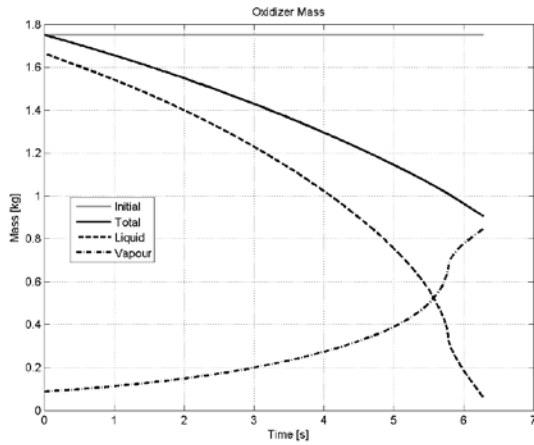
(d) Nozzle Pressure Profile



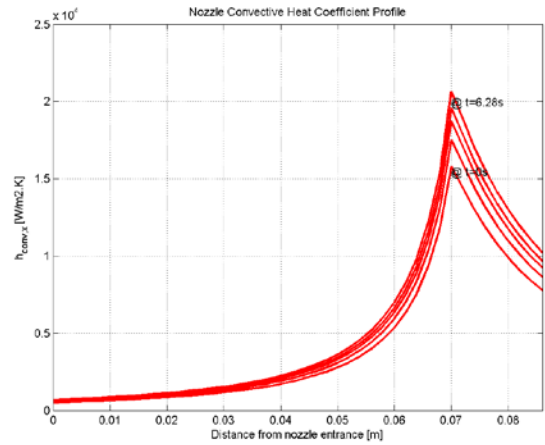
(e) Mass Flow



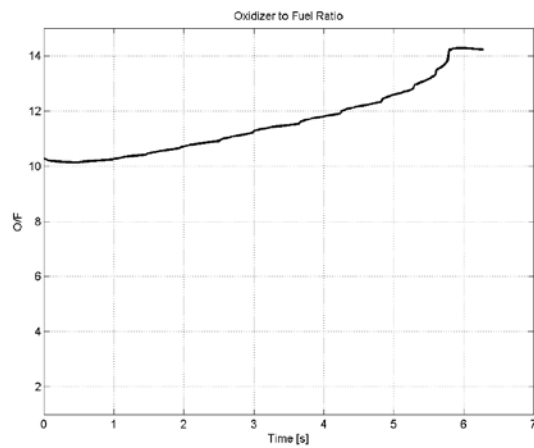
(f) Nozzle Temperature Profile



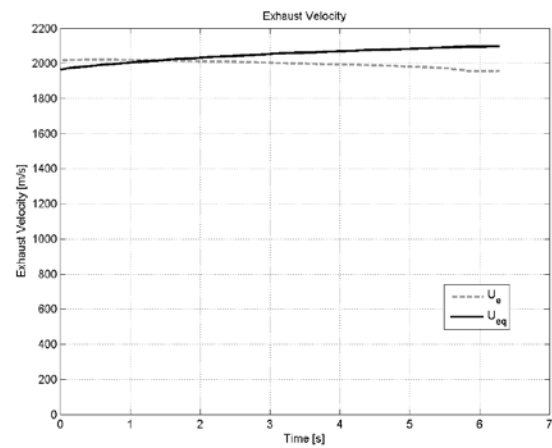
(g) Oxidizer Mass



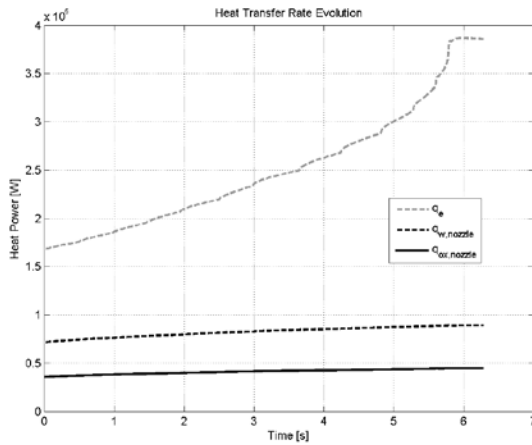
(h) Nozzle Convective Heat Coefficient Profile



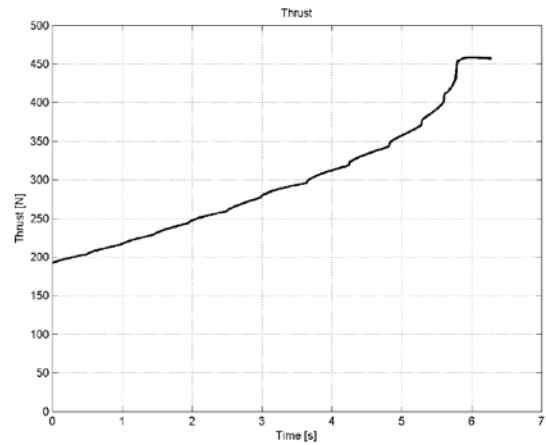
(i) Oxidizer to Fuel Ratio



(j) Exhaust Velocity



(l) Heat Transfer Rate Evolution

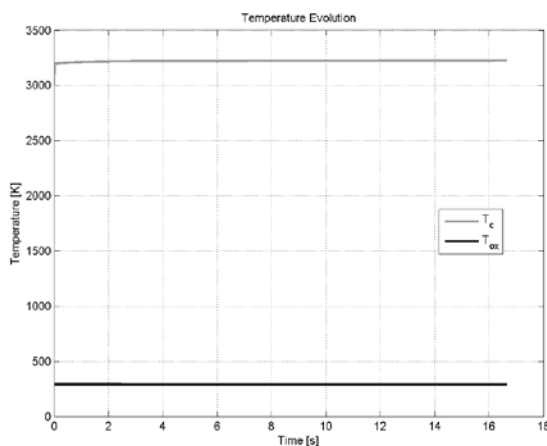


(m) Thrust

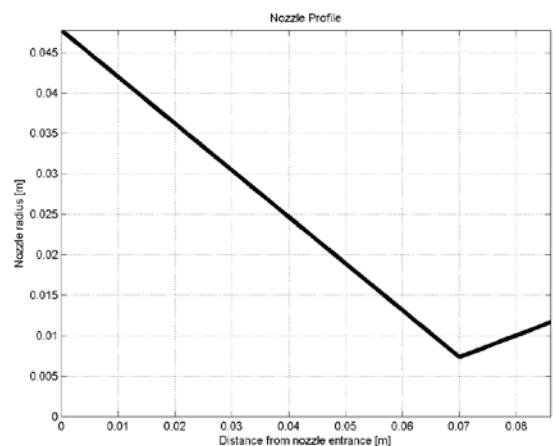
Fig. 4.6 - Simulation results with a heat transfer fraction of 50%.

The burning time decreased significantly, compared with the previous cases (~ 6 s). This is due to higher OF ratios involved in this simulation, leading to the oxidizer mixture condition mentioned above. One last remark goes to the convective heat transfer coefficient which is increasing due to chamber conditions, and leads to an increase in heat transfer and its recovery system.

The results of the simulation in which the chosen heat transfer fraction gave the steadiest burn are given on Fig. 4.7. As the plots show, the temperature and pressure vary very slightly during the burn, both in the chamber and in the tank. The targeted mass flow rate is achieved for most of the time, and the burn time is also on target (slightly higher than 15 s). This simulation was terminated when the liquid fraction of the oxidizer dropped below 5%. And that can explain why by the end of the burn, the tank pressure began to rise.

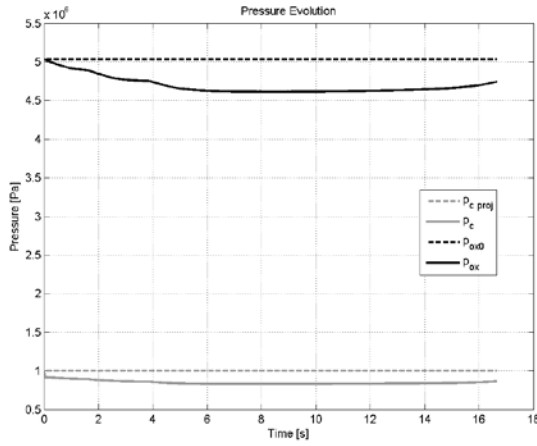


(a) Temperature Evolution

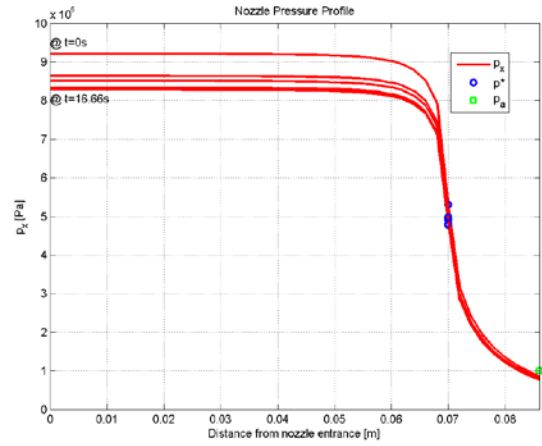


(b) Nozzle Profile

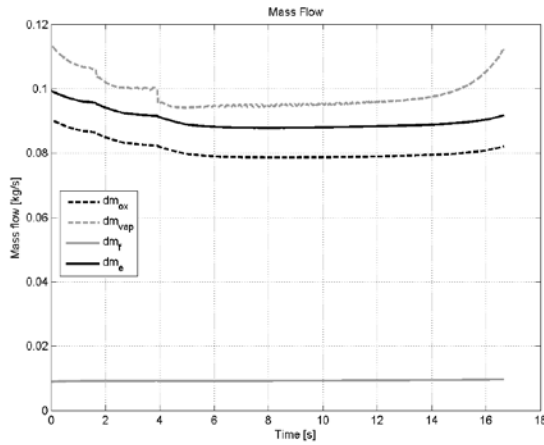




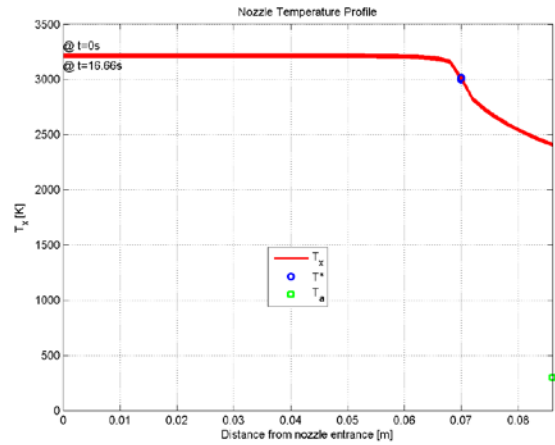
(c) Pressure Evolution



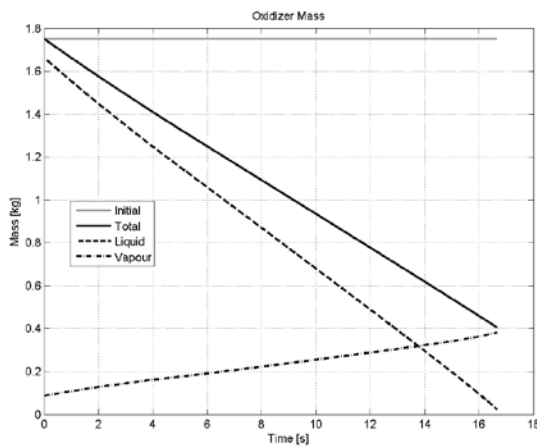
(d) Nozzle Pressure Profile



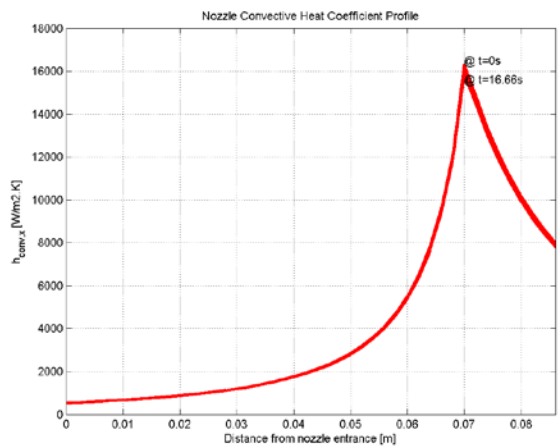
(e) Mass Flow



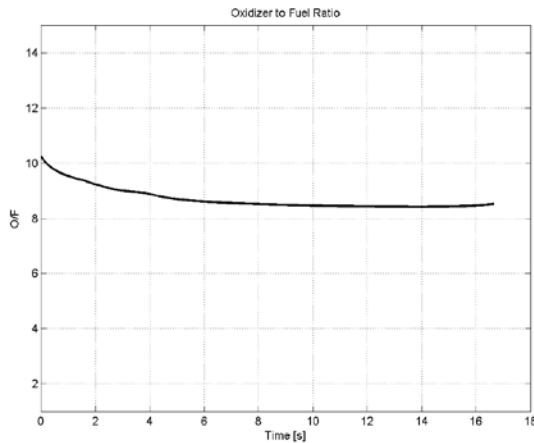
(f) Nozzle Temperature Profile



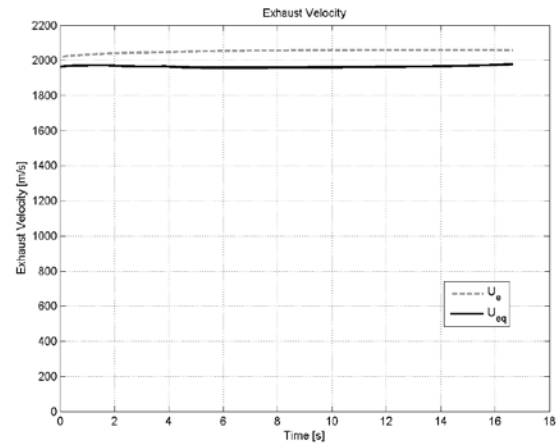
(g) Oxidizer Mass



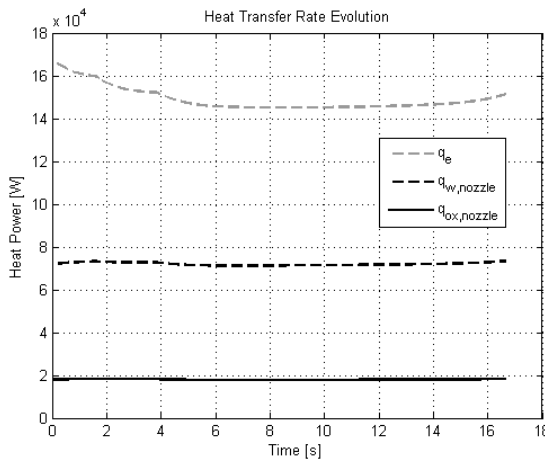
(h) Nozzle Convective Heat Coefficient Profile



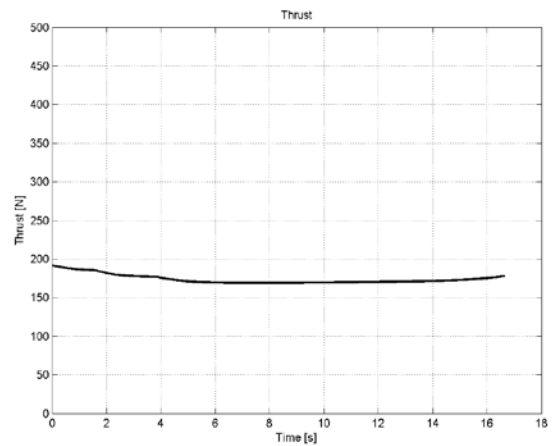
(i) Oxidizer to Fuel Ratio



(j) Exhaust Velocity



(l) Heat Transfer Rate Evolution



(m) Thrust

Fig. 4.7 - Simulation results with a heat transfer fraction of 25%.

It can be observed that during this burn the OF ratio was larger than the design calculations indicated ( $OF = 7.7$ ), closer to a stoichiometric proportion ( $OF = 9.5$ ). The heat rejected by nozzle cooling was also a significant fraction of the energy contained in the exhaust. This can be explained by the relatively low temperature at which the wall was considered to have been maintained (700 K, versus an exhaust temperature above 3000 K). Note that 25% of this heat rejected was recovered to heat the tank oxidizer.

In terms of performance, since the chamber pressure remain levelled, the nozzle flow behaved as predictable, i.e., with a completely supersonic flow on the divergent side of the nozzle. The mean specific impulse retrieved from this simulation is 200.2 s, which is not far of the theoretical project value of 209.6 s. This value was calculated assuming isentropic flow in the nozzle and results from NASA CEA 2 program for the propellant pair chosen in this project, with inputs being  $p_c = 10$  bar  $T_{ox} = 298$  K,  $T_f = 298$  K and  $OF = 7.7$ :  $T_c = 3257.5$  K,  $\rho_c = 0.947$  kg/m<sup>3</sup>,  $c_{p,c} = 4.894$  J/kg.K,  $\gamma_c = 1.1420$ ,  $M_c = 25.659$  kg/kmol,  $U_e = 2056$  m/s and  $F = 206$  N.

## 5 Conclusions and Future Work

### 5.1 Viability

The simulation results and the considerations presented in this document although not conclusive are indicative that the proposed system may be a viable alternative system design in chemical propulsion. Some of the points highlighted throughout the text need to be addressed in the future but, at this stage do not present themselves as prohibitive issues.

### 5.2 Engine stability

The design studies carried out highlighted the functioning of the engine, as well as its stability features. The main conclusion to be drawn is that, in its current embodiment (i.e.: non-inverted hybrid with no control valves), the engine is not stable as it was initially thought (ex: for long burns the trend is not for a feedback loop returning to the initial parameters).

The inclusion of a sonic throat for gaseous oxidizer injection, although important for safety, does not appear to have any appreciable overall effect on stability. This is an important conclusion since one of the points to be clarified by simulation was if stability was dependent on gaseous reactant injection being sonic or subsonic. In a sonic injection, the flow is choked, thus “blind” to the difference between tank and chamber pressures. In a subsonic injection, the flow is dependent of this pressure difference. Nevertheless, a gaseous oxidizer injection can have some advantages in the quality of the combustion, since the oxidizer is already vaporized.

The recovered (or feedback) heat transfer also does not add to the stability of the system, although it might be tailored to offer a reasonable constant performance throughout the entire burn. The main issue with the stability of a passive feedback heat transfer is a result of two separate phenomena. These phenomena are illustrated in Fig. 3.4 and Fig. 3.2.

In the range of temperatures that the proposed system is expected to operate the enthalpy of vaporization falls drastically with a temperature increase (see red line in Fig. 3.4). The obvious consequence is that, as the oxidizer tank is heated and its temperature rises, less heat is necessary to heat it further. Maintaining a constant heating power while the temperature is allowed to rise will lead to runaway vaporization of oxidizer, with a subsequent increase in tank temperature and pressure. In fact, this was what happened in the simulation of 50% heat transfer recover to the oxidizer tank.

This rise in pressure in the tank will lead, despite the sonic condition at the injection orifice being verified or not, to an increase in the mass flow rate of the oxidizer to the chamber, thereby increasing the OF ratio. The optimal OF ratio for the engine corresponds to the peak of combustion products temperature shown in Fig. 3.2.

As Fig. 3.2 shows, the exhaust temperature, and consequently the amount of heat transferred by a completely passive system will decrease to either side of the optimal OF ratio. However, the decrease towards a leaner combustion (high OF) is much shallower than the decrease towards a richer combustion (low OF). The simulation has shown this very mild stabilizing effect is not quite sufficient to counteract the rate of pressure increase in the tank.

This problem manifests itself in simulation results in the different evolutions of the tank and chamber pressure throughout the burn for different feedback heat transfer efficiencies. There is an optimum efficiency value for a given engine sizing and proportion that allows stable and reasonably constant conditions throughout the burn. However, even slight deviations from this value lead to either rising or falling of tank and chamber pressure.

At this stage, there are multiple solutions envisaged for this problem. The most obvious is the use of a feedback heat transfer system that actively controls the amount of heat transferred to the oxidizer during the burn. Such system would ensure optimal and even performance of the engine, as well as adding another operational control level. However, its implementation would necessarily detract from the desired simplicity of the system as originally proposed.

Another solution would be to alter the propellant combination in order to cause a sharper drop in combustion temperature for higher OF ratios. If this drop would be large enough, the system would be truly self-stable with a completely passive feedback heat transfer mechanism. This solution may also be implemented by using a reverse hybrid, with a gaseous fuel and a solid oxidizer. In this case, an excessive heating would cause the OF ratio to decrease, and the combustion temperature would drop a more substantial amount, causing the system to be stable. Nevertheless, required efforts for studies and experiments on characterizing such oxidizer-fuel combinations would need to be made.

A compromise solution may be using some safety tank valves to release some oxidizer. A solution that is very common in the state-of-the-art rocketry.

### **5.3 Test program and future developments**

Regarding the test program, there are two critical areas in which experimental validation work should be done preliminarily. One of these areas is the validation of the simulation regression rate.

As mentioned, it was used an equation found in the literature (Bertoldi, 2007), which is empirical and based on various values, including geometric ones. For this reason it should be done further experimental tests, in order to validate and update the equation according to this hybrid rocket engine geometry.

The other critical area that should be the object of a more detailed study is the mechanism of heat transfer from the nozzle to the tank. The simulation work presented above did not cover in detail how this transfer is done, although considerations were made regarding the limitations of the process. In a future engine based on the proposed system, the ideal solution would be to use heat conduction to transfer the heat. The limitations outlined above must be taken into account for the design of the nozzle and a more detailed design and simulation work regarding the geometry should be performed to assess the feasibility and limitations of using conductive heat transfer as a mechanism. Alternatively, a heat transfer system based on heat exchangers (using a separate working fluid) can also be studied in more detail.

It will be also of great interest to control the amount of oxidizer tank heating. Therefore, the suggestion made earlier of decoupling the nozzle cooling system from the oxidizer tank heating system is highly recommended, especially for an experimental setup.

As a final conclusive statement it seems highly promising a system design based on the concept of using heat transfer from at least the nozzle to control vapour pressure of a liquid propellant for pumping it into the combustion chamber as a gas.

## 6 References

- Almeida, L. A. R., Santos, L. M. C., (2005).** *Projecto, Construção e Lançamento de um Foguete Híbrido a Base do Par Propelente Parafina – N<sub>2</sub>O*. Projecto de Graduação. Universidade de Brasília, 83.
- Berger, B., (2007).** Is nitrous oxide safe? [Online]. 5 October, Swiss Propulsion Laboratory, Switzerland. [Consulted in 1 May 2013]. Available in WWW:<URL: [http://www.spl.ch/publication/SPL\\_Papers/N2O\\_safety\\_e.pdf](http://www.spl.ch/publication/SPL_Papers/N2O_safety_e.pdf) >
- Bertoldi, A. E. M., (2007).** *Avaliação Experimental da Queima de Parafina e Óxido Nitroso em Motores Híbridos*. Dissertação de Mestrado. Universidade de Brasília.
- Carmiciono, C., Sorge, A. R., (2005).** Role of Injection in Hybrid Rockets Regression Rate Behaviour. *Journal of Propulsion and Power*, 21 (4), 606-612.
- Casalino, L., Pastrone, D., (2002).** Optimal Design of Hybrid Rockets for Small Satellites. 38<sup>th</sup> AIAA/ASME/SAE/ASEE Joint Propulsion Conference & Exhibit. Indianapolis, Indiana.
- Chang, S.Y., Lee, C., Shin, K.S., (2005).** “The Enhancement of Regression Rate of Hybrid Rocket Fuel by Various Methods”, 43<sup>rd</sup> AIAA – Aerospace Sciences Meeting and Exhibit, Reno, Nevada.
- Chemical Equilibrium with Applications, CEA.** NASA Computer Program CEA [Online]. Glenn Research Center, Cleveland, OH, United States of America. [Consulted in 1 May 2013]. Available in WWW:<URL: <http://www.grc.nasa.gov/WWW/CEAWeb/> >.
- Chiaverini, M. J., Serin, N., Johnson, D. K., Lu, Y., Kuo, K. K., Risha, G. A., (2000).** Regression Rate Behaviour of Hybrid Rocket Solid Fuels. *Journal of Propulsion and Power*, 16 (1), 125-132.
- Contaifer, R. A., (2006).** *Qualificação e Testes de Voo do Foguete SD 1*. Trabalho de conclusão de curso. Universidade de Brasília.
- George, P., Krishnan, S., Varkey, P. M., Ravindran, M., Ramachandran, L., (2001).** Fuel Regression Rate in Hydroxyl-Terminated-Polybutadiene/Gaseous-Oxygen Hybrid Rocket Motors. *Journal of Propulsion and Power*, 17 (1), 35-42.
- Gordon, S., McBride, B. J., (1994).** *Computer Program for Calculation of Complex Chemical Equilibrium Compositions and Applications – I. Analysis*. NASA Reference Publication 1311.
- Gouvêa, L. H., (2007).** *Análise de Desempenho de um Motor Híbrido utilizando Parafina e Peróxido de Hidrogénio como Propelentes*. Dissertação de Mestrado. Instituto Nacional de Pesquisas Espaciais, 138.
- Humble, R. W., Henry, G. N., Larson, W. J., (1995).** *Space Propulsion Analysis and Designer*. MacGraw-Hill Companies, Inc. Primis Custom Publishing.

**Incropera, F. P., DeWitt, D. P., (2002).** *Fundamentals of Heat and Mass Transfer – Fifth Edition.* United States of America: John Wiley & Sons, Inc.

**Jansen, D. P. L. F., Kletzki, Ph., (1998).** Preliminary Design of a 3 kN Hybrid Propellant Engine. *ESA Journal*, Vol. 12, 421-439.

**Liepmann, H. W., Roshko, A., (1957).** *Elements of Gas Dynamics.* United States of America: John Wiley & Sons Inc.

**Lyne, J. E., Naoumov, V. I., Scholes, J., Dodge, M., Elton, B., Wozniak, P., Austin, D., Combs, C., (2005).** First Steps in the Development and Testing of Nontoxic, Bioderived Fuels for Hybrid Rocket Motors. *43<sup>rd</sup> AIAA Aerospace Sciences Meeting and Exhibit*, AIAA 2005-741, 10-13 January, Reno, Nevada.

**Longman Dictionaries, (1995).** *Longman Dictionary of Contemporary English – Third Edition.* England: Longman Group Ltd.

**Karabeyoglu, B. J., Ziliac, A., Cantwell, G., DeZilwa, S., Castellucci, P., (2004).** Scale-Up Tests of High Regression Rate Paraffin-Based Hybrid Rockets Fuel. *Journal of Propulsion and Power*, 20 (6), 1037-1045.

**Karabeyoglu, A., Dyer, J., Stevens, J. and Cantwell, B., (2008).** Modeling of N<sub>2</sub>O Decomposition Events. *44<sup>th</sup> AIAA/ASME/SAE/ASEE Joint Propulsion Conference & Exhibit*, AIAA 2008-4933, 21-23 July, Hartford, CT.

**Korting, P. A. O. G., Schöyer, H. F. R., Timnat, Y. M., (1987).** Advanced Hybrid Rocket Motor Experiments. *Acta Astronautica*, 15 (2), 97-104.

**McBride, B. J., Gordon, S., (1996).** *Computer Program for Calculation of Complex Chemical Equilibrium Compositions and Applications – II. Users Manual and Program Description.* NASA Reference Publication 1311.

**Moran, M. J., Shapiro, H. N., (2000).** *Fundamentals of Engineering Thermodynamics – 4<sup>th</sup> Edition.* United States of America: John Wiley & Sons, Inc.

**NIST Chemistry WebBook, NIST.** Thermophysical Properties of Fluid Systems [Online]. United States of America. [Consulted in 1 May 2013]. Available in WWW: <URL: <http://webbook.nist.gov/chemistry/fluid/> >

**Pardal, T. C. D. (2012).** Propulsion System. Omnidea Lda. Portugal – WIPO PCT International Patent. Patent number: WO 2013/048271 A1 - PCT/PT2012/000027. 5 July 2012.

**Risha, G. A., Boyer, E., Wehrman, R. B., Kuo, K. K., (2002).** Performance Comparison of HTPB-Based Solid Fuels Containing Nano-Sized Energetic Powder in a Cylindrical Hybrid Rocket Motor. *38<sup>th</sup> AIAA/ASME/SAE/ASEE Joint Propulsion Conference and Exhibit*, AIAA 2002-3576, 7-10 July, Indianapolis, Indiana.

**Rocket Propulsion Analysis, RPA.** Thermodynamic data [Online]. Russia. [Consulted in 1 May 2013]. Available in WWW:<URL: [www.propulsion-analysis.com/downloads/thermo/thermo.lib](http://www.propulsion-analysis.com/downloads/thermo/thermo.lib) >.

**Santos, L. M. C., Almeida, L. A. R., Fraga, A. M., Veras, C. A. G., (2004).** Experimental Investigation of a Paraffin Based Hybrid Rocket. *10<sup>th</sup> Brazilian Congress of Thermal Sciences and Engineering*, Rio de Janeiro.

**Scaled Composites, (2009).** Scaled Composites Safety Guidelines for N<sub>2</sub>O [Online]. 17 June, Mojave, CA, United States of America. [Consulted in 1 May 2013]. Available in WWW: <URL: <http://www.scaled.com/images/uploads/news/N2OSafetyGuidelines.pdf> >.

**Scaled Composites, SC.** Scaled Composites, LLC [Online]. Mojave, CA, United States of America. [Consulted in 1 May 2013]. Available in WWW: <URL: <http://www.scaled.com/> >.

**Space Propulsion Group, SPG.** Space Propulsion Group, Inc. [Online]. Silicon Valley, CA, United States of America. [Consulted in 1 May 2013]. Available in WWW: <URL: <http://www.spg-corp.com/> >.

**Sutton, G. P., (1992).** *Rocket Propulsion Elements – 6<sup>th</sup> Edition*. United States of America: John Wiley & Sons, Inc.

**Thicksten, Z., Macklin, F., Campbell, J., (2008).** Handling considerations of Nitrous Oxide in Hybrid Rocket Motor Testing. *44<sup>th</sup> AIAA/ASME/SAE/ASEE Joint Propulsion Conference & Exhibit*, AIAA 2008-4830, 21-23 July, Hartford, CT.

**White, F. M., (2002).** *Mecânica dos Fluidos – 4<sup>a</sup> Edição*. Rio de Janeiro, RJ: McGraw-Hill Interamericana do Brasil.

**Whitmore, S. A., Chandler, S. N., (2010).** Engineering Model for Self-Pressurizing Saturated - N<sub>2</sub>O - Propellant Feed Systems. *Journal of Propulsion and Power*, 26 (4), 706-714.

**Zakirov, V., Sweeting, M., Lawrence, T., Sellers, J., (2001).** Nitrous Oxide as a Rocket Propellant. *Acta Astronautica*, 48 (5-12), 353-362.

**Zakirov, V. A., Li, L., (2005).** 1-D, Homogeneous Liquified Gas Self-Pressurization Model. *European Conference for Aerospace Sciences (EUCASS)*, Session 5.11.01, 4-7 July, Moscow, Russia.

**Zandbergen, B. T. C., (2007).** *Thermal Rocket Propulsion (version 2.03)*. TU Delft.

**Zandbergen, B.T. C.** Hybrid Rocket Motors. [Online] TU Delft, Delft, Netherlands. [Consulted in 1 May 2013]. Available in WWW: <URL: <http://www.lr.tudelft.nl/en/organisation/departments/space-engineering/space-systems-engineering/expertise-areas/space-propulsion/propulsion-options/chemical-rockets/hybrid/> >.



## Appendix

### A. Ariane 5 Space Rocket Launcher



Fig. 0.1 – Vulcain 2 rocket engine, from Astrium, that powers the Ariane 5 (LOX/LH<sub>2</sub>). With regenerative cooling system that supports the combustion chamber and also the active cooled nozzle by dump flow.

The European Ariane 5 space rocket launcher is a good example to illustrate the numbers behind such mission. The launcher is capable of lifting a 40 tons payload into a low Earth orbit (LEO) or a 6.8 tons payload into geostationary transfer orbit (GTO). It requires 3 stages to do that. A large core stage, called main stage, has attached to it two booster rockets and a smaller core stage on the top of the main one. The two booster rockets assist the core stage during the initial 130 s launch phase. After burn-out these two boosters are separated from the main core stage, which continues the ascent flight. After 590 s of flight the main core stage burn-out and is separated. The second core stage takes over bringing the payload to its intended launch orbit. The total launcher mass at lift-off is about 746 tons, of which 642 tons is propellant (~86 % of total mass). The main stage is powered by a single liquid rocket engine (Vulcain), which provides for both main vehicle thrust as well as launcher yaw and pitch control. It produces 1145 kN of vacuum thrust and has a nominal burn time of 590 s, as mentioned. Total stage mass is approximately 170 tons and maximum propellant mass is around 155 tons (130 tons of oxidizer and 25 tons of fuel). Stage lengths and diameter are 29 m and 5.4 m, respectively. The larger booster rockets (solid rockets) each provides thrust for about 130 s. During this time each booster provides a total thrust of  $4.6 \times 10^8$  N. Thrust at lift-off is 5.5 MN, which reduces to about 4.0 MN at 35 – 55 s to minimize aerodynamic loads. Maximum thrust is around 6.0 MN. The thrust tails off after 75 s to limit maximum launcher acceleration down to  $3.5 g_0$ . The second core stage is propelled by a single rocket engine called Aestus. It produces 27.5 kN of thrust. Total propellant mass is 9.7 tons stored in 4 propellant tanks. The *Étage à Propergols Stockables* (Storable Propellant Stage) or EPS stage is spin stabilized. Its attitude control system consist of six 400 N (each) thrusters. Two of them are used for spin-up and other two to spin-down. The remaining two are to allow tilting the spin axis.

## B. Specific impulse

According to Sutton (1992), the specific impulse  $I_{sp}$  is the total impulse per unit weight of propellant. If the total mass flow rate of propellant is  $\dot{m}$  and the standard acceleration of gravity at sea level is  $g_0$ , then:

$$I_{sp} = \frac{\int_0^t F \cdot dt}{g_0 \cdot \int_0^t \dot{m} \cdot dt}$$

This equation will give a time-averaged specific impulse value for any rocket propulsion system, particularly where the thrust varies with time. During transient conditions (during start or the thrust build up period, the shutdown period, or during a change of flow or thrust levels) values of  $I_{sp}$  can be obtained by integration or determining average values for short time intervals for  $F$  and  $\dot{m}$ .

For constant propellant mass flow  $\dot{m}$ , constant thrust  $F$ , and negligibly short start or stop transients:

$$I_{sp} = \frac{F}{\dot{m} \cdot g_0} = \frac{F}{\dot{w}}$$

In the metric Standard International (SI) system of units  $I_{sp}$  is expressed simply in "seconds". However, it is really a thrust force per unit weight flow. Specific impulse is then a measure for the performance of a rocket propulsion system.



```

    = N2O(Tox0);           %Oxidizer initial properties
pot0 = pox0;             %Oxidizer tank initial pressure [Pa]
rotox0 = ((1-xox0)*(1/rolox0) + xox0*(1/rogox0))^(1); %Density [kg/m3]
utox0 = ulox0 + xox0*(ugox0-ulox0); %Init. Spec. internal energy [J/kg]
htox0 = hlox0 + xox0*(hgox0-hlox0); %Init. Spec. enthalpy [J/kg]
stox0 = slox0 + xox0*(sgox0-slox0); %Init. Spec. entropy [J/kg.K]

% Injection (inj.) system geometry
Cd = 0.6;                %Discharge coefficient (0.6)
Dinj = 2.8E-3;           %Injector diameter [m] (2.96 mm)
Ninj = 1;                %Number of injectors
Ainj = Ninj*pi*(Dinj/2)^2; %Injector area [m2]

% Combustion chamber (c.c.) geometry
Dcc = 95.5E-3;           %C.c. inner diameter [m] (95.5 mm)
Dfp0 = 10E-3;           %F.g. port initial inner diameter [m] (10 mm)
Lf = 30E-3;             %Fuel grain lenght [m] (29.9 mm)
Lpc = 25E-3;            %Pre/Post chamber lenght [m]

Atopcc = pi*((Dcc/2)^2-(Dinj/2)^2); %C.c. top surface [m2]
Atoppc = pi*(Dcc/2)^2; %Pre/Post chamber section area [m2]
Apc = pi*Dcc*Lpc; %Pre/Post chamber inner surface [m2]
Atopf0 = pi*((Dcc/2)^2-(Dfp0/2)^2); %Fuel grain init. top surface [m2]
Afp0 = pi*Dfp0*Lf; %Fuel grain port init. inner surface [m2]
Atopfp0 = pi*(Dfp0/2)^2; %Fuel grain port init. top surface [m2]
Acc0 = Atopcc + 2*Apc + 2*Atopf0 + Afp0; %C.c. init. inner surface [m2]

Vpc = pi*(Dcc/2)^2*Lpc; %Pre/Post chamber volume [m3]
Vfp0 = pi*(Dfp0/2)^2*Lf; %Fuel grain port init. inner volume [m3]
Vcc0 = 2*Vpc + Vfp0; %Combustion chamber init. volume [m3]
Vf0 = pi*((Dcc/2)^2-(Dfp0/2)^2)*Lf; %Fuel grain init. volume [m3]

% Convergent-divergent conical nozzle (n.) geometry
Dnt = 14.2E-3;          %Nozzle throat diameter [m] (14.23 mm)
Eps = 2.39;             %Nozzle expansion ratio (2.39)
Dne = Dnt*(Eps)^(1/2); %Nozzle exit diameter [m]
% Lnconv = (3/(2*((3)^(1/2))))*(Dcc-Dnt); %Nozzle conv. region length [m]
Lnconv = 70E-3; %[m] (70.3 mm ~ 70 mm)
Lncent = 0; %Nozzle central region length [m]
% Lndiv = (((Eps)^(1/2)-1)*(Dnt/2)+0.7*Dnt*(secd(15)-1))...
% /tand(15); %Nozzle divergent region length [m]
Lndiv = 16E-3; %[m] (15.9 mm ~16 mm)
Ln = Lnconv + Lncent + Lndiv; %Nozzle total lenght [m]
tnt = 32E-3; %Nozzle throat wall thickness [m] (32 mm)
xn = 0:2E-3:Ln; %Nozzle x position [m]

Ant = pi*((Dnt/2)^2); %Nozzle throat area [m2]
Ane = pi*((Dne/2)^2); %Nozzle exit area [m2]
Anconvin = (pi/sind(30))...
*((Dcc/2)^2-(Dnt/2)^2); %Nozzle conv. region inner surface [m2]
Ancentin = pi*Dnt*Lncent; %Nozzle cent. region inner surface [m2]
Andivin = (pi/sind(15))...
*((Dne/2)^2-(Dnt/2)^2); %Nozzle div. region inner surface [m2]
Anin = Anconvin + Ancentin + Andivin; %Nozzle total inner surface [m2]

Vnconv = (pi/(3*tand(30))...
*((Dcc/2)^3-(Dnt/2)^3));%Nozzle conv. region volume [m3]
Vncent = pi*(Dnt/2)^2*Lncent; %Nozzle cent. region volume [m3]
Vndiv = (pi/(3*tand(15))...
*((Dne/2)^3-(Dnt/2)^3)); %Nozzel div. region volume [m3]
Vn = Vnconv + Vncent + Vndiv; %Nozzle total volume [m3]

Lneq = Ln; %Equivalent (cylindrical) nozzle lenght [m]
Aneqin = Anin; %Equivalent (cyl.) nozzle inner surface [m2]
Dneq = Aneqin/(pi*Lneq); %Equivalent (cyl.) nozzle inner diameter [m]
tneq = tnt; %Equivalent (cyl.) nozzle wall thickness [m]
Dneqex = Dneq+2*tneq; %Equivalent (cyl.) nozzle exterior diameter [m]
Aneqex = pi*Dneqex*Lneq; %Equivalent (cyl.) nozzle exterior surface [m2]

% Oxidizer tank geometry
Vot = mtox0/rotox0; %Oxidizer tank total volume [m3]
Vgox0 = mgox0/rogox0; %Oxidizer initial vapour volume [m3]
Vlox0 = mlox0/rolox0; %Oxidizer initial liquid volume [m3]
Vtox0 = Vgox0+Vlox0; %Oxidizer initial total volume [m3] (Valid.)

% Constant parameters
Ra = 8314.5; %Universal gas constant [J/kmol.K]

```

```

g = 9.81; %Gravitic aceleration [m/s2]
Csf = 0.0130; %Surface empirical constant
CS = 2; %Safety factor

% Tank walls (c.c. and nozzle) initial conditions
Tw0 = 700; %Walls initial temperature [K] (298 K)
Twcg0 = Tw0; %Init. c.g. side wall surf. temp. [K] (298 K)
Twox0 = Tw0; %Init. ox. side wall surf. temp. [K] (298 K)

% Tank walls (c.c. and nozzle) property constants (Stainless Steel)
cw = 478; %Specific heat [J/(kg.K)]
row = 7810; %Density [kg/m3]
kw = 16.4; %Thermal conductivity [W/m.K]
Twmmax = 1100; %Maximum allowable temperature [K]

% Nozzle wall mesh
[MAT,lMat,NVT,NPT,X,xw,xe,dx,rowt,cwt,kwt] = WallMesh(tnt);
TWt0 = Tw0*ones(1,NPT); %Wall initial temperature [K]
TWtmax = Twmax*ones(1,NPT); %Wall maximum allowable temperature [K]

% Solid fuel properties
rof = 812; %Solid fuel density (Paraffin) [kg/m3]
mf0 = rof*Vf0; %Solid fuel initial mass [kg]

% N2O-Paraffin constant parameters
a = 0.4201; %Regression rate characteristic constant
b = 0.47; %Regression rate characteristic expoent

% Nozzle to tank oxidizer heat transfer efficiency
etanox = 0.25; % 0< etanox < 1

timecal(2) = rem(now,1); %Record initial conditions calculation time [s]
%%
%-----

%
% SIMULATION PROCEDURE
%-----
% VARIABLES INITIALIZATION
% Temperature
Tcg = Tcg0; %Combustion gases temperature [K]
Tcc = Tcc0; %Combustion chamber temperature [K]
Tf = Tf0; %Fuel grain vapour temperature [K]
Tox = Tox0; %Oxidizer temperature [K]
Tot = Tot0; %Oxidizer tank temperature [K]
Tw = Tw0; %Walls temperature [K]
TWt = TWt0; %Wall temperature [K] (f(xn))
Twcg = Twcg0; %C.g. side wall surface temperature [K]
Twox = Twox0; %Oxidizer side wall surface temperature [K]

% Pressure
pcg = pcg0; %Combustion gases pressure [Pa]
pcc = pcc0; %Combustion chamber pressure [Pa]
pox = pox0; %Oxidizer pressure [Pa]
pot = pot0; %Oxidizer tank pressure [Pa]

% Density
rolox = rolox0; %Oxidizer liquid density [kg/m3]
rogox = rogox0; %Oxidizer vapour density [kg/m3]
rotox = rotox0; %Oxidizer density [kg/m3]

% Specific internal energy
ulox = ulox0; %Oxidizer liquid spec. int. energy [J/kg]
ugox = ugox0; %Oxidizer vapour spec. int. energy [J/kg]
utox = utox0; %Oxidizer specific internal energy [J/kg]

% Specific enthalpy
hlox = hlox0; %Oxidizer liquid spec. enthalpy [J/kg]
hgox = hgox0; %Oxidizer vapour spec. enthalpy [J/kg]
htox = htox0; %Oxidizer specific enthalpy [J/kg]

% Specific entropy
slox = slox0; %Oxidizer liquid spec. entropy [J/kg.K]
sgox = sgox0; %Oxidizer vapour spec. entropy [J/kg.K]
stox = stox0; %Oxidizer specific entropy [J/kg.K]

```

```

% Specific heat capacity
cvlox = cvlox0; %Ox. liq. spec. heat cap. (const. vol.) [J/kg.K]
cvgox = cvgox0; %Ox. vap. spec. heat cap. (const. vol.) [J/kg.K]
cplox = cplox0; %Ox. liq. spec. heat cap. (const. pr.) [J/kg.K]
cpgox = cpgox0; %Ox. vap. spec. heat cap. (const. pr.) [J/kg.K]
gamox = gamox0; %Oxidizer specific heat ratio

% Viscosity
visclox = 0.0000601; %Oxidizer liquid viscosity [N.s/m2]
viscgox = 17e-6; %Oxidizer vapour viscosity [N.s/m2]

% Conductivity
kox = 0.0151; %Oxidizer thermal conductivity [W/m.K]

% Molar mass
Mox = 44.0128; %Oxidizer molar mass [kg/kmol]

% Surface tension
Siglox = Siglox0; %Ox. liq. surface tension [N/m]

% Diameter
Dfp = Dfp0; %Fuel grain port inner diameter [m]

% Area
Atopf = Atopf0; %Fuel grain top surface [m2]
Afp = Afp0; %Fuel grain port inner surface [m2]
Atopfp = Atopfp0; %Fuel grain port top surface [m2]
Acc = Acc0; %Combustion chamber inner surface [m2]

% Volume
Vfp = Vfp0; %Fuel grain port inner volume [m3]
Vcc = Vcc0; %Combustion chamber volume [m3]
Vf = Vf0; %Fuel grain volume [m3]
Vgox = Vgox0; %Oxidizer vapour volume [m3]
Vlox = Vlox0; %Oxidizer liquid volume [m3]
Vtox = Vtox0; %Oxidizer total volume [m3] (Valid.)

% Mass
mtox = mtox0; %Oxidizer total mass (7.308)[kg]
mgox = mgox0; %Oxidizer vapour mass [kg]
mlox = mlox0; %Oxidizer liquid mass [kg]
mf = mf0; %Solid fuel mass [kg]

% Quality
xox = xox0; %Oxidizer quality (mvap/mtot)

% Time and counters
et = 5; %Estimated time [s] (15s)
dt = 0.02; %Time step [s]
time = 0; %Initial time counter
i = 1; %Initial simulation step counter

%-----
% VARIABLES PRE-ALLOCATION MEMORY
%-----
% Temperature
TA = zeros(1,et/dt); %Ambient temperature [K]
TCG = zeros(1,et/dt); %Combustion gas temperature [K]
TCC = zeros(1,et/dt); %Combustion chamber temperature [K]
TF = zeros(1,et/dt); %Fuel grain vapour temperature [K]
TW = zeros(et/dt,NPT); %Walls temperature [K] (f(t,X))
TWCG = zeros(1,et/dt); %C.g. side wall surface temperature [K]
TWOX = zeros(1,et/dt); %Oxidizer side wall surface temperature [K]
TOX = zeros(1,et/dt); %Oxidizer temperature [K]
TOT = zeros(1,et/dt); %Oxidizer tank temperature [K]
TN = zeros(et/dt,length(xn)); %Nozzle temperature profile [K]
Tnf = zeros(1,length(xn)); %Nozzle film temperature [K]
TT_STAR = zeros(1,et/dt); %Nozzle throat critical temperature [K]

% Pressure
PCG0 = zeros(1,et/dt); %Project combustion chamber pressure [Pa]
POX0 = zeros(1,et/dt); %Initial oxidizer pressure [Pa]
Pe = zeros(1,et/dt); %Nozzle exit pressure [Pa]
Pa = zeros(1,et/dt); %Ambient pressure [Pa]
PCG = zeros(1,et/dt); %Combustion gases pressure [Pa]
PCG1 = zeros(1,et/dt); %New combustion gases pressure [Pa]
PCC = zeros(1,et/dt); %Combustion chamber pressure [Pa]

```

```

POX = zeros(1,et/dt); %Oxidizer pressure [Pa]
POT = zeros(1,et/dt); %Oxidizer tank pressure [Pa]
PN = zeros(et/dt,length(xn)); %Nozzle pressure profile [Pa]
PT_STAR = zeros(1,et/dt); %Nozzle throat critical pressure [Pa]

% Density
RoCG1 = zeros(1,et/dt); %Combustion gas density [kg/m3]
RoLOX = zeros(1,et/dt); %Oxidizer liquid density [kg/m3]
RoGOX = zeros(1,et/dt); %Oxidizer vapour density [kg/m3]
RoTOX = zeros(1,et/dt); %Oxidizer density [kg/m3]

% Specific internal energy
ULOX = zeros(1,et/dt); %Oxidizer liquid spec. int. energy [J/kg]
UGOX = zeros(1,et/dt); %Oxidizer vapour spec. int. energy [J/kg]
UTOX = zeros(1,et/dt); %Oxidizer specific internal energy [J/kg]

% Specific enthalpy
HCG1 = zeros(1,et/dt); %Combustion gas enthalpy [J/kg]
HLOX = zeros(1,et/dt); %Oxidizer liquid spec. enthalpy [J/kg]
HGOX = zeros(1,et/dt); %Oxidizer vapour spec. enthalpy [J/kg]
HTOX = zeros(1,et/dt); %Oxidizer specific enthalpy [J/kg]

% Specific entropy
SLOX = zeros(1,et/dt); %Oxidizer liquid spec. entropy [J/kg.K]
SGOX = zeros(1,et/dt); %Oxidizer vapour spec. entropy [J/kg.K]
STOX = zeros(1,et/dt); %Oxidizer specific entropy [J/kg.K]

% Specific heat capacity
CpCG1 = zeros(1,et/dt); %C.g. spec. heat cap. (const. pr.) [J/kg.K]
CvLOX = zeros(1,et/dt); %Ox. liq. spec. heat cap. (const. vol.) [J/kg.K]
CvGOX = zeros(1,et/dt); %Ox. vap. spec. heat cap. (const. vol.) [J/kg.K]
CpLOX = zeros(1,et/dt); %Ox. liq. spec. heat cap. (const. pr.) [J/kg.K]
CpGOX = zeros(1,et/dt); %Ox. vap. spec. heat cap. (const. pr.) [J/kg.K]
GamCG1 = zeros(1,et/dt); %Combustion gas specific heat ratio
GamOX = zeros(1,et/dt); %Oxidizer specific heat ratio

% Viscosity
VisCG1 = zeros(1,et/dt); %Combustion gas viscosity [N.s/m2]=[kg/s.m]

% Conductivity
KCG1 = zeros(1,et/dt); %Combustion gas thermal conductivity [W/m.K]

% Prandtl number
PrCG1 = zeros(1,et/dt); %Combustion gas Prandtl number

% Molar mass
MMCg1 = zeros(1,et/dt); %C.g. molar mass [kg/kmol]

% Surface tension
SigLOX = zeros(1,et/dt); %Ox. liq. surface tension [N/m]

% Oxidizer-fuel ratio
OF = zeros(1,et/dt); %Oxidizer-fuel ratio

% Diameter
DCC = zeros(1,et/dt); %C.c. inner diameter [m] (95.5 mm)
DFP = zeros(1,et/dt); %Fuel grain port inner diameter [m]
Dn = zeros(1,length(xn)); %Nozzle diamter [m] (f(xn))

% Length
delta_xn = zeros(1,length(xn)); %Distance between two nozzle points [m]
LN = zeros(1,et/dt); %Nozzle length [m]
LNconv = zeros(1,et/dt); %Nozzle conv. region length [m]

% Area
AtopF = zeros(1,et/dt); %Fuel grain lateral surface [m2]
AFP = zeros(1,et/dt); %Fuel grain port inner surface [m2]
AtopFP = zeros(1,et/dt); %Fuel grain port inner surface [m2]
ACC = zeros(1,et/dt); %Combustion chamber inner surface [m2]
AtCC = zeros(1,et/dt); %C.c. and nozzle inner surface [m2]
Anlat = zeros(1,length(xn)); %Nozzle lateral area [m2] (f(xn))

% Volume
VFP = zeros(1,et/dt); %Fuel grain port inner volume [m3]
VF = zeros(1,et/dt); %Fuel grain volume [m3]
VCC = zeros(1,et/dt); %Combustion chamber volume [m3]
VtCC = zeros(1,et/dt); %C.c. and nozzle volume [m3]

```

```

VgOX = zeros(1,et/dt); %Oxidizer vapour volume [m3]
VlOX = zeros(1,et/dt); %Oxidizer liquid volume [m3]
VtOX = zeros(1,et/dt); %Oxidizer total volume [m3] (Valid.)
VOT = zeros(1,et/dt); %Oxidizer tank total volume [m3]

% Mass
MF = zeros(1,et/dt); %Fuel grain mass [kg]
MlOX = zeros(1,et/dt); %Oxidizer liquid mass [kg]
MgOX = zeros(1,et/dt); %Oxidizer vapour mass [kg]
MtOX = zeros(1,et/dt); %Oxidizer total mass (7.308)[kg]
MtOX0 = zeros(1,et/dt); %Initial oxidizer total mass [kg]

% Regression rate
dR = zeros(1,et/dt); %Regression rate [m/s]

% Mass flow
dMOX = zeros(1,et/dt); %Oxidizer vapour mass flow [kg/s]
dMF = zeros(1,et/dt); %Fuel mass flow [kg/s]
dM = zeros(1,et/dt); %Total mass flow rate [kg/s]
dMCGe = zeros(1,et/dt); %Exhaust combustion gas mass flow [kg/s]
dMOXvap = zeros(1,et/dt); %Vaporized oxidizer mass flux [kg/s]

% Heat coefficients
hcoefcg = zeros(1,length(xn)); %C.g. conv. heat. coef. [W/m2.K] (f(xn))
HcoefCG = zeros(et/dt,length(xn)); %Nozzle conv. coef. profile [W/m2.K]
HcoefCGNm = zeros(1,et/dt); %Mean c.g. conv. heat coef. [W/m2.K]
HcoefOX = zeros(1,et/dt); %Ox. conv. heat coef. [W/m2.K]

% Heat transfer
dQOUTCG = zeros(1,et/dt); %C.g. exhaust heat power [W]
dqoutw_xn = zeros(1,length(xn)); %C.g. heat t. through n.w. [W] (f(xn))
dQOUTW = zeros(1,et/dt); %C.g. heat transfer through nozzle walls [W]
dQNOX = zeros(1,et/dt); %Nozzle to oxidizer heat transfer [W]
dQCOMB = zeros(1,et/dt); %C.c. amount of heat generated [W]

% Quality
XOX = zeros(1,et/dt); %Oxidizer quality (mvap/mtot)

% Exhaust velocity
Ue = zeros(1,et/dt); %Combustion gases exhaust velocity [m/s]
Ueq = zeros(1,et/dt); %Equivalent velocity [m/s]

% Thrust
F = zeros(1,et/dt); %Thrust force [N]

% Specific impulse
ISP = zeros(1,et/dt); %Specific impulse [s]

% Sonic conditions
SCINJ = zeros(1,et/dt); %Injection sonic condition

% Time and counters
TIME = zeros(1,et/dt); %Time

timecal(3) = rem(now,1); %Record initial simulation time [s]
%%

while Dfp < Dcc

%-----
% PRE-COMBUSTION CALCULATIONS
%-----
% Oxidizer mass flow rate calculation
% Injection orifice sonic conditions verification
% Back flow verification
if (pcg >= pox)
    dmox = 0;
    display('WARNING - back flow possibility into oxidizer tank');
    break
end

% Sonic flow conditions (auxiliary variables K1 and K2)
K1 = pox/pcg;
K2 = ((gamox+1)/2)^(gamox/(gamox-1));

```



```

% Subsonic flow conditions (auxiliary variables K3 and K4)
K3 = (pcg/pox)^(2/gamox);
K4 = (pcg/pox)^((gamox+1)/gamox);

% Sonic conditions verification
if ((K1 < K2) && (K3 > K4)) %Subsonic flow case
    dmox_ss = Cd*Ainj*(2*rogox*pox*(gamox/(gamox-1))*...
        ((pcg/pox)^(2/gamox)-(pcg/pox)^((gamox+1)/gamox)))^(1/2);
    dmox = dmox_ss; %Ox. mass flow rate (subsonic) [kg/s]
    scinj = 0; %Injection sonic condition
else %Sonic flow case
    dmox_s = Cd*Ainj*...
        (gamox*rogox*pox*(2/(gamox+1))^((gamox+1)/(gamox-1)))^(1/2);
    dmox = dmox_s; %Ox. mass flow rate (sonic) [kg/s]
    scinj = 1; %Injection sonic condition
end

% Regression rate calculation
dr = a*((dmox/Atopfp)^b)*1E-3; %Regression rate [m/s]

% Fuel mass flow rate calculation
dmf = rof*dr*Afp; %Fuel mass flow rate [kg/s]

% Total mass flow rate calculation
dm = dmox + dmf; %Total mass flow rate [kg/s]

% Oxidizer to fuel ratio calculation
of = dmox/dmf; %Oxidizer to fuel ratio
if (of < 1)
    display('WARNING - O/F below 1');
    break
elseif (of > 15)
    display('WARNING - O/F above 15');
    break
elseif (isnan(of))
    display('WARNING - O/F calculation error');
    break
end

% New fuel grain port diameter calculation
Dfp1 = Dfp + 2*dr*dt; %New fuel grain port diameter [m]

% New surfaces and volumes calculation
Atopfp1 = pi*(Dfp1/2)^2; %New fuel grain port top surface [m2]
Atopf1 = pi*((Dcc/2)^2-(Dfp1/2)^2); %New fuel grain top surf. [m2]
Afp1 = pi*Dfp1*Lf; %New fuel grain port inner surface [m2]
Acc1 = Atopcc + 2*Apc + 2*Atopf1 + Afp1;%New c.c. inner surface [m2]
Vfp1 = pi*(Dfp1/2)^2*Lf; %New fuel grain port inner volume [m3]
Vcc1 = 2*Vpc + Vfp1; %New combustion chamber volume [m3]

% New fuel grain mass and volume calculation
Vf1 = pi*((Dcc/2)^2-(Dfp1/2)^2)*Lf; %New fuel grain volume [m3]
mf1 = rof*Vf1; %New fuel grain mass [kg]

% Oxidizer properties at fuel port
% Mach number and oxidizer temperature calculation
delta_Maox_cc = 1;
Maox_cc_old = 1;
while delta_Maox_cc > 0.001
    Tox_cc_aux = Tox/(1+(((gamox-1)/2)*Maox_cc_old^2));
    rotox_cc_aux = rotox/((Tox/Tox_cc_aux)^(1/(gamox-1)));
    Maox_cc_new = dmox/...
        (Atopfp*rotox_cc_aux*(gamox*(Ra/Mox)*Tox_cc_aux)^(1/2));
    delta_Maox_cc = abs(Maox_cc_old-Maox_cc_new)/Maox_cc_new;
    Maox_cc_old = Maox_cc_new;
end
Tox_cc = Tox_cc_aux;
rotox_cc = rotox_cc_aux;
Maox_cc = Maox_cc_new;

%-----
% COMBUSTION CALCULATIONS
%-----
[Tcg1, rocgl, hcgl, cpcgl, gamegl, viscgl, kcg1, Pregl, Mcgl] = ...
    CombCal(Tox_cc, pcg, of);

```

```

%-----
% COMBUSTION CHAMBER CALCULATIONS
%-----
% Exhaust combustion gases mass flow calculation
dmcge = dmox+dmf; %Exhaust c.g. mass flow [kg/s]

% Nozzle flow calculations
[pcg1,pt_star,Tt_star,pe,Te,ae,ue,Max,Tn,pn,ron,Rn,An] = ...
    NozzleFlowCal(Ra,pa,Tcg1,rocg1,gamcg1,Mcg1,dmcge,Dcc,Lnconv,Ln,xn);

%-----
% PERFORMANCE CALCULATIONS
%-----
f = (((1+cosd(15))/2)*dmcge*ue)+((pe-pa)*Ane); %Thrust force [N]
ueq = ue + ((pe-pa)/dmcge)*Ane; %Equivalent velocity [m/s]
Isp = ueq/g; %Specific impulse [s]

%-----
% HEAT TRANSFER SYSTEM CALCULATIONS
%-----
% Combustion gases convection heat transfer coefficient calculation
for j =1:length(xn)
    %Nozzle film temperature
    Tnf(j) = (Tn(j)+Twcg)/2; %[K]
    %Combustion gas convection coefficient ->
    %-> Cornelisse et al correlation
    hcoefcg(j) = 0.023*(Prpg1^0.33)*kcg1*...
        ((dmcge/(An(j)*viscg1))^0.8)*...
        (1/((Rn(j)*2)^0.2))*(Tcg1/Tnf(j))^(0.68); %[W/m2.K]
end

% Amount of heat generated in combustion chamber calculation
% -> Amount of heat that enters the combustion chamber
% With the oxidizer
dqinox = dmox*hgox; %[W]

% -> Total combustion chamber area and volume
Atcc = Acc + Anin; %C.c and nozzle inner surface [m2]
Vtcc = Vcc + Vn; %C.c and nozzle volume [m3]

% -> Amount of heat that exits the combustion chamber
% Through the combustion gases
dqoutcg = dmcge*hcg1; %[W]
% Through the nozzle walls
for j = 1:length(xn)
    if xn(j) == xn(1)
        delta_xn(j) = (xn(j+1) - xn(j))/2; %[m]
    elseif xn(j) == xn(length(xn))
        delta_xn(j) = (xn(j) - xn(j-1))/2; %[m]
    else
        delta_xn(j) = xn(j+1) - xn(j); %[m]
    end
    Dn(j) = Rn(j)*2;
    Anlat(j) = pi*Dn(j)*delta_xn(j); %[m2]
    dqoutw_xn(j) = Anlat(j)*hcoefcg(j)*(Tn(j)-Twcg); %[W/m]
end
dqoutw = sum(dqoutw_xn); %[W]

% -> Amount of heat stored inside the combustion chamber
dqstcc = cpcg1*rocg1*Vtcc*((Tcg1-Tcg)/dt); %Stored in c.g. [W]

% -> Amount of heat generated in combustion chamber due to combustion
dqcomb = dqstcc + dqoutcg + dqoutw - dqinox;%Combustion [W]

% Amount of heat transfer from nozzle to oxidizer tank
dqnox = etanox*dqoutw;

%-----
% OXIDIZER TANK CALCULATIONS
%-----
mtox1 = mtox - dmox*dt; %New oxidizer mass [kg]
rotox1 = mtox1/Vot; %New oxidizer density [kg/m3]
htox1 = (dqnox*dt+(mtox1-mtox)*hgox+mtox*((1-xox)*hlox+xox*hgox))/...
    mtox1; %New oxidizer spec. enthalpy [J/kg]

```

```

% New oxidizer temperature and quality iterative calculation
[Tox1,xox1] = hro2Tx(htox1,rotox1); %Tox1 [K], xox1 [Adimensional]
if xox1 > 0.95
    display('WARNING - ox. gas fraction exceeds 95% of total ox. mass');
    break
end

% New oxidizer properties calculation
[pox1,rolox1,ulox1,hlox1,slox1,cvlox1,cplox1,Siglox1,rogox1,...
    ugox1,hgox1,sgox1,cvgox1,cpgox1,gamox1] = N2O(Tox1);
pot1 = pox1; %New oxidizer tank pressure [Pa]
rotox1 = ((1-xox1)*(1/rolox) + xox*(1/rogox))^-1; %New dens. [kg/m3]
utox1 = ulox1 + xox1*(ugox1-ulox1); %New spec. internal energy [J/kg]
htox1 = hlox1 + xox1*(hgox1-hlox1); %New spec. enthalpy [J/kg]
stox1 = slox1 + xox1*(sgox1-slox1); %New spec. entropy [J/kg.K]

% New oxidizer quantities calculation
mlox1 = (1-xox1)*mtox1; %New ox. liq. mass [kg]
dmoxvap = (mlox-mlox1)/dt; %Vaporized ox. mass flux [kg/s]
mgox1 = xox1*mtox1; %New ox. vap. mass [kg]
Vlox1 = mlox1/rolox1; %New ox liq. volume [m3]
Vgox1 = mgox1/rogox1; %New ox. vap. volume [m3]
Vtox1 = Vlox1+Vgox1; %New ox. total volume [m3]
if (pox1 > 72e5) || (Tox1 > 309)
    display('WARNING - supercritical oxidizer tank conditions');
    break
end

if (pcg1 < pa)
    display('WARNING - hybrid motor engine extinguished (pcg <= pa)');
    break
end

%-----
% VARIABLE LOGGING
%-----
% Temperature
TA(i) = Ta; %Ambient tempertature [K]
TCG(i) = Tcg; %Combustion gas temperature [K]
TCC(i) = Tcc; %Combustion chamber tempertature [K]
TF(i) = Tf; %Fuel grain vapour temperature [K]
TW(i,:) = Twt; %Walls temperature [K]
TWCG(i) = Twcg; %C.g. side wall surface temperature [K]
TWOX(i) = Twox; %Oxidizer side wall surface temperature [K]
TOX(i) = Tox; %Oxidizer temperature [K]
TOT(i) = Tot; %Oxidizer tank temperature [K]
TN(i,:) = Tn; %Nozzle temperature profile [K]
TT_STAR(i) = Tt_star; %Nozzle throat critical temperature [K]

% Pressure
PCG0(i) = pcg0; %Project combustion chamber pressure [Pa]
POX0(i) = pox0; %Initial oxidizer pressure [Pa]
Pe(i) = pe; %Nozzle exit pressure [Pa]
Pa(i) = pa; %Ambient pressure [Pa]
PCG(i) = pcg; %Combustion gases pressure [Pa]
PCG1(i) = pcg1; %New combustion gases pressure [Pa]
PCC(i) = pcc; %Combustion chamber pressure [Pa]
POX(i) = pox; %Oxidizer pressure [Pa]
POT(i) = pot; %Oxidizer tank pressure [Pa]
PN(i,:) = pn; %Nozzle pressure profile [Pa]
PT_STAR(i) = pt_star; %Nozzle throat critical pressure [Pa]

% Density
RoCG1(i) = rocgl; %Combustion gas density [kg/m3]
RoLOX(i) = rolox; %Oxidizer liquid density [kg/m3]
RoGOX(i) = rogox; %Oxidizer vapour density [kg/m3]
RoTOX(i) = rotox; %Oxidizer density [kg/m3]

% Specific internal energy
ULOX(i) = ulox; %Oxidizer liquid spec. int. energy [J/kg]
UGOX(i) = ugox; %Oxidizer vapour spec. int. energy [J/kg]
UTOX(i) = utox; %Oxidizer specific internal energy [J/kg]

% Specific enthalpy
HCG1(i) = hcgl; %Combustion gas enthalpy [J/kg]

```

```

HLOX(i) = hlox;           %Oxidizer liquid spec. enthalpy [J/kg]
HgOX(i) = hgox;          %Oxidizer vapour spec. enthalpy [J/kg]
HtOX(i) = httox;         %Oxidizer specific enthalpy [J/kg]

% Specific entropy
SLOX(i) = slox;          %Oxidizer liquid spec. entropy [J/kg.K]
SgOX(i) = sgox;         %Oxidizer vapour spec. entropy [J/kg.K]
StOX(i) = stox;         %Oxidizer specific entropy [J/kg.K]

% Specific heat capacity
CpCGl(i) = cpcgl;       %C.g. spec. heat cap. (const. p) [J/kg.K]
CvLOX(i) = cvlox;       %Ox. liq. spec. heat cap. (const. V) [J/kg.K]
CvgOX(i) = cvgox;       %Ox. vap. spec. heat cap. (const. V) [J/kg.K]
CpLOX(i) = cplox;       %Ox. liq. spec. heat cap. (const. p) [J/kg.K]
CpgOX(i) = cpgox;       %Ox. vap. spec. heat cap. (const. p) [J/kg.K]
GamCGl(i) = gamcgl;     %C.g. specific heat ratio
GamOX(i) = gamox;       %Oxidizer specific heat ratio

% Viscosity
VisCGl(i) = viscgl;     %Combustion gas viscosity [N.s/m2]

% Conductivity
KCGl(i) = kcg1;         %Combustion gas thermal conductivity [W/m.K]

% Prandtl number
PrCGl(i) = Prcgl;      %Combustion gas Prandtl number

% Molar mass
MMCGl(i) = Mcgl;       %C.g. molar mass [kg/kmol]

% Surface tension
SigLOX(i) = Siglox;    %Ox. liq. surface tension [N/m]

% Oxidizer-fuel ratio
OF(i) = of;            %Oxidizer-fuel ratio

% Diameter
DCC(i) = Dcc;          %C.c. inner diameter [m] (95.5 mm)
DFP(i) = Dfp;          %Fuel grain port inner diameter [m]

% Length
LN(i) = Ln;           %Nozzle length [m]
LNconv(i) = Lnconv;   %Nozzle conv. region length [m]

% Area
AtopF(i) = Atopf;     %Fuel grain lateral surface [m2]
AFP(i) = Afp;         %Fuel grain port inner surface [m2]
AtopFP(i) = Atopfp;   %Fuel grain port top surface [m2]
ACC(i) = Acc;         %Combustion chamber inner surface [m2]
AtCC(i) = Atcc;       %C.c. and nozzle inner surface [m2]

% Volume
VFP(i) = Vfp;         %Fuel grain port inner volume [m3]
VF(i) = Vf;          %Fuel grain volume [m3]
VCC(i) = Vcc;         %Combustion chamber volume [m3]
VtCC(i) = Vtcc;       %C.c. and nozzle volume [m3]
VgOX(i) = Vgox;       %Oxidizer vapour volume [m3]
VLOX(i) = Vlox;       %Oxidizer liquid volume [m3]
VtOX(i) = Vtox;       %Oxidizer total volume [m3] (Valid.)
VOT(i) = Vot;         %Oxidizer tank total volume [m3]

% Mass
MF(i) = mf;           %Fuel grain mass [kg]
MLOX(i) = mlox;       %Oxidizer liquid mass [kg]
MgOX(i) = mgox;       %Oxidizer vapour mass [kg]
MtOX(i) = mtox;       %Oxidizer total mass (7.308)[kg]
MtOX0(i) = mtox0;     %Initial oxidizer total mass [kg]

% Regression rate
dR(i) = dr;           %Regression rate [m/s]

% Mass flow
dMOX(i) = dmox;       %Oxidizer vapour mass flow [kg/s]
dMF(i) = dmf;         %Fuel mass flow [kg/s]
dMCGe(i) = dmcge;     %Exhaust combustion gas mass flow [kg/s]
dMOXvap(i) = dmoxvap; %Vaporized oxidizer mass flux [kg/s]

```

```

% Heat coefficients
HcoefCG(i,:) = hcoefcg;      %Nozzle conv. heat coef. profile [W/m2.K]

% Heat transfer
dQOUTCG(i) = dqoutcg;      %C.g. exhaust heat power [W]
dQOUTW(i) = dqoutw;      %C.g. heat transfer through nozzle walls [W]
dQNOX(i) = dqnox;      %Nozzle walls heat transfer to oxidizer [W]
dQCOMB(i) = dqcomb;      %C.c. amount of heat generated [W]

% Quality
XOX(i) = xox;      %Oxidizer quality (mvap/mtot)

% Exhaust velocity
Ue(i) = ue;      %Combustion gas exhaust velocity [m/s]
Ueq(i) = ueq;      %Equivalent velocity [m/s]

% Thrust
F(i) = f;      %Thrust force [N]

% Specific impulse
ISP(i) = Isp;      %Specific impulse [s]

% Sonic conditions
SCINJ(i) = scinj;      %Injection sonic condition

% Time and counters
TIME(i) = time;      %Time [s]

%-----
% VARIABLES UPDATE
%-----
% @ Oxidizer tank
Tox = Tox1;
pox = pox1;
rolox = rolox1;
ulox = ulox1;
hlox = hlox1;
slox = slox1;
cvlox = cvlox1;
cplox = cplox1;
Siglox = Siglox1;
rogox = rogox1;
ugox = ugox1;
hgox = hgox1;
sgox = sgox1;
cvgox = cvgox1;
cpgox = cpgox1;
gamox = gamox1;
pot = pot1;
rotox = rotox1;
utox = utox1;
htox = htox1;
stox = stox1;
Vgox = Vgox1;
Vlox = Vlox1;
Vtox = Vtox1;
mgox = mgox1;
mlox = mlox1;
mtox = mtox1;
xox = xox1;

% @ Combustion chamber
Dfp = Dfpl;
Atopfp = Atopfpl;
Atopf = Atopf1;
Afp = Afpl;
Acc = Accl;
Vf = Vf1;
Vfp = Vfpl;
Vcc = Vccl;
mf = mf1;
pcg = pcgl;
Tcg = Tcgl;

time = time + dt;

```

```

%-----
% SIMULATION CYCLE COUNTER
%-----
i = i+1;

%-----
% SIMULATION STOPPAGE CRITERIA
%-----
if Dfp >= Dcc
    display('FUEL EXHAUSTED - burn completed successfully');
end

end

% Mean Specific Impulse
Ispm = sum(ISP)/(length(ISP));

timecal(4) = rem(now,1);    %Record final simulation time [s]
%%
%-----

%-----
% PLOTS
%-----
fig1 = figure(1);
plot(TIME(1:i-1),TCG(1:i-1),'-','color',[0.6 0.6 0.6],'LineWidth',2);
hold on;
plot(TIME(1:i-1),TOX(1:i-1),'-k','LineWidth',2);
grid on;
title('Temperature Evolution')
xlabel('Time [s]');
ylabel('Temperature [K]');
legend('T_c','T_o_x','Location','Best');
% ylim([1000 1200]);
saveas(fig1,'Fig1.png');

fig2 = figure(2);
plot(TIME(1:i-1),PCG0(1:i-1),'--','color',[0.6 0.6 0.6],'LineWidth',2);
hold on;
plot(TIME(1:i-1),PCG(1:i-1),'-','color',[0.6 0.6 0.6],'LineWidth',2);
hold on;
plot(TIME(1:i-1),POX0(1:i-1),'--k','LineWidth',2);
hold on;
plot(TIME(1:i-1),POX(1:i-1),'-k','LineWidth',2);
grid on;
title('Pressure Evolution')
xlabel('Time [s]');
ylabel('Pressure [Pa]');
% ylim([0 2E6]);
legend('p_c_p_r_o_j','p_c','p_o_x_0','p_o_x','Location','Best');
saveas(fig2,'Fig2.png');

fig3 = figure(3);
plot(TIME(1:i-1),dMOX(1:i-1),'--k','LineWidth',2);
hold on;
plot(TIME(1:i-1),dMOXvap(1:i-1),'--','color',[0.6 0.6 0.6],'LineWidth',2);
hold on;
plot(TIME(1:i-1),dMF(1:i-1),'-','color',[0.6 0.6 0.6],'LineWidth',2);
hold on;
plot(TIME(1:i-1),dMCGe(1:i-1),'-k','LineWidth',2);
grid on;
title('Mass Flow')
xlabel('Time [s]');
ylabel('Mass flow [kg/s]');
legend('dm_o_x','dm_v_a_p','dm_f','dm_e','Location','Best');
% ylim([0 0.5]);
saveas(fig3,'Fig3.png');

fig4 = figure(4);
plot(TIME(1:i-1),MtOX0(1:i-1),'-','color',[0.6 0.6 0.6],'LineWidth',2);
hold on;
plot(TIME(1:i-1),MtOX(1:i-1),'-k','LineWidth',2);
hold on;
plot(TIME(1:i-1),MlOX(1:i-1),'--k','LineWidth',2);
hold on;

```

```

plot(TIME(1:i-1),MgOX(1:i-1),'-k','LineWidth',2);
grid on;
title('Oxidizer Mass')
xlabel('Time [s]');
ylabel('Mass [kg]');
legend('Initial','Total','Liquid','Vapour','Location','Best');
% ylim([0 1]);
saveas(fig4,'Fig4.png');

fig5 = figure(5);
plot(TIME(1:i-1),OF(1:i-1),'-k','LineWidth',2);
grid on;
title('Oxidizer to Fuel Ratio')
xlabel('Time [s]');
ylabel('O/F');
ylim([1 15]);
saveas(fig5,'Fig5.png');

fig6 = figure(6);
plot(TIME(1:i-1),dQOUTCG(1:i-1),'--','color',[0.6 0.6 0.6],'LineWidth',2);
hold on;
plot(TIME(1:i-1),dQOUTW(1:i-1),'--k','LineWidth',2);
hold on;
plot(TIME(1:i-1),dQNOX(1:i-1),'-k','LineWidth',2);
grid on;
title('Heat Transfer Rate Evolution')
xlabel('Time [s]');
ylabel('Heat Power [W]');
legend('q_e','q_w_n_o_z_z_l_e','q_o_x_n_o_z_z_l_e','Location','Best');
saveas(fig6,'Fig6.png');

fig7 = figure(7);
plot(TIME(1:i-1),Ue(1:i-1),'--','color',[0.6 0.6 0.6],'LineWidth',2);
hold on;
plot(TIME(1:i-1),Ueq(1:i-1),'-k','LineWidth',2);
grid on;
title('Exhaust Velocity')
xlabel('Time [s]');
ylabel('Exhaust Velocity [m/s]');
ylim([0 2200]);
legend('U_e','U_e_q','Location','Best');
saveas(fig7,'Fig7.png');

fig8 = figure(8);
plot(TIME(1:i-1),F(1:i-1),'-k','LineWidth',2);
grid on;
title('Thrust')
xlabel('Time [s]');
ylabel('Thrust [N]');
ylim([0 500]);
saveas(fig8,'Fig8.png');

fig9 = figure(9);
plot(xn,Rn,'-k','LineWidth',4);
grid on;
title('Nozzle Profile')
xlabel('Distance from nozzle entrance [m]');
ylabel('Nozzle radius [m]');
xlim([0 Ln]);
ylim([0 Rn(:,1)]);
saveas(fig9,'Fig9.png');

integertest = ~mod((length(TIME)/4),1);
integerTest1 = ~mod(((length(TIME)-1)/4),1);
integerTest2 = ~mod(((length(TIME)-2)/4),1);
if integertest == 1
    k(1) = 1;
    k(2) = 1*((length(TIME))/4);
    k(3) = 2*((length(TIME))/4);
    k(4) = 3*((length(TIME))/4);
    k(5) = length(TIME);
elseif integerTest1 == 1
    k(1) = 1;
    k(2) = 1*((length(TIME)-1)/4);
    k(3) = 2*((length(TIME)-1)/4);
    k(4) = 3*((length(TIME)-1)/4);
    k(5) = length(TIME);

```

```

elseif integerTest2 == 1
    k(1) = 1;
    k(2) = 1*((length(TIME)-2)/4);
    k(3) = 2*((length(TIME)-2)/4);
    k(4) = 3*((length(TIME)-2)/4);
    k(5) = length(TIME);
else
    k(1) = 1;
    k(2) = 1*((length(TIME)-3)/4);
    k(3) = 2*((length(TIME)-3)/4);
    k(4) = 3*((length(TIME)-3)/4);
    k(5) = length(TIME);
end
legend_str{k(1)} = strcat('@ t= ', num2str(TIME(k(1))), 's');
legend_str{k(2)} = strcat('@ t= ', num2str(TIME(k(2))), 's');
legend_str{k(3)} = strcat('@ t= ', num2str(TIME(k(3))), 's');
legend_str{k(4)} = strcat('@ t= ', num2str(TIME(k(4))), 's');
legend_str{k(5)} = strcat('@ t= ', num2str(TIME(k(5))), 's');

fig10 = figure(10);
plot(xn,PN(k(1),:),'-','color',[1 0 0],'LineWidth',2);
hold on;
plot(LNconv(k(1)),PT_STAR(k(1)),'o','color',[0 0 1],'LineWidth',2);
hold on;
plot(LN(k(1)),Pa(k(1)),'s','color',[0 1 0],'LineWidth',2);
hold on;
legend('p_x','p*','p_a','Location','Best');
for z = 2:5
    plot(xn,PN(k(z),:),'-','color',[1 0 0],'LineWidth',2);
    hold on;
    plot(LNconv(k(z)),PT_STAR(k(z)),'o','color',[0 0 1],'LineWidth',2);
    hold on;
    plot(LN(k(z)),Pa(k(z)),'s','color',[0 1 0],'LineWidth',2);
    hold on;
end
grid on;
title('Nozzle Pressure Profile')
xlabel('Distance from nozzle entrance [m]');
ylabel('p_x [Pa]');
xlim ([0 Ln]);
ylim ([0 2.2E6]);
% Text legend above the curves
x_string=xn(1);
y_string=PN(:,1);
text(x_string,y_string(1)+8E4,legend_str{k(1)});
for z = 2:5
    dy = (y_string(k(z))-y_string(k(z)-1));
    if dy < 0.1E6
        text(x_string,y_string(k(5))-8E4,legend_str{k(5)});
        break
    else
        text(x_string,y_string(k(z))+8E4,legend_str{k(z)});
    end
end
end
saveas(fig10,'Fig10.png');

fig11 = figure(11);
plot(xn,TN(k(1),:),'-','color',[1 0 0],'LineWidth',2);
hold on;
plot(LNconv(k(1)),TT_STAR(k(1)),'o','color',[0 0 1],'LineWidth',2);
hold on;
plot(LN(k(1)),TA(k(1)),'s','color',[0 1 0],'LineWidth',2);
hold on;
legend('T_x','T*','T_a','Location','Best');
for z = 2:5
    plot(xn,TN(k(z),:),'-','color',[1 0 0],'LineWidth',2);
    hold on;
    plot(LNconv(k(z)),TT_STAR(k(z)),'o','color',[0 0 1],'LineWidth',2);
    hold on;
    plot(LN(k(z)),TA(k(z)),'s','color',[0 1 0],'LineWidth',2);
    hold on;
end
grid on;
legend('T_x','T*','T_a','Location','Best');
title('Nozzle Temperature Profile')
xlabel('Distance from nozzle entrance [m]');
ylabel('T_x [K]');

```



```

xlim ([0 Ln]);
% ylim ([0 1.05]);
% Text legend above the curves
x_string=xn(1);
y_string=TN(:,1);
text(x_string,y_string(1)+100,legend_str{k(1)});
for z = 2:5
    dy = (y_string(k(z))-y_string(k(z)-1));
    if dy < 25
        text(x_string,y_string(k(5))-100,legend_str{k(5)});
        break
    else
        text(x_string,y_string(k(z))-100,legend_str{k(z)});
    end
end
saveas(fig11,'Fig11.png');

fig12 = figure(12);
plot(xn,HcoefCG(k,:), '-','color',[1 0 0],'LineWidth',2);
grid on;
title('Nozzle Convective Heat Coefficient Profile')
xlabel('Distance from nozzle entrance [m]');
ylabel('h_c_o_n_v,_x [W/m2.K]');
xlim ([0 Ln]);
% ylim ([0 1.05]);
x_string=Lnconv;
y_string=HcoefCG(:,36);
text(x_string,y_string(1)+700,legend_str{k(1)});
for z = 2:5
    dy = (y_string(k(z))-y_string(k(z)-1));
    if dy < 700
        text(x_string,y_string(k(5))-700,legend_str{k(5)});
        break
    else
        text(x_string,y_string(k(z))-350,legend_str{k(z)});
    end
end
end
saveas(fig12,'Fig12.png');

timecal(5) = rem(now,1);    %Record plotting time [s]
%%
%-----
%
% PROGRAM REPORT
%-----
display(['Total calculation time ='...
num2str((timecal(5)-timecal(1))*3600*24) ' s'])
display(['Iteration time ='...
num2str((timecal(4)-timecal(3))*3600*24/i) ' s'])

```